UNIVERSITY OF BUCHAREST
FACULTY OF PHYSICS

PRODUCTION STUDIES OF Λ_b BARYONS AT LHCB

PhD candidate,
Bogdan Paul Popovici

PhD adviser,
Prof. Dr. Sabin Stoica

A thesis submitted for the degree of
Doctor of Philosophy
2011

I would like to dedicate this thesis to my coleague and friend
Bogdan Popescu.

Acknowledgements

I would like to warmly thank to my supervisor dr. Sabin Stoica for his permanent guidance and for giving me the opportunity to work in such a large and "beautiful" collaboration as LHCb. I have met there many interesting and dedicated people which helped me shape my understanding on the current problems in particle physics. I mention here Olivier Schneider, Guy Wilkinson, Tatsuya Nakada who guided my participation in the CERN working groups. Special thanks are due to my collaborators Raluca Muresan and Marco Adinolfi who helped me with the intricacies of LHCb software and the studies from this thesis. Also, I would like to thank to all my colleagues from LHCb-RO group for many interesting discussions about LHCb subjects and to my colleagues from DFT department for their support and understanding.

This thesis was financed by the Romanian National Authority for Scientific Research (ANCS), mainly through the Program "Capacitati" which supports the Romanian participation at CERN.

Abstract

This thesis contains the main results obtained by the author during his participation in the Large Hadron Collider beauty (LHCb) collaboration as member of the Romanian LHCb group. They refer to contributions obtained both during the construction period of the LHCb detector and after the start of the Large Hadron Collider (LHC) and of the LHCb experiment.

The thesis is structured into five chapters and one Annex. In the first Chapter - Introduction, a general view of the Standard Model (SM) and its limitations are presented, together with the general motivation for the LHC, and particularly, for the LHCb searches. In Chapter 2, the theoretical tool used in SM cross section calculations, i.e. the perturbative Quantum Chromodynamic (pQCD), is shortly described, together with the phenomenology of the b quark production and Λ_b physics, with the goal of a better understanding of the context in which the main contribution of this thesis falls into. In the third Chapter, a detailed description of the LHCb detector and its subdetectors is presented, aiming to provide the reader with more detailed information about the detector's performances and the type of events that can be searched for at the LHCb experiment. Chapter 4 presents the contribution of the author to the development of a calibration method for the RICH subdetectors, which turned out to be very useful in order to fully exploit its performances for hadron identification over the wide momentum range, from 2 to 100 GeV/c. Further, the method is applied to the case of the measurement of Λ_b production.

The main contribution of this thesis is described in Chapter 5 and consists in a complete analysis of a measurement of the Λ_b^0 pro-

duction cross section at 7 TeV in hadronic events at LHCb experiment. Using the data collected in 2010, of $35pb^{-1}$, the total cross section was measured after the reconstruction of the decay chain, $\Lambda_b^0 \to J/\psi(\mu^-\mu^+)\Lambda^0(p\pi^-)$, using several methods of selecting different types of tracks for the "stable" particles.

Another original contribution, presented in Annex A.2, refers to writing a complex software package which can be generically used in other similar data analyzes. Other contributions related to the participation of the author in the monitoring of the data acquisition by the LHCb detector and in offline checking of the data quality are also mentioned.

Contents

Contents **v**

List of Figures **vii**

1 Introduction **2**

2 QCD and b physics **8**

2.1 QCD 9

2.2 b hadrons production 17

2.3 Λ_b phenomenology - a literature review 25

3 LHCb experiment @ CERN **33**

3.1 LHC and CERN 33

3.2 The LHCb detector and performances 39

3.3 The LHCb computing 59

4 Particle identification studies with RICH detectors **62**

4.1 Physics of RICH detectors 62

4.2 MC free calibration of LHCb RICH detectors using the $\Lambda \to p\pi$ decay 67

4.3 Performance studies - Λ_b case 72

5 Measurement of the $\Lambda_b \to J/\Psi\Lambda^0$ production cross-section **77**

5.1 Data Samples 78

5.2 Reconstruction and selection 82

5.3 Efficiencies 89

5.4 Event yields 97
5.5 Systematic studies 98
5.6 Cross-section determination 111

6 Summary **114**

A **116**
A.1 Efficiency details 116
A.2 BPython: The offline software package 123

References **128**

List of Figures

1.1 Energy scales . . . 4
1.2 Invariant mass of jet pairs plus a W from CDF . . . 5

2.1 Meson spectrum . . . 11
2.2 Baryon spectrum . . . 12
2.3 Ratio of hadrons production to lepton production in e^+e^- . . . 13
2.4 Deep inelastic scattering . . . 14
2.5 QCD interaction vertices . . . 15
2.6 Running of α_s . . . 16
2.7 parton distributions . . . 20
2.8 hadron collisions . . . 22
2.9 Cloud words for high energy physics software . . . 24
2.10 Λ_b decay . . . 26
2.11 Λ_b in ratio of production fractions . . . 30
2.12 Branching ratio and forward-backward asymmetry for $\Lambda_b \to \Lambda l^+ l$ in ACD extra dimension model. . . . 32

3.1 Instantaneous luminosity at LHC . . . 35
3.2 Accelerator and storage chain of LHC . . . 36
3.3 Number of bunches in LHC beams . . . 38
3.4 $b\bar{b}$ correlation in pp collisions at LHC. . . . 39
3.5 Integrated luminosity at LHCb . . . 40
3.6 LHCb detector . . . 41
3.7 Overview of the Level-0 trigger. . . . 42
3.8 Trigger flow diagram . . . 44

3.9 Types of tracks . . . 45
3.10 Performance plots for tracks reconstruction. . . . 47
3.11 Display of VELO sensors. . . . 48
3.12 Magnetic field . . . 49
3.13 Silicon trackers. . . . 50
3.14 OT module. . . . 51
3.15 RICH1 and RICH2 detectors . . . 53
3.16 RICH coverage . . . 54
3.17 Calorimeter tiling . . . 56
3.18 Muon stations . . . 58
3.19 Efficiencies for the muon detector . . . 59

4.1 Rich separation of topological similar events. . . . 63
4.2 Cherenkov light . . . 65
4.3 Photon rings reconstructed in Cherenkov detectors . . . 67
4.4 RICH PID . . . 68
4.5 Momentum distributions for protons and pions from Λselection . . 69
4.6 $p\pi$-invariant mass . . . 70
4.7 Armenteros-Podolanski plots . . . 71
4.8 Identification and misidentification efficiency curves . . . 72
4.9 Invariant mass distributions of PID calibration samples. . . . 74
4.10 Construction of MC Efficiencies . . . 75
4.11 PID Efficiency residuals. . . . 76

5.1 Invariant mass for J/Ψ . . . 83
5.2 Invariant mass for Λ^0. . . . 85
5.3 p_T spectra for Λ^0 . . . 86
5.4 p_T spectra of $\bar{\Lambda}^0$ . . . 86
5.5 Invariant mass for Λ^0 . . . 88
5.6 The phase space of the analysis. . . . 88
5.7 Distributions of the simulated Λ_b polar angle. . . . 90
5.8 The correction factor for geometrical acceptance . . . 90
5.9 Best track multiplicities . . . 91
5.10 Map of the tracking weights . . . 92

5.11 Reconstruction efficiencies 94
5.12 Trigger efficiency 95
5.13 Fits of $\bar{\Lambda}_b$ invariant mass 97
5.14 Fits of Λ_b invariant mass 98
5.15 Λ_b polarization angles 102
5.16 MC toys distributions for trigger systematic 105
5.17 MC toy distribution for reconstruction systematic 106
5.18 MC toy distribution for tracking systematic 107
5.19 The ratio between the proton PID efficiency 108
5.20 The measured Λ_b cross-section 111
5.21 Comparison with CMS results 113

A.1 Fit of J/ψ invariant mass for ~~TIS~~TOS MagUp samples 120
A.2 Fit of J/ψ invariant mass for ~~TIS~~TOS MagDown samples 120
A.3 Fit of J/ψ invariant massfor TISTOS MagUp samples 121
A.4 Fit of J/ψ invariant mass for TISTOS MagDown samples 121
A.5 Fit of J/ψ invariant mass for TIS~~TOS~~ MagUp samples 122
A.6 Fit of J/ψ invariant mass for TIS~~TOS~~ MagDown samples 122

Chapter 1

Introduction

The Standard Model (SM) is a theory of elementary particles and the way they interact through the electromagnetic, weak, and strong forces. Developed in the 1970s, it incorporated all the elementary particles known at that time, but also it correctly predicted the existence and the properties of new ones which were later discovered. The charm, bottom and top quarks, the tau neutrino, the $W^{\pm}$ and Z bosons were thus predicted before they were discovered. The last predicted but still undiscovered particle, the Higgs boson, is now almost to be confirmed, after the discovery of a new particle with its characteristics reported at LHC in July 2012 [1; 2]. The SM is also one of the most developed and tested theories in physics. The part which describes the electromagnetic interactions of the particles, the quantum electrodynamic field theory (QED), supports calculations of physical quantities with unparalleled precision. As an example, the theoretical and the experimentally measured value of the magnetic dipole moment of the muon, agree within a very high precision: $g_{\mu}(th.)/g_{\mu}(exp.) = 0.99999518$.

The SM combines two well established theories the special relativity and Quantum Mechanics that fundamentally changed our view about the world and the limits we can access. There are four fundamental interactions in the nature: strong, weak, electromagnetic and gravity, while SM provides an elegant and coherent picture based on the notion of symmetry for the first three of them. In the language of gauge theories the basic structures are the fields, the fields of matter of spin $\frac{1}{2}$ and of those which carry the interaction of spin 1, and which are subject to specific symmetries. The fields are described by representations of an abstract

	Particles	Mass [MeV/c^2]	Spin	Charge/e^+	Colour states
quarks	down (d)	4-8	1/2	-1/3	3
	up (u)	1.5-4	1/2	2/3	3
	strange (s)	80-130	1/2	-1/3	3
	charm (d)	$(1.15 - 1.35) \cdot 10^3$	1/2	2/3	3
	bottom (b)	$(4.1 - 4.9) \cdot 10^3$	1/2	-1/3	3
	top (t)	$1.74 \cdot 10^6$	1/2	2/3	3
leptons	e^-	0.511	1/2	-1	0
	ν_e	$< 3 \cdot 10^{-6}$	1/2	0	0
	μ^-	105.66	1/2	-1	0
	ν_μ	< 0.19	1/2	0	0
	τ^-	1777	1/2	-1	0
	ν_τ	< 18.2	1/2	0	0
gauge bosons	γ	0	1	0	0
	$W^\pm$	$80.41 \cdot 10^3$	± 1	0	0
	Z	$91.18 \cdot 10^3$	1	0	0
	gluon (g)	0	1	0	8
	Higgs (H)	$> 114 \cdot 10^3$	0	0	0
	Graviton (G)	0	2	2	0

Table 1.1: Particles of the minimal Standard Model: the first group contains quarks, the second, leptons, and the last one, gauge bosons. All charges are given in units of positron charges. The gravitational force is also considered. The graviton and Higgs boson are the last two un-observed particles.

symmetry group, and the interactions fields are induced by the requirement that the Lagrangian is invariant with respect to arbitrary transformations within the representations. The Lagrangian of the Standard Model is invariant under the symmetry:

$$SU(3) \otimes SU(2) \otimes U(1) \tag{1.1}$$

The matter fields are divided between leptons and quarks considering the interactions they take part in, the leptons interact only weak and/or electromagnetic, while quarks participate in all three. There are three generations of leptons, each of them consisting of a charged particle (electron, muon, tau) and a neutral partner (electron, muon and tau neutrinos). In an analogous manner, three generations of quarks exist, each consisting of a charge $+2/3$ quark (up, charm and top) and a charge $-1/3$ quark (down, strange and bottom). The generations are arranged by a mass hierarchy which is not completely understood, see Table 1.1

for a view of their properties.

As for the interaction fields, the $SU(2) \otimes U(1)$ symmetry of the electroweak part dictates the existence of heavy mass gauge bosons, $W^{\pm}$, Z for the weak interaction and of the photon for the electromagnetic interaction. Quarks carry the property of colour and the $SU(3)$ group implies 8 mediators (gluons) for the strong interaction.

The massive particles within the model acquire their mass through the proposed Higgs mechanism which requires that the above mention fields couple to an additional scalar field, called Higgs boson, whose discovery has not been confirmed yet.

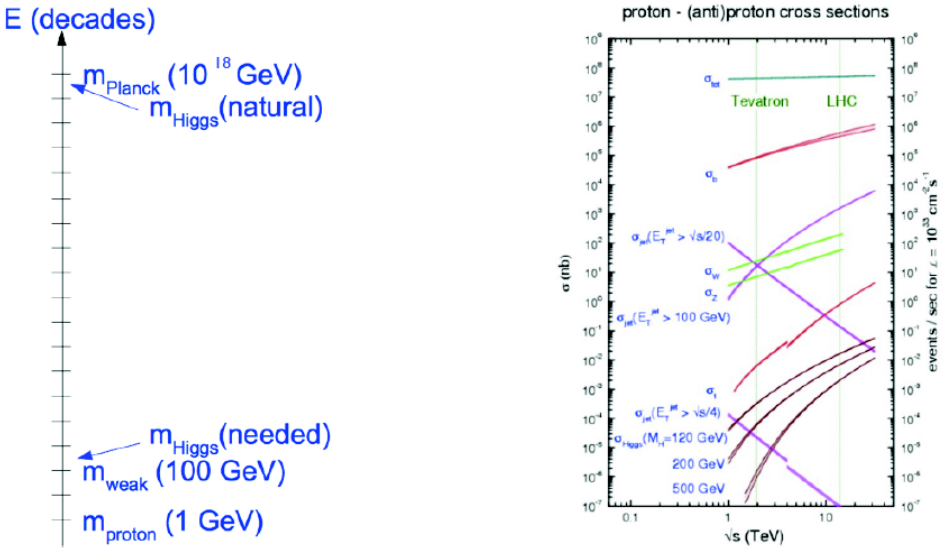

Figure 1.1: Energy scales.

The Standard Model is a very robust theory tested in numerous experiments in the past 40 years, but it does not address a series of open problems, like the explanation for the mass hierarchies, the inclusion of the gravitational interaction into the model, and other experimental observations from astrophysics, such as, dark matter, the disparity between matter and antimatter etc. All these questions lead to the conclusion that a new kind of physics should be introduced in our explanations. As suggested in Fig. 1.1, left side, the natural place to look for these new phenomena would be at the scale of Planck mass 10^{18} GeV. However,

the couplings with the physics from the electroweak scale suggest that the mass for the Higgs boson should be searched at the TeV scale. The Higgs as well as other heavy particles, like the top quark, should appear in the loop diagrams of the known physics, and since these are well constrained, the corrections introduced by new particles should be small. In order to keep the corrections small, the masses of the new particles should be of order of the heaviest known quark, the top mass. This theoretical hint is one of the most important motivation for building the large and expensive experiments at TeV scale like those from LHC at CERN.

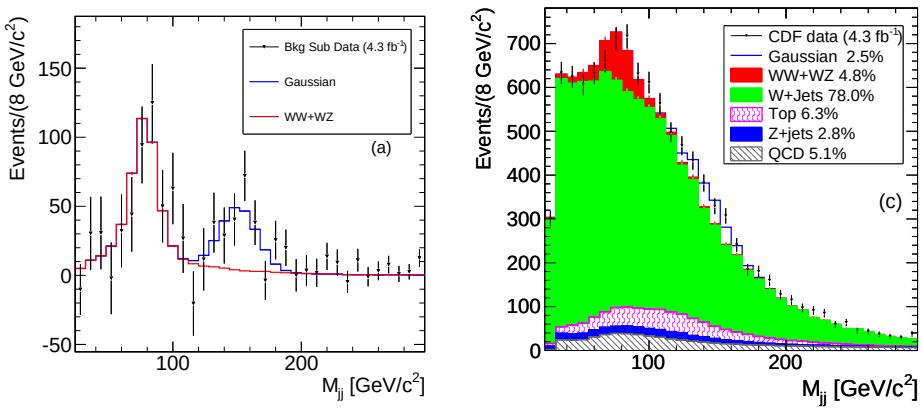

Figure 1.2: Findings from CDF in an analysis of invariant mass distribution of jet pairs produced in association with a W boson [3]. In the left side the dijet invariant mass is shown after the subtraction of the background. A peak not foreseen by the SM is shown in blue. In the right side the same distribution is plotted before subtracting the background. Expected SM contributions are shown with different colours. The uncertainties on the knowledge of these components could explain the observed peak.

Once such experiments constructed, one should realize that the cross section for producing the Higgs boson is very small compared to the SM background from b quark, t quark or W and Z. From Fig. 1.1, right side, we can see that the Higgs production rates can be smaller from 2 to 8 orders than these backgrounds. Thus, both large luminosities and good understanding of the SM predictions are required for the observation of the Higgs. Cases like the one recently reported by CDF Collaboration in $W + 2$ jets measurement, where an unexpected peak

was found after the subtraction of the background [3], can be clarified only after a good control of the QCD contributions is in place. In Fig. 1.1 the predictions from the CDF observation can be compared with the predictions before and after subtracting the background. For the moment, the excess of the observed events cannot be definitively interpreted due to the large uncertainties in the theoretical predictions. It rests on future collaborative efforts from QCD, the experiments and the Monte Carlo (MC) computer simulations to improve our knowledge in situations like this.

The broad subject of this paper lies in the fields of testing the predictions of the perturbative QCD and Λ_b^0 phenomenology. In the second chapter we dwell on the theory of the SM, first on the electroweak part and the appearance of the Higgs field and then, to a larger extent on the QCD theory and the phenomenology of b quark production in hard interactions. The decomposition of the hard interactions in stages as they are seen by the Monte Carlo simulators are then described, leading to the necessity of their further improvement. Also in this chapter the program for the study of Λ_b baryon is sketched as it currently appears in the literature.

This thesis is based on the contribution of the author to the LHCb Collaboration at CERN, thus in the third chapter the LHCb experiment and its role in the CERN program are described. The LHCb detector is a $10m \times 10m \times 15m$ sophisticated piece of engineering formed from thousands of sub-components which are running smoothly together. In this chapter, the detector is described from the viewpoint of the principal sub-detectors, their physics principles and the operation workflow of the experiment. Also the personal contribution to the data acquisition monitoring and analysis of the data quality is mentioned here.

In the fourth chapter more details are presented on the Ring Imaging CHerenkov (RICH) sub-detector, one of the sub-detectors responsible for the identification of the particles in the final state. Here the author was involved in developing a method for the calibration of RICH using the input from real data.

The next chapter presents one of the main contributions of this thesis, which is the measurement of the Λ_b^0 production cross-section at LHCb at $\sqrt{s} = 7$ TeV. The structure of the chapter underlines the main steps of the analysis, choosing of the data, simulation samples and trigger conditions, reconstructing the Λ_b

candidates, calculating the efficiencies, extracting the signal yields and performing the systematic tests and displaying the results. All these steps are presented in detail and the main options are justified. The final results are expressed as the integral cross section for producing Λ_b and $\bar{\Lambda}_b$ baryons multiplied by the branching ratios of $\mathcal{B}(\Lambda_b \to J/\Psi\Lambda^0)$.

$$\sigma(pp \to \Lambda_b X)_{PS}\mathcal{B}(\Lambda_b \to J/\Psi\Lambda^0) = 4.08 \pm 0.59(stat) \pm 0.36(sys)\text{nb}$$

$$\sigma(pp \to \bar{\Lambda}_b X)_{PS}\mathcal{B}(\bar{\Lambda}_b \to J/\Psi\bar{\Lambda}^0) = 2.60 \pm 0.46(stat) \pm 0.26(sys)\text{nb}$$

The thesis ends with the conclusions and suggestions for future developments of the studies presented and with additional details on different topics left for the appendices. A part of the Annex is dedicated to the software package that was written for the studies in this thesis.

Chapter 2

QCD and b physics

The present decade in the high energy physics will undoubtedly be dominated by new results from LHC. Its main focus is placed on studies of the dynamics of the electroweak symmetry breaking and on the searches for possible manifestations of beyond the Standard Model physics. However, the main feature of the events studied at LHC is the very complex QCD final states accessible to the detectors. This is due to the rich structure of the initial colliding protons which are not simple point like particles. In the current picture of the parton model, the hadrons are seen as balls of valence quarks surrounded by virtual partons (quarks and gluons), whose distributions depend on energy. Beside the hard interaction of the colliding protons, the strong interaction appears in the formation of the hadrons (hadronization process) and also interferes with electroweak interaction at the stage of particles decays. Tests of QCD are thus important for many applications at LHC collider.

In this chapter we introduce some theoretical aspects and motivation regarding b quark production and Λ_b studies. In the first section the QCD theory and its main features are introduced. The b quark production framework is presented in the second section from the view point of the perturbative QCD and then of the Monte Carlo (MC) generators. The state of the art for b quark production is the FONLL scheme, a fix order calculation at next-to-leading-order (NLO) with summation of the large logarithms. The Monte Carlo generators are used to simulate pp collisions and address in a specific manner non-perturbative phenomena like parton showers, hadronization, interaction with the underlying events.

In the last section we look at the Λ_b baryon and review some interesting phenomenological aspects. The study of Λ_b is useful both from the point of view of the SM and of NP effects. The analysis of Λ_b production from this thesis can easily be developed in one of those studies.

2.1 QCD

The view on the QCD appears as a dual one [4]. Some see it as "our most perfect physical theory" [5], much better established than the electroweak theory. It has only one parameter, the strong coupling, and it contains a wealth of phenomena: radiative couplings, confinement, spontaneous (chiral) symmetry breaking, anomalies, instantons. And, basically, there is no alternative theory of strong interaction. Meanwhile the electroweak theory is responsible for the quark masses, it has a lot of parameters, and quite a few alternatives are possible for the symmetry breaking sector.

The alternative view is that the electroweak theories are much better established. Here, we can compute every accessible phenomenon with great accuracy, and seek accurate comparisons with experimental results. Meanwhile, the QCD is notoriously difficult to compute due to the highly non-perturbative parts of the theory at small momenta and the proliferation of diagrams needed to be considered in the perturbative regime. The passing from one regime to the other is not very well founded in the theoretical framework and needs experimental input. Thus, predictions for the basic quantities include several steps which include: factorization, hard processes, infrared safety, parton showers and matching, hadronization and the so-called underlying events.

We continue this section by introducing QCD with a few historical motivations and by explaining some of its properties.

2.1.1 Motivation

Quantum Chromodynamic, the gauge field theory that describes the strong interactions of colored quarks and gluons, is the SU(3) component of the $SU(3) \otimes SU(2) \otimes U(1)$ Standard Model of Particle Physics. For the broad topics regarding

QCD a list of resources can be found in the the following paper [6].

The $SU(3)$ group is the group of 3×3 complex unitary matrices U with unit determinant

$$U^\dagger U = 1, \qquad \det U = 1.$$

From observation $SU(3)$ symmetry acting on colour is an exact symmetry and the only free states seen are neutral in colour. Thus invariants can be easily formed out of quark-antiquark states

$$\sum_i \psi_i^* \psi_i \to \sum_i U_{ij}^* \psi_j^* U_{ik} \psi_k = \sum_{kj} (\sum_i U_{ji}^\dagger U_{ik}) \psi_j^* \psi_k = \sum_k \psi_k^* \psi_k \tag{2.1}$$

where the subscript is the index of colour and ψ_i is the quark field. Also we can form colour singlet from three-quark states

$$\sum_{ijk} \epsilon^{ijk} \psi_i \psi_j \psi_k \to \sum_{ijk} \epsilon^{ijk} U_{ii'} U_{jj'} U_{kk'} \psi_{i'} \psi_{j'} \psi_{k'} = \epsilon^{i'j'k'} \psi_{i'} \psi_{j'} \psi_{k'} \tag{2.2}$$

where the following identity was used for the last step

$$\sum_{ijk} \epsilon^{ijk} U_{ii'} U_{jj'} U_{kk'} = \det U \epsilon^{i'j'k'} \tag{2.3}$$

The most important multiplets that can be formed as combinations of two and three quarks are displayed in Figs. 2.1 and 2.2. Multiplets are classified according to their transformation properties under the flavour group. Each multiplet contains particles with similar properties. This flavour picture encountered a problem in 1951, when the Δ^{++} baryon, composed of three quarks u, was discovered. The total wave function of the Δ^{++}, according to the Pauli principle has to be antisymmetric. The introduction of a new degree of freedom, the colour hypothesis, allows to have states symmetric in spin, flavour and spatial wave function and antisymmetric in colour, and thus the total wave function to be antisymmetric.

$$|\Delta^{++}\rangle = |u_\uparrow u_\uparrow u_\uparrow\rangle \quad \to \quad |\Delta^{++}\rangle = \epsilon^{ijk} |u_{i\uparrow} u_{j\uparrow} u_{k\uparrow}\rangle \tag{2.4}$$

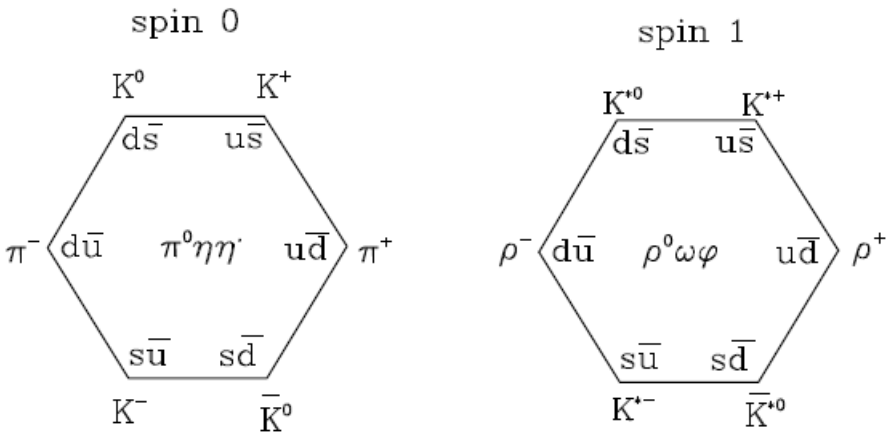

Figure 2.1: Meson spectrum [4].

An important experimental confirmation of the existence of the colour quantum number was given by the study of the total cross section at e^+e^- colliders. As a first approximation, one expects that the ratio between the decaying cross section into hadrons and into leptons to depend only on the charge and the number of possible final states:

$$R = \frac{\sigma(e^+e^- \rightarrow hadrons)}{\sigma(e^+e^- \rightarrow \mu^+\mu^-)} = \frac{\sum_{quarks} q^2_{quarks}}{q^2_\mu} \tag{2.5}$$

where the sum has to be carried out on quarks which can be produced at the energies of the machine.

The experimentally measured ratios at various energies Fig.2.3 are compatible with the hypothesis of the colour existence, and the number of colours 3.

Another confirmation for the quark parton model and later of QCD came in 1968 with the results on the deep inelastic scattering in e^-p experiments from SLAC (Standford Linear Accelerator Center, Stanford, California) [8], which showed evidence for scaling phenomenon. The deep inelastic scattering process, sketched in Fig. 2.4, is the collision of a lepton with a nucleon target, which fragments into high multiplicity, massive final states. The kinematics of the scattering process can be defined by only two independent variables. We have chosen

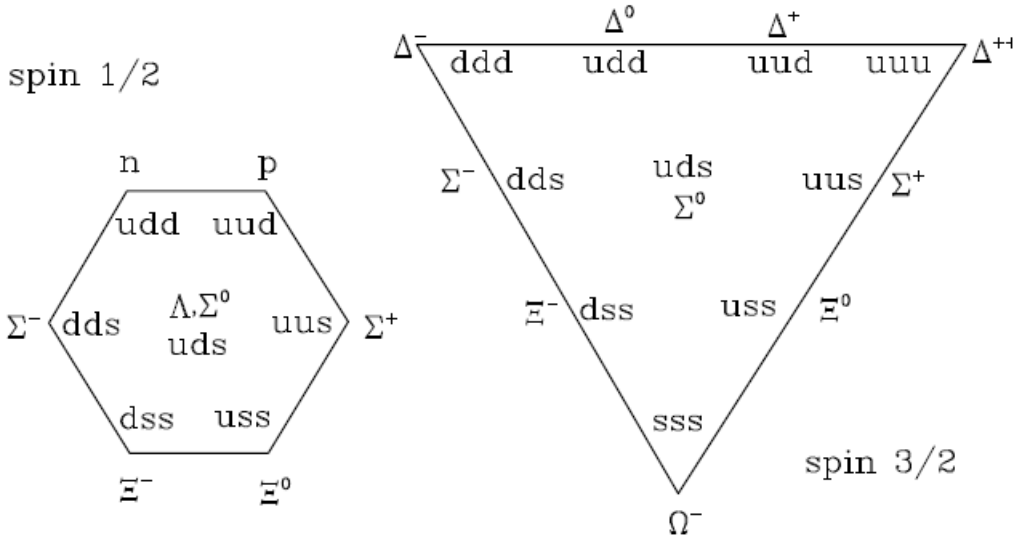

Figure 2.2: Baryon spectrum [4].

the x and y dimensionless variables defined below:

$$x_{Bj} = \frac{Q^2}{2p \cdot q} \quad y = \frac{q \cdot p}{k \cdot p}, \tag{2.6}$$

where $Q^2 = -q^2 = (k - k')^2 = 2k \cdot k'$.

The term "deep inelastic scattering" means that both Q^2 and pq are large with respect to m_p, but the x_{Bj} remains finite. The limit where $Q \to \infty$, $pq \to \infty$, is called Bjorken limit. Scaling means [4] that the differential cross section, when expressed in terms of these dimensionless parameters, in the limit of high energy with x and y fixed, scales like the energy in the process, according to its canonical dimension

$$\frac{d\sigma}{dxdy} \propto \frac{1}{Q^2}. \tag{2.7}$$

This property is quite remarkable, since it looks more like the behavior one may find in a renormalizable field theory with a dimensionless coupling, like electrodynamics. This phenomena was also observed in e^+e^- annihilation and has given a strong evidence that if a field theory was to describe strong interactions, it had to be weakly coupled at high energies, that is to say, it had to be asymptotically free. In its turn this linked to the non-abelian gauge theories which could

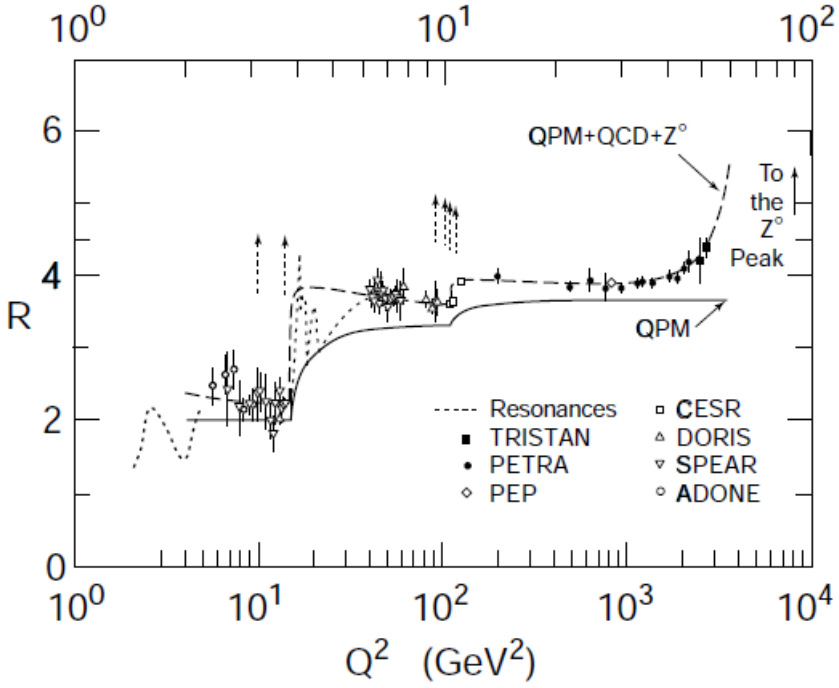

Figure 2.3: Ratio of hadrons production to lepton production in e^+e^- as function of c.m. energy [7]. The expectation of quark parton model when also the QCD and the Z^0 are included is $N_c = 3$.

explain the asymptotical freedom, and also indicated that the condition of colour neutrality of the hadron spectrum must have a dynamical origin.

In modern view QCD is scale invariant only to the first approximation. This can be seen in the contexts as, when one zooms in on a QCD jet, when repeated self-similar pattern of jets within jets within jets, reminiscent of fractals such as the famous Mandelbrot set in mathematics, appears. In the context of QCD, the original Bjorken scaling, called also light-cone scaling, is also related to the conformal invariance theoretical approaches which are now being studied, or to the physics of the so-called unparticles [9]. In the limit of high energy the properties of the theory are determined only by dimensionless kinematic quantities, such as scattering angles (pseudorapidities) and ratios of energy scales. However, this is not true at all energies, and this is related to the fact the strong coupling is not a constant, but runs with the energy.

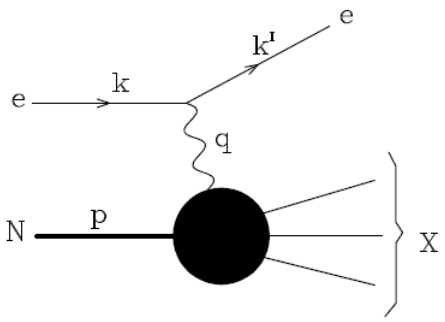

Figure 2.4: Deep inelastic scattering.

Next sections we introduce the QCD lagrangian.

2.1.2 The Lagrangian of QCD

The Lagrangian of QCD is

$$\mathcal{L} = \bar{\psi}_q^i (i\gamma^\mu)(D_\mu)_{ij}\psi_q^j - m_q \bar{\psi}_q^i \psi_{qi} - \frac{1}{4} F_{\mu\nu}^a F^{a\mu\nu}, \tag{2.8}$$

where ψ_q^i denotes a quark field with colour index i, $\psi_q^i = (\psi_{qR}, \psi_{qG}^i, \psi_{qB})^T$, γ^μ is a Dirac matrix that expresses the vector nature of the strong interaction, with μ being a Lorentz vector index, m_q allows for the possibility of non-zero quark masses, D_μ is the covariant derivative in QCD,

$$(D_\mu)_{ij} = \delta_{ij}\partial_\mu - i g_s t_{ij}^a A_\mu^a, \tag{2.9}$$

with g_s the strong coupling (related to α_s by $g_s^2 = 4\pi\alpha_s$), A_μ^a the gluon field with (adjoint-representation) colour index a, and t_{ij}^a proportional to the hermitean and traceless Gell-Mann matrices of SU(3). $F_{\mu\nu}^a$ is the gluon field strength tensor for a gluon with colour index a (in the adjoint representation, i.e., $a \in [1, \ldots, 8]$).

$$F_{\mu\nu}^a = \delta_\mu A_\nu^a - \delta_\nu A_\mu^a + g_s f^{abc} A_\mu^b A_\nu^c, \tag{2.10}$$

Besides the quark-quark-gluon vertex Fig. 2.5(a), one important feature of the QCD lagrangian is the presence of gluon-gluon-gluon vertex Fig. 2.5(b). The

self-coupling of gluons is the reason why the strong coupling constant, $\alpha_s = g2/4\pi$, is large at small momentum transfer (large distances) and decreases at high momentum transfer (small distance) as shown in Figure 2.6.

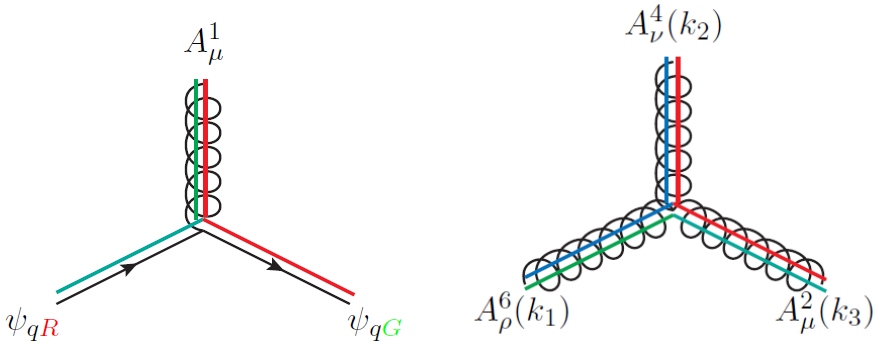

Figure 2.5: Interaction vertices in QCD [9]

This behavior, known as running coupling constant explains two observed phenomena in QCD: asymptotic freedom and color confinement. Asymptotic freedom refers to the weakening of strong coupling at small distances (high momentum transfer). Quarks are surrounded by a cloud with virtual gluons and quarks. Because gluons can split into gluon pairs, the color charge of the cloud is preferentially the color of the quark. Thus, as the quark is probed at smaller distances, less of the color charge of the virtual particles is seen, eventually leaving only the bare color charge of the quark. Therefore the theory has a small coupling at small distance scales.

The coupling of the strong force becomes large at a scale $\Lambda_{QCD} \approx 300MeV$. Λ_{QCD} is approximately the scale where QCD is non-perturbative, because the strong coupling constant $\alpha_s \rightarrow 1$. As the force between the colored objects increases with distance, eventually enough potential energy is present to create a $q\bar{q}$ pair out of the vacuum. This process continues until the quark hadronizes into a color singlet object. The simplest color singlet is the meson, the pairing of a quark and anti-quark of the same color. The next simplest color singlet is a baryon, which is the combination of three quarks or three anti-quarks, each with a different color. Color confinement is a non-perturbative process and it explains

the lack of free quarks in nature; only color singlet objects have been seen.

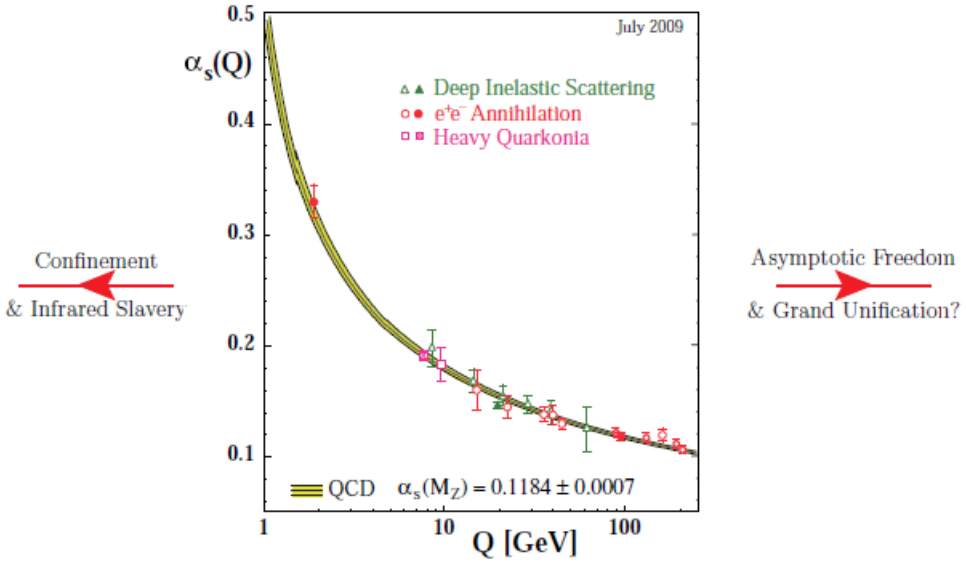

Figure 2.6: Illustration of the running of α_s in a theoretical calculation (yellow shaded band) and in physical processes at different characteristic scales, from [10].

In Quantum Field Theory (QFT), when calculating the Green function using the perturbative Feynman rules, the divergence problem arises from loop diagram momentum integral. The renormalization approach [11] is introduced to the QFT to subtract the ultraviolet divergence in high energy. To absorb the divergence, the physical constants, such as electron charge, mass or coupling constants, would be redefined in terms of quantities measured at a specific kinematic renormalization point, which has a characteristic energy. The characteristic energy is called the renormalization scale μ_R. The renormalization approach must be developed in a specific subtraction scheme.

The procedure is not unique, and different renormalization schemes have been used in the literature, depending on the properties of the parameters needed in the calculation. The observables should be invariant under variations of this scale. However, since the perturbative expansion is performed only to a given order, a theoretical dependence is obtained in pQCD. The strong interaction coupling constant α_s is "running" as a function of the renormalization scale μ_R,

and satisfies the following renormalization group equation (RGE)

$$\mu_R^2 \frac{d\alpha_s}{\mu_R^2} = \beta(\alpha_s) = -(b_0\alpha_s^2 + b_1\alpha_s^3 + b_2\alpha_s^4 + \cdots) \tag{2.11}$$

where b_0, b_1 and b_2 are the 1-loop, 2-loop and 3-loop beta-function coefficients respectively. The minus sign of the coefficients in Equation 2-11 is the origin of asymptotic freedom. The strong coupling α_s decreases as the μ_R increases, which means that quarks can be considered as "free" particles in high energy collisions with large momentum transfer.

2.2 b hadrons production

In 1977 at Fermilab the E288 collaboration observed a peak around 9.5 GeV in the structure of the dimuon spectrum in 400 GeV proton-nucleus collisions. This was quickly interpreted as a bottom (or beauty)-antibottom bound state, $\Upsilon(1S)$ resonance. Since then, the physics of the b quark has been a very rich one, having today a dedicated experiment, LHCb, to study its properties. We present in this section aspects related to the b quark production.

2.2.1 Perturbative calculation for b-quark cross section

In hadron-hadron interactions, heavy quarks ($Q = c, b$) are produced in the hard collisions of one parton from each hadron. The general form of the heavy quark production cross section in collisions between hadrons A and B is [12]

$$\sigma(s) = \sum_{i,j} \int dx_A dx_B d\hat{\sigma}_{ij}(x_A x_B s, m^2, \mu_1^2) F_i^A(x_A, \mu_2) F_j^B(x_B, \mu_2) \tag{2.12}$$

where $\sqrt{s}$ is the total center of mass energy of the $A + B$ hadron system, F_i^A are the structure functions which measure the probability of parton i in hadron A to carry fractional momentum x_A, m is the heavy quark mass, μ_1 and μ_2 are the normalization and factorization scales, and $d\hat{\sigma}_{ij}$ is the short distance partonic cross section for the process $ij \to Q\bar{Q}X$ which occurs at the effective center of

mass energy

$$\hat{s} = x_A x_B s.$$

The terms involved in calculating $d\sigma(s)$ cannot be calculated exactly. Instead, they are expanded into a perturbative power series in the strong coupling constant α_s

$$d\hat{\sigma}_{ij}(\hat{s}, m^2, \mu_1^2) = \alpha_s^2(\mu_1) f_{ij}^{(0)}(\hat{s}, m^2) + \alpha_s^3(\mu_1) f_{ij}^{(1)}(\hat{s}, m^2) + \ldots \quad (2.13)$$

$$F_i^A(x_A, \mu_2) = g_i^{A,(0)}(x_A, \mu_2) + \alpha_s(\mu_2) g_i^{A,(1)}(x_A, \mu_2) + \ldots \quad (2.14)$$

where the functions f, g and the constants μ_1, μ_2 depend upon the scheme used for renormalization and factorization. The indexes (0) and (1) refer to the leading order (LO) and next to leading order (NLO) terms respectively.

To calculate the total heavy quark production cross section is then an exercise in determining the partonic cross section derived to some order in α_s, and convoluting them with the structure functions. This technique was followed using complete $\mathcal{O}(\alpha_s^3)$ calculations by Nason, Dawson and Ellis (NDE) [12; 13].

The previous fixed order calculation is reasonable when the heavy-quark mass is the only relevant mass scale of the specific process, and it fails when the transverse momentum of the heavy quark is much larger than its mass. In that case, the order of neither the heavy quark mass, nor the transverse momentum can be chosen as the renormalization and factorization scales, since the large logarithms in terms of $\alpha_s^2(\alpha_s \log \frac{p_T}{m})^n$ (LL) and $\alpha_s^3(\alpha_s \log \frac{p_T}{m})^n$ (NLL) break the convergence. An approach for treating this problem was proposed in Ref. [14], here the terms to be summed are redistributed between the perturbative and non-perturbative factorization terms. This was however, only a first step, since it was a "massless" approach. The development of the resummation idea and the fixed order calculations lead to the development of FONLL method [15] whose general strategy can be written as

$$\text{FONLL} = \text{FO} + (\text{RS} - \text{FOM0}) \times G(m, p_T) \quad (2.15)$$

where FOM0, the massless limit component, corresponds to the fixed order (FO) terms in the resummation (RS) calculation which should be subtracted to avoid

double counting. A matching procedure is introduced to match the RS and the FOM0 calculations. The function $G(m, p_T)$ is quite a general one, it has to approach unity $\frac{m}{p_T} \to 0$ and to suppress the logarithm terms in the low p_T range. The result from this method can then be described as

$$\begin{aligned} \frac{d\sigma}{dp_T^2} &= A(m)\alpha_s^2 + B(m)\alpha_s^3 + \\ &+(\alpha_s^2 \sum_{i=2}^{\infty} a_i(\alpha_s \log\frac{\mu}{m})^i + \alpha_s^3 \sum_{i=2}^{\infty} b_i(\alpha_s \log\frac{\mu}{m})^i) \times G(m, p_T) \end{aligned} \quad (2.16)$$

where coefficients $a(m)$ and $b(m)$ are extracted from the LO and NLO calculations and the coefficients a_i and b_i depend on the colliding center of-mass energy s, p_T and scales μ.

2.2.2 The handling of non-perturbative effects

Parton distribution functions

Parton distribution functions (PDFs) describe the longitudinal momentum carried by various partons in a hadron. $f_\alpha^A(x_\alpha, \mu_F)$ is the probability distribution for a parton of flavor α to have a momentum $x_\alpha P_{proton}$ at energy scale μ_F . The PDFs change or evolve as a function of the energy scale of the interaction because shorter distances within the proton are probed. As the energy of the probe increases, the effects of the emission of softer gluons from a quark and the splitting of gluons in $q\bar{q}$ pairs are resolved. Therefore, the PDFs populate lower and lower regions of x as the factorization scale, μ_F, increases. The evolution of the PDFs are determined by a set of evolution equations, first described by Altarelli and Parisi [16], which are solved in perturbative QCD to the same fixed order as the parton cross section. As the PDFs are non-perturbative, the functional form of the PDFs are empirical and must be fit from experimental measurements. As no experiment is sensitive to all partons over the entire x region, the PDFs have to be determined by a global fit to wide range of Deep Inelastic Scattering (DIS) experimental data. There are collaborations specialized in performing such global analyses like CTEQ [17] and MRST [18] collaborations. HERA collaboration also

provides a set of PDFs [19] using experimental data from DESY.

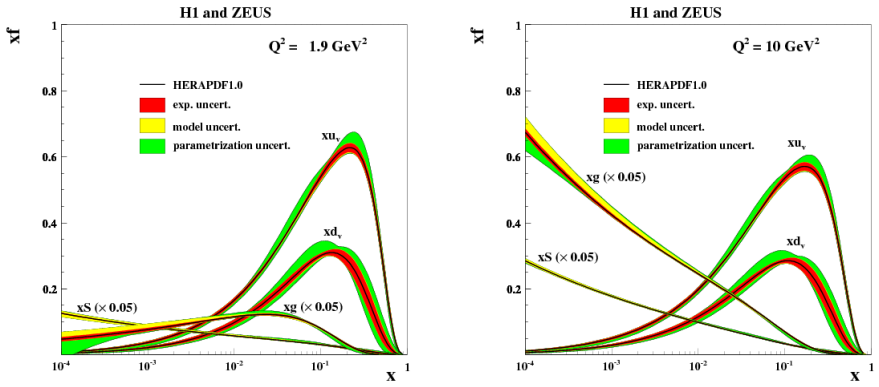

Figure 2.7: The parton distribution functions from HERAPDF1.0, xu_v,xd_v,$xS = 2x(\bar{U} + \bar{D})$, xg, at $Q^2 = 1.9\ GeV^2$ (left) and $Q^2 = 10\ GeV^2$ (right). The gluon and sea distributions are scaled down by a factor 20. The experimental, model and parametrization uncertainties are shown separately.[19]

Fragmentation

b and $\bar{b}$ quarks can not exist as free particles due to the quark confinement. The process where a quark forms a bound state (hadron) with another antiquark or a pair of quarks is called hadronization. The hadronization process happens much later than the $b\bar{b}$ quark pair creation and doesn't affect the inclusive $b\bar{b}$ production cross-section. The creation of quark pairs and their hadronizations are called fragmentation, which can be described in the parton model by a fragmentation function.

Many fragmentation functions exist and differ according to kinematic arguments used to derive them. Two commonly used fragmentation functions are introduced by Peterson et al. [14] and by Bowler [15]. The fragmentation functions are assumed to be universal, that is to have no dependence on the incoming particle. Thus, fragmentation functions are tuned using measurements of e^+e^- collisions at the Z pole [16] where the measurement of the fraction x is best determined. The fragmentation functions evolve with the scale of the fragmentation (μ_H) in a manner similar to the PDFs, with a set of equations, similar

to the Altarelli-Parisi ones. These functions should be calculated to the same fixed order as the PDF and parton cross section. The quantity μ_H is typically set to the same value as the renormalization/factorization scale. The Peterson fragmentation function assumes that the energy lost by the heavy quark due to the light antiquark is small. The transition amplitude is determined by the energy difference between the incoming partons and the outgoing hadrons. The Peterson fragmentation function is

$$f(z) = \frac{1}{z(1 - \frac{1}{z} - \frac{\epsilon_Q}{1-z})^2} \tag{2.17}$$

where ϵ_Q corresponds to the ratio of the light quark mass with respect to the heavy quark mass.

Experimental inputs are required to improve the accuracy of fragmentation functions. And then the functions can be used to give theoretical predictions for more experiments. The hadronization fractions for B hadrons, which are the branching fractions of $\bar{b} \to B$, are currently consider to be [20]:

$f_{B^0} \sim f_{B^+} \sim 40\%$, $f_{B_s^0} \sim 11\%$, $f_{b-baryon} \sim 8.5\%$.

These fractions need feedback from the LHC experiments. The Λ_b production cross-section measurements in this thesis can be extended to extract hadronization fraction results.

Monte Carlo simulation

The equation 2.14 indicates a path for calculating the cross-section for the heavy quarks production. Perturbative calculations are appropriate for the partonic cross-section, while for partonic distribution functions and hadronization functions one must rely on different experimental input and phenomenological methods. This procedure can be sometimes difficult and not optimal, if we are interested in new models or we worry about the computational time. Thus, general frameworks were developed to generate events for simulation studies. These event generators treat the full process of collision, the hard interaction of the partons, the emission of the radiation, the formation of jets, hadronization, underlying events. Currently, the most used event generators are Pythia [21; 22], Herwig++ [23] and Sherpa [24], which propose alternative solutions for the split-

ting mentioned above and are useful for making comparisons. They are built as modular packages which can be sometimes interchanged between themselves and more important they have interfaces that allow the implementation of a specific phenomenon in an easy manner when new solutions are proposed. However, they are still developing and sometimes they don't have implemented specific processes, or their very core idea cannot be easily made compatible with the theoretical ones. For instance, with respect to the hard interaction, all generators offer LO calculation, but not necessarily NLO calculations, while the FONLL scheme is not fully implemented in either of them. Careful evaluation has to be made when choosing a generator for a specific problem or when interpreting the differences between their predictions.

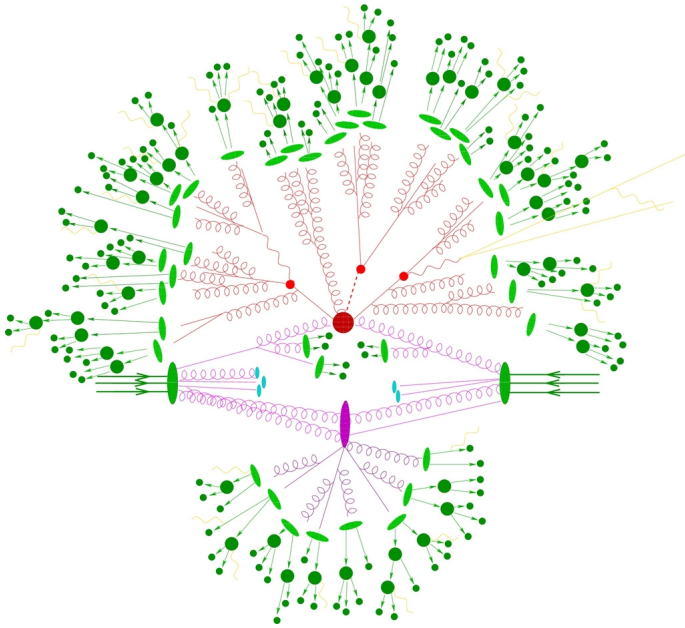

Figure 2.8: Pictorial representation of a typical event at LHC as produced by an event generator. The hard interaction (big red blob) is followed by the decay of both top quarks/Higgs boson (small red blobs). Additional hard QCD radiation is produced (red) and a secondary interaction takes place (purple blob) before the final-state partons hadronise (light green blobs) and hadrons decay (dark green blobs). Photon radiation occurs at any stage (yellow)[24].

The general view of the event generators on the typically selected events at

LHC can be explained by Fig. 2.8. The main idea is to rely on the factorization of such events into different well-defined phases, corresponding to different kinematic regimes. In the description of each of these phases different approximations are employed. We list below the typical phases used in a generator in corespondence with Fig. 2.8.

- Hard process: In general, the central piece of the event simulation is provided by the hard process (the dark red blob in the figure), which can be calculated in fixed order perturbation theory in the coupling constants owing to the correspondingly high scales. This part of the simulation is handled by computations based on matrix elements, which are either hard-coded or provided by special programs called parton-level or matrix-element (ME) generators.

- Parton showers: The QCD evolution described by parton showers then connects the hard scale of coloured parton creation with the hadronization scale where the transition to the colourless hadrons occurs. The parton showers model multiple QCD bremsstrahlung in an approximation to exact perturbation theory, which is accurate to leading logarithmic order.

- Hadronization: At the hadronization scale, which is of the order of a few Λ_{QCD}, QCD partons are transformed into primary hadrons (light green blobs) by applying purely phenomenological fragmentation models having typically around ten parameters to be fitted to data.

- Decays: The primary hadrons are decayed finally into particles that can be observed in detectors. In most cases, effective theories or simple symmetry arguments are invoked to describe these decays.

- Initial/final state radiation: Another important feature associated with the decays is QED bremsstrahlung, which is simulated by techniques that are accurate at leading logarithmic order and, eventually, supplemented with exact first-order results.

- Underlying events: A particularly difficult scenario arises in hadronic collisions, where remnants of the incoming hadrons may experience secondary

hard or semi-hard interactions. This underlying event is pictorially represented by the purple blob in Fig. 2.8. Such effects are beyond QCD factorization theorems and therefore no complete first-principles theory is available. Instead, phenomenological models are employed again, with more parameters to be adjusted by using comparisons with data.

For this thesis we used Pythia event generator and also compared the results with the prediction from FONLL calculation from [15], and NLO prediction from POWHEG [25; 26; 27].

The software for high energy physics application has a long history, it is constantly evolving and new data and models are introduced. Working in this fields often implies that one should be familiar with many different libraries and computing frameworks implementing the steps described above. A random list of currently used software libraries can be seen in Fig. 2.9 in the form of a cloud text, which displays their number and relative importance.

Figure 2.9: Cloud words for high energy physics software.

2.2.3 Production studies at LHCb

LHCb experiment, started in 2010, ended successfully the first years of its b-physics program. The registered data was $37pb^{-1}$ in 2010 and $1.1fb^{-1}$ in 2011 at 7TeV, and $2.1fb^{-1}$ at 8TeV in 2012. Large samples of $c\bar{c} \sim 10^{12}$ and $b\bar{b} \sim 10^{11}$ were collected, thus making LHCb a real flavour factory.

One of the first analysis performed at LHCb was the measurement of the total cross section for b quark production [28]. The analysis exploits the large branching ratios for the transition $b \to c$ and reconstructs the semi-inclusive channel $D^0 X \mu^- \bar{\nu}$. The result in the pseudorapidity interval $2 < \eta < 6$ and integrated over all transverse momenta, the average cross-section to produce b-flavored or $\bar{b}$-flavored hadrons, was found to be $\sigma_{b\bar{b}} = 75 \pm 5 \pm 13)\mu b$. Extended to the full space this result becomes $\sigma_{b\bar{b}}^{4\pi} = 284 \pm 20 \pm 49)\mu b$. A second determination of the total cross section was obtain in the measurement of J/ψ production [29] separating the prompt J/ψ from the component with a displaced secondary vertex. The result found is in excellent agreement with the above result.

Another direction was the study of ratio of fragmentation factors. In a first analysis [30] there were studied the ratios of strange B meson to light B meson production $f_s/(f_u + f_d)$ and Λ_b^0 baryon to light B meson production $f_{\Lambda_b}/(f_u + f_d)$ as a function of the charmed hadron-muon pair transverse momentum p_T and the b hadron pseudorapidity η, for p_T between 0 and 14 GeV and η between 2 and 5. A second analysis measured the ratio f_s/f_d comparing the decay rate of the exclusive channels $B_s^0 \to D_s^- \pi^+$ to $B^0 \to D^- K^+$ and of the channels $B_s^0 \to D_s^- \pi^+$ to $B^0 \to D^- \pi^+$. Together these two analysis provided the best value for the ratio f_s/f_d, which allowed to reach new best limits in the important flavour changing neutral current (FCNC) decay $B_s \to \mu\mu$.

For the exclusive production of b hadrons, so far, only one analysis was published [31], the measurement of $B^\pm$ production in the channel $B^\pm \to J/\psi K^\pm$. More interesting results for the other mesons await the final approval [32]. In this thesis we present the measurement of the Λ_b production cross section.

2.3 Λ_b phenomenology - a literature review

From the beginning, the physics of baryons had an important contribution to the understanding/conception of QCD, as suggested in Section 2.1.1, but it became soon too difficult when the complexity of the three-quark system was realized and the physics of mesons was preferred. However, baryons as opposed to mesons are everywhere around us and the interest for the baryons was reborn in the last years. The reasons are that the baryons are sufficiently simple systems in

which the quintessentially nonabelian character of QCD is manifest, but they are "sufficiently complex to reveal physics hidden from us in the mesons" [33]. The advent of LHC experiments producing large samples of c and b-baryons allows a further investigation of QCD degrees of freedom.

The result from this thesis, the measurement of the production cross section of the Λ_b baryon, follows the interest of testing the validity of pQCD calculations at these new energies and in a unique phase space for the baryons which contain the b quark. The decay mode chosen for this is $\Lambda_b^0 \rightarrow J/\psi\Lambda^0$, see Fig. 2.10, which although not the most abundant, has the advantage that can be well reconstructed and relates tightly to a list of other interesting applications.

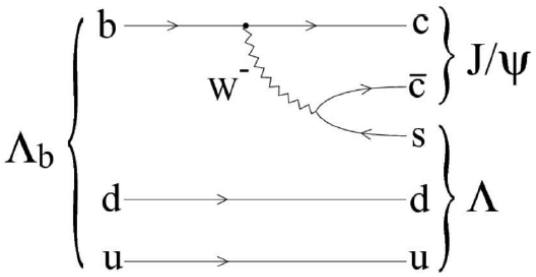

Figure 2.10: Feynman diagram for the weak Λ_b decay.

The present analysis is part of a more general program which motivates our work and includes:

i) spectroscopy; measurement of masses, lifetime, states

ii) confirming Λ_b^0 decay modes

iii) relative production rate measurement of baryons (Stone)

iv) baryon fragmentation factor f_{baryon}

v) polarization studies $\Lambda_b^0 \rightarrow J/\Psi\Lambda^0$

vi) CP violation in direct searches $\Lambda_b^0 \rightarrow J/\Psi\Lambda^0$

vii) time reversal violations $\Lambda_b^0 \rightarrow J/\Psi\Lambda^0$

viii) SM checks in radiative decays $\Lambda_b^0 \rightarrow J/\Psi\Lambda^0$

ix) search for charmless hadronic b-meson decays

x) forward production of beauty baryons in pp collisions [34; 35]

The production of the Λ_b baryons is an important step of this program since it provides us with the basic tools for performing these studies.

In the following subsections of this Chapter, we will review some directions of the Λ_b program. We grouped the studies into *Checks of the Standard Model*, Section 2.3.1, and *Searches for New Physics*, Section 2.3.2. Since, virtually, any unexpected result could be interpreted as a hint for NP in Section 2.3.2 we choose to select only those studies which explicitly refer to a beyond SM model.

2.3.1 Checks of the Standard Model

The Λ_b was first observed in a pp experiment at CERN ISR [36; 37] and further studied at LEP and Tevatron experiments. The available samples didn't allow a full investigation of its properties. The current accepted values, including LHC measurements, are [20]: for mass $m = 5619.4 \pm 0.7 MeV$, for mean life $\tau = (1.425 \pm 0.032) ps$, while the quantum numbers $I(J^P)$ were not measured yet ($0(\frac{1}{2}^+)$ is the quark model prediction).

We choose to present in this section studies regarding the properties of Λ_b, liftime and masses, production mechanisms and observables.

Spectroscopy

In the spectator model, the decay of b-flavored hadrons H_b is governed entirely by the flavour changing $b \rightarrow Wq$ transition ($q = c, u$), thus the lifetimes of the b-flavored hadrons are the same in the first approximations. This is very different than the s and c systems where there are differences of 2-3 order of magnitude between most stable and less stable resonances. The current theoretical calculations for the decay rates are done in the framework of Heavy Quark Expansion

(HQE). These are written as a series in Λ_{QCD}/m_b powers [38]:

$$\Gamma_{H_b \to f} = |V_{CKM}|^2 \sum_n c_n^{(f)} (\frac{\Lambda_{QCD}}{m_b})^n \langle H_b|O_n|H_b\rangle, \tag{2.18}$$

where $c_n^{(f)}$ coefficients are known as Operator Product Expansion coefficients, and can be calculated perturbatively, i.e as series of $\alpha_s(m_b)$ powers. The non-perturbative physics is encoded in $\langle H_b|O_n|H_b\rangle$ expectation values and can be calculated using techniques like lattice QCD or QCD sum rules [39].

The HQE theory can explain the spectator picture, i.e in the $m_b \to \infty$ limit the H_b lifetimes are the same, and the fact that the differences between baryon and meson appear in the order Λ_{QCD}^2/m_b^2. Differences between mesons start to appear at Λ_{QCD}^3/m_b^3 order. However, there is a need for more precise non-perturbative calculations to match the current/future experimental precision. Lifetime measurements of b hadrons test the validity of HQE and also they can be used to supply input for the extraction of elements of the Cabibbo-Kobayashi-Maskawa (CKM) quark mixing matrix.

As regard Λ_b lifetime, there was a long standing puzzle [40]: while the theoretical calculations of $\tau(B^+)/\tau(B^0)$ agreed with the experimental measurements, not the same happened with $\tau(\Lambda_b^0)/\tau(B^0)$ ratio which differed by 2σ by the experimental value. More recent calculations [41] reduce this difference, but still there is a puzzle since the most precise value for the lifetime of Λ_b from CDF [42] is much higher than the world average value. LHCb has measured the lifetime in the decay $\Lambda_b^0 \to J/\psi\Lambda$ with 2010 data and is expected to reach a better precision with the next sets of data.

On the spectroscopy side, the heavy b-hadrons can be seen as the atomic model of QCD, where the heavy quark is surrounded either by a light anti-quark, to form a b meson or by a di-quark pair, to form a bottom baryon. The higher states above the background can be predicted using heavy quark effective theory (HQET), non-relativistic and relativistic potential models, $1/N_c$ expansion, sum rules and lattice QCD calculations [43]. The experimental findings help thus improving these models. Before LHC only a few b-baryons states were observed Λ_b, $\Sigma_b^{(*)\pm}$, $\Xi_b^{-,0}$, Ω_b [44] and very few decay modes. The CDF and D0

measurements of Ω_b mass were in disagreement of nearly 6σ. LHCb [45] measured Ξ_b, Ω_b solving the controversy about Ω_b mass, which was found to be $M(\Omega_b) = 6050.3 \pm 4.5_{stat} \pm 2.2_{syst} MeV/c2$. LHCb [46] has also observed new resonances $\Lambda_b^{*0}(5912)$ and $\Lambda_b^{*0}(5920)$, and more new decay modes and resonances are being searched for. Recently, the CMS Collaboration [47] has found the excited state Ξ_b^{*0}.

Baryon fragmentation factors

The fragmentation process, in which a primary b quark forms either a $b\bar{q}$ meson or a bq_1q_2 baryon, cannot be reliably predicted because it is driven by strong dynamics in the non-perturbative regime. Knowledge of the fragmentation functions allows us to relate theoretical predictions of the $b\bar{b}$ quark production cross-section, derived from perturbative QCD, to the observed hadrons [30]. Many b-physics analyses need these fractions as input. Ratios of fragmentation factors allows us to perform precise $\bar{B}_s^0$ branching fraction measurements (due to good knowledge of many absolute branching fractions of B^- and $\bar{B}^0$ decays).

In principle fragmentation fractions can depend on energy and phase space region or energy, although it is often assumed that the fractions of these different species are the same in unbiased samples of high-p_T b jets originating from Z^0 decays, from pp collisions at the Tevatron, or from pp collisions at the LHC. This hypothesis is plausible under the condition that the square of the momentum transfer to the produced b quarks, Q^2, is large compared with the square of the hadronization energy scale, $Q^2 \gg \Lambda_{QCD}^2$. These fractions, f_u for B^-, f_d for B^0, f_s for B_s^0 and f_{baryon} for all baryons, were previously determined at LEP and Tevatron. They should obey the completeness relation:

$$f_u + f_d + f_s + f_{baryon} = 1 \tag{2.19}$$

The averaged values from LEP and Tevatron were [20]: $f_u \sim f_d \sim 40\%$, $f_s \sim 11\%$, $f_{b-baryon} \sim 8.5\%$.

However, for the baryon case it was found at Tevatron that the ratio $f_{\Lambda_b}/(f_u + f_d)$ has a dependency with p_T, see Fig. 2.11. LHCb has also measured [30] this fragmentation factor using the semileptonic decays $B^- \to D^0\mu^-\bar{\nu}X$, $B^0 \to$

$D^+\mu^-\bar{\nu}X$, $\Lambda_b \to \Lambda_c\mu^-\bar{\nu}X$. They confirm the findings of Tevatron on p_T dependency.

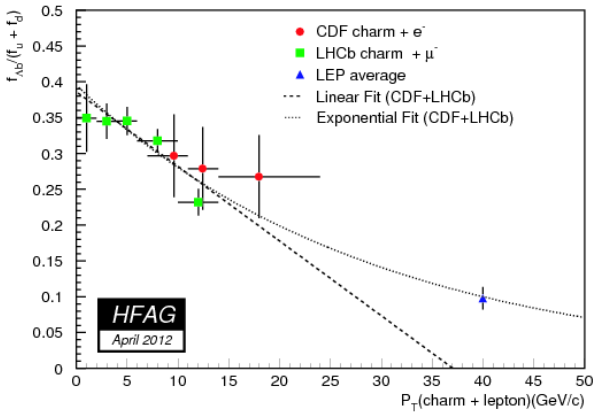

Figure 2.11: Ratio of production fraction $f_{\Lambda_b}/(f_u + f_d)$ as a function of p_T of the lepton+charm system for LEP, CDF and LHCb data. The exponential and linear fits are explained in Ref. [38].

This result still has to be checked since for the other ratios, which can be formed in Eq. , no such dependency was put in evidence.

The decay studied in this thesis can be used to check this behavior measuring the p_T dependency of the following ratio $\frac{\sigma(\Lambda_b^0)B(\Lambda_b^0\to J/\psi\Lambda^0)}{\sigma(B^0)B(B^0\to J/\psi K_S^0)}$. Another extension, would be to study the $\sigma(\Xi_b^-)B(\Xi_b^- \to J/\Psi\Xi^-)$, $\sigma(\Omega_b^-)B(\Omega_b^- \to J/\Psi\Omega^-)$ decays in relation to $\Lambda_b^0 \to J/\Psi\Lambda^0$.

Non-factorisable effects in Λ_b production

In the Introduction we presented a result from CDF in which an unexpected peak appears in the invariant mass of jet pairs plus a W analysis. A second example from Tevatron [48; 49] which contradicts the SM and hints to the physics beyond SM [50; 51] is the forward-backward asymmetry in top quark-antiquark production. The top quark tends to follow the proton direction, while the antitop tends to follow the antiproton direction. The effect grows with increasing effective mass $m_{t\bar{t}}$ of the top-antitop pair, and with increasing rapidity difference between the top and antitop. The observed effect is about three times as large as predicted by next-to-leading-order QCD, but with the same sign.

In the Reference [34], it is suggested that this effect could still be explained within SM if one takes into considerations the non-factorizable effects in $t\bar{t}$ production. To check this it is suggested to look at other manifestations of these effects that should appear for example in "enhanced multiparticle production between the t and p remnants or the $\bar{t}$ and $\bar{p}$ remnants ... [or] a forward-backward or charge asymmetry in baryon/antibaryon production" [34].

If this were the case the LHCb could measure Λ_b over $\bar{\Lambda}_b$ and should see an increase with $|y|$. This measurement is a natural continuation of the study from this thesis and it is expected to be done with the larger datasets from 2011 and 2012.

2.3.2 Searches for New Physics

Fourth generation effect on Λ_b decays

The rare decays of B mesons involving flavor changing neutral current (FCNC) transitions are of great interest to look for possible hints of new physics beyond the SM. In the SM, the FCNC transitions arise only at one-loop level, thus providing an excellent testing ground to look for new physics. Therefore, it is very important to study FCNC processes, both theoretically and experimentally, as these decays can provide a sensitive test for the investigation of the gauge structure of the SM at the loop level.

The Reference [52] analyses the rare Λ_b decays in the context of SM4, a simple extension of the SM with a fourth generation of quarks. The decays studied were $\Lambda_b \to \Lambda\pi$, $\Lambda_b \to pK^-$, $\Lambda_b \to \Lambda\gamma$ and $\Lambda_b \to \Lambda l^+ l^-$. It was found that in this model the branching ratios of the various decay modes considered are significantly enhanced from their corresponding SM values and would be favorable for finding NP at LHCb.

Extra dimensions and Λ_b decays

One of the simplest models assuming extra dimensions is the Appelquist, Cheng and Dobrescu (ACD) model [53]. In this model the SM fields (both gauge bosons and fermions) propagate in the extra dimensions and only one extra dimension compactified on a circle of radius R is considered.

In Reference [54] the ACD model is assumed and a comprehensive analysis of the $\Lambda_b \to \Lambda l^+ l$ transition is made. The observables branching ratio, forward-backward asymmetry, double lepton polarization asymmetries and polarization of the Λ baryon are analyzed in terms of compactification radius and corresponding form factors.

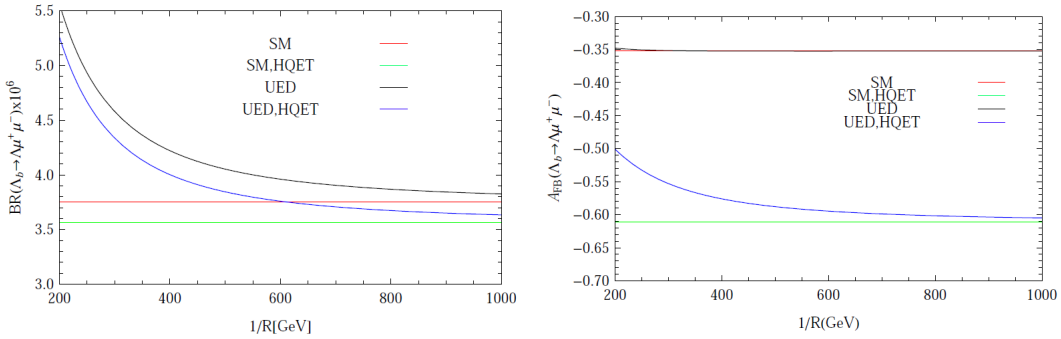

Figure 2.12: Branching ratio and forward-backward asymmetry for $\Lambda_b \to \Lambda l^+ l$ in ACD extra dimension model, from Ref. [54].

In Fig. 2.12 it can be seen the sensitivity of the branching ratio and forward-backward asymmetry observables where the muons werr used for the lepton case. The plot shows that the proposed observables are sensitive in a large range of values for the compactification factor $1/R$.

Chapter 3

LHCb experiment @ CERN

Modern high energy physics experiments are developed arround large infrastructures which can span distances of the order of kilometers. In this chapter we mainly present the LHCb detector from the point of view of the principal subdetectors, their physics principles and of the operation work-flow of the experiment. It is one of the main detectors that uses data from the Large Hadron Collider (LHC) accelerator at CERN, which is at present the world most powerful accelerator. Thus, for fixing the context, we begin this chapter with a short description of CERN and LHC and of the other experiments that use the data from the LHC accelerator. For a more general view, we also introduce CERN laboratory, followed by a short description of the LHC accelerator and of the other LHC experiments.

Before LHC accelerator and LHCb experiment large laboratories around the world, running high energy experiments have also contributed to the b physics program; a list is given here: KEK, Japan [55]; SLAC, Stanford [56; 57]; Fermilab, Chicago [58; 59]; Cornell University [60]; DESY, Hamburg [61; 62; 63; 64]; BES, Beijing [65]; CERN, Geneva [66; 67; 68; 69; 70].

3.1 LHC and CERN

CERN, Conseil Européen pour la Recherche Nucléaire, is an international laboratory dedicated to studies of nuclear physics and particle physics. It was founded

in 1954, nearby Geneva, as an European initiative for strengthening the scientific cooperation between European research institutes and it has, now, 20 member states and cooperation with institutes from other continents too. Overall, a total of 10000 visiting scientists from 608 institutes and universities from 113 countries around the world use CERNs facilities, amounting to half of the worlds particle physicists. Moreover, CERN employs around 2400 people between scientific and technical staff. CERN has also become a fertile ground for other types of researches which include vacuum technology, superconducting magnets, computing, cryogenics and electrical, electronics civil and mechanical engineering etc. The most well known technologies to the public which have originated from CERN are world wide web (www) protocol a key piece of the Internet communication today and the positron emission tomography (PET), a nuclear medical imaging technique that produces a three-dimensional image or picture of functional processes in the body.

The LHC at CERN is a two-ring superconducting hadron accelerator and collider of approximately 27 km in circumference, situated underground crossing the Swiss and France borders nearby Geneva. It is currently the largest collider ever built and it is used to accelerate protons and heavy ions. The two rings intersect in four points where the beams traveling in opposite directions can collide. The LHC was designed to provide an energy of 14 TeV in center-of-mass and an instantaneous luminosity of $\mathcal{L} = 10^{34} cm^2 s^{-1}$. In 2009 LHC started the official running colliding the beams at 900GeV and in the following years the energy increased to 7 TeV and then to 8 TeV in the center of mass. The nominal values are expected to be reached after a long shut-down of 2 years, 2013-2014, when repairments and upgrades are expected to be done.

LHC can achieve these high performances in energy and beam intensities using a chain of smaller accelerators and storage rings, see the Fig. 3.2. The source of the protons is a cylinder of hydrogen gas. The gas is ionized to obtain protons, which are then fed into the Linac2. Linac2 accelerates the protons until they reach an energy of 50 MeV before injecting them into the Proton Synchrotron Booster (PSB). When they reach 1.5 GeV the protons are fed into the Proton Synchrotron (PS), which takes the energy up to 25 GeV. Finally the Super Proton Synchrotron (SPS) increases the energy to 450 GeV before injecting the protons

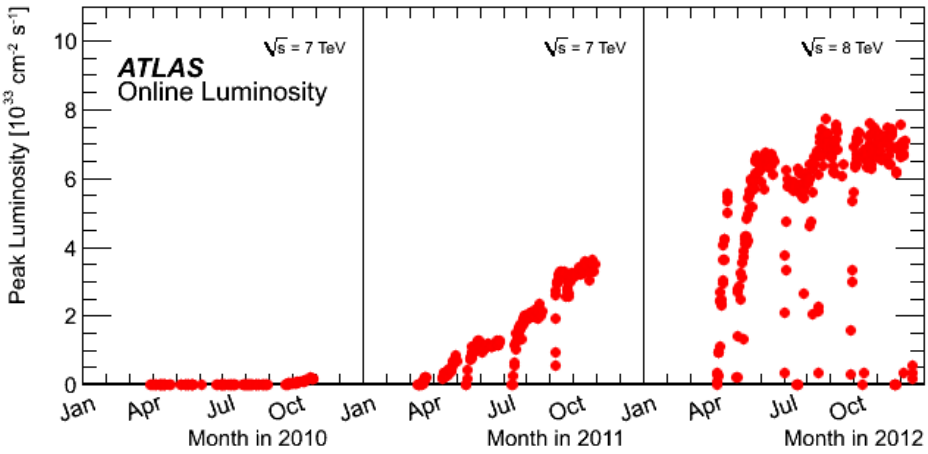

Figure 3.1: Instantaneous luminosity versus delivered by LHC at IP1 point; statistic taken from ATLAS site

into the LHC.

In the four intersection points there are underground caverns hosting the detector complexes of the four main LHC experiments, ATLAS, ALICE, CMS, LHCb. The primary goals of the LHC and its experiments are to test the SM description of particle physics and to look for direct or indirect evidence of the existence of new particles and interactions:

- the only missing particle of SM, the Higgs boson it is expected to be observed at LHC, some indications of higgs-like particle have already been reported by ATLAS [1] and CMS [2];
- different theories beyond SM predict particles in the range accessible to LHC, at the moment only exclusion limits have been set for these particles.
- alternative tests of SM and indirect searches for New Physics can be done by over-constraining SM identities measuring the same quantities in different ways. These strategies are followed in particular by LHCb, the dedicated b-physics experiment. First results however confirm that the possible New Physics effects should be very small at these scales [71];
- in dedicated runs the LHC will provide heavy ion collisions (e.g. Pb-Pb),

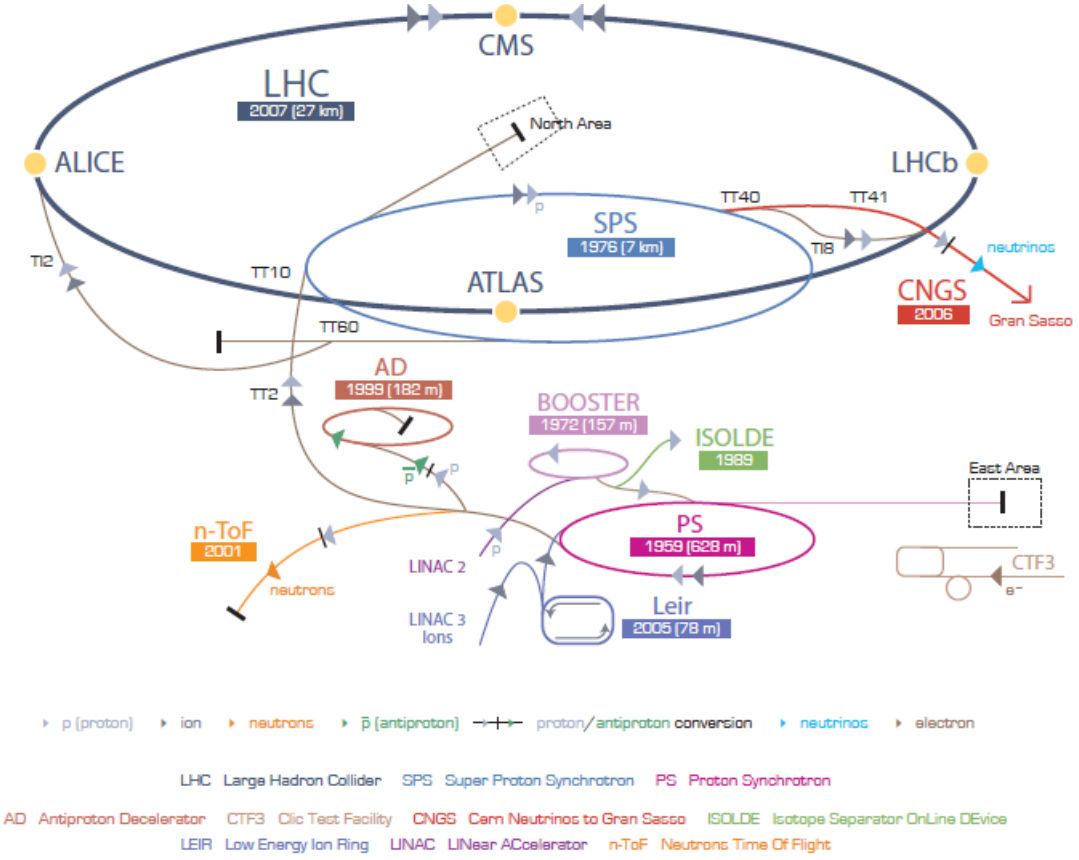

Figure 3.2: Preacceleration chain and the LHC ring.

instead of pp collisions, to study the behaviour of nuclear matter in extreme conditions and the formation of a quark-gluon plasma.

A short description of the experiments using the LHC is given below. The four major experiments located at the four interaction points are:

- ATLAS: A Toroidal LHC Apparatus System [72] is a general purpose experiment, dedicated to Higgs boson search and discovery of physics beyond the SM, such as the heavy W and Z-like objects, the super symmetric particles, the components of the fundamental fermions and detailed studies of the top quark. The primary goal is to operate at high luminosity, but the detector is conceived to assure performance in the full operational range

of LHC being actually the LHC biggest detector (diameter of 25 m for a length of 44 m), while using a toroidal magnetic field.

- CMS: the Compact Muon Solenoid [73] has a physics program similar to ATLAS. It uses a general-purpose detector to investigate a wide range of physics, including the search for the Higgs boson, extra dimensions, and particles that could make up dark matter. Although it has the same scientific goals as the ATLAS experiment, it uses different technical solutions and design of its detector magnet system to achieve these. In fact, it is the heaviest LHC detector (12500 tonnes) and has a strong magnetic field (4 T).

- LHCb: the Large Hadron Collider beauty experiment it will be described with more detail in Section 3.2.

- ALICE: A Large Ion Collider Experiment [74], dedicated to study of QGP, the state of matter appearing in ion collisions, namely the physics of strongly interacting matter at extreme energy densities, where the formation of a new phase of matter, the quark-gluon plasma, is expected. The existence of such a phase and its properties are a key issue in QCD for the understanding of confinement and chiral-symmetry restoration. For this purpose, the collaboration intends to carry out a comprehensive study of the hadrons, electrons, muons and photons produced in the collision of heavy nuclei. The challenging issue is the high track multiplicity in Pb-Pb collisions.

Finally there are other two smaller experiments which we remind them here:

- LHCf: the Large Hadron Collider forward experiment [75]is the smallest of the LHC experiments. It is meant to to perform a measurement of the very forward production cross sections and energy spectra of neutral pions and neutrons generated in the 'forward' region of collisions. These studies are needed to check the hadronic model used to understand the ultra energetic cosmic rays. LHCf consists of two small detectors, located 140 m upstream and downstream of the ATLAS detector.

- TOTEM: the TOTal Elastic and diffractive cross section Measurement experiment [76] is dedicated to the measurement of the total pp cross section with a luminosity-independent method based on the Optical Theorem. Moreover, its physics program aims at obtaining a deeper understanding of the proton structure by studying elastic scattering processes with large momentum. It is located near the CMS interaction point, and covers the extreme forward region.

LHC start-up

Constructing and running a collider of LHC magnitude is a very complex entreprise which wouldn't be possible without the experience gather in the last 50 years from the previous machines built at CERN and without the the other large high energy facilities. Although it hasn't reach yet the nominal parameters the LHC has surpassed the performance expectations, delivering stable beams over long periods, 10-12 hours and enough integrated luminosity to confirm or exclude the hypothesis of a Higgs boson below 500 GeV.

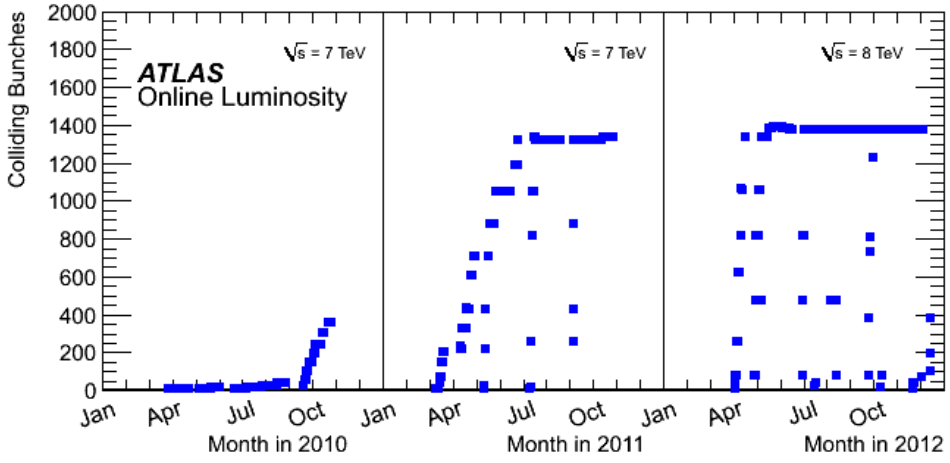

Figure 3.3: Number of bunches in LHC beams versus time; statistic taken from ATLAS site.

3.2 The LHCb detector and performances

The LHCb experiment consists in a single arm spectrometer [77] designed to search New Physics through the study of very rare decays of b and c-flavored hadrons and precision measurements of CP-violating observables [78].

As explained in Sec. 2.2 according to the parton model, in the hadronic collisions the interactions take place at the level of the partons (gluons and quarks), thus in general the $b\bar{b}$ quark pairs are produced parallel to the collision axis. This can be easily seen from Fig. 3.4, which shows the angular correlation between the two b quarks. The LHCb takes advantage of this fact choosing a forward angular coverage from approximately 10 to 300 (horizontally) and 250 (vertically) mrad. Almost 40% of the $bp\bar{a}ir$ are accepted by such geometrical setup.

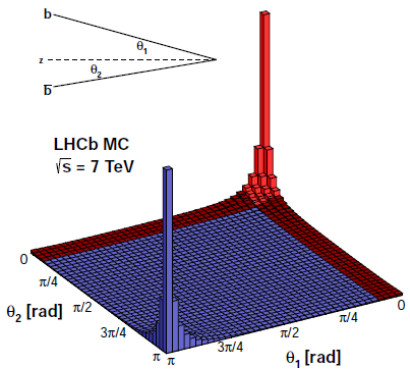

Figure 3.4: $b\bar{b}$ correlation in pp collisions at LHC.

To accomplish its program of studying the b-physics, LHCb has a high-resolution vertex detector, which allows precise reconstruction of secondary vertices and several systems dedicated to precise particle identification in order to distinguish as many channels as possible. Another operational and design feature of LHCb is to run at low pile-up conditions (small number of pp interactions per bunch crossing), usually less than 3. Thus the events can be well reconstructed and the subdetectors are protected against the radiation damages. The LHCb has acquired most of the data at the designed instantaneous luminosity of $\mathcal{L} = 2 \cdot 10^{32}$, or higher, which was lesser than the one needed by ATLAS or CMS. This was made possible by defocusing the beams at the interaction point and

leveling the luminosity. In the first years of running 2010-2012 (Run I), LHCb recorded around $5 \cdot 10^{12}$ pairs of $c\bar{c}$ and $2 \cdot 10^{11}$ pairs of $b\bar{b}$ thus becoming a truly flavour factory at CERN. The evolution of the integrated luminosity with time is seen in Fig. 3.5.

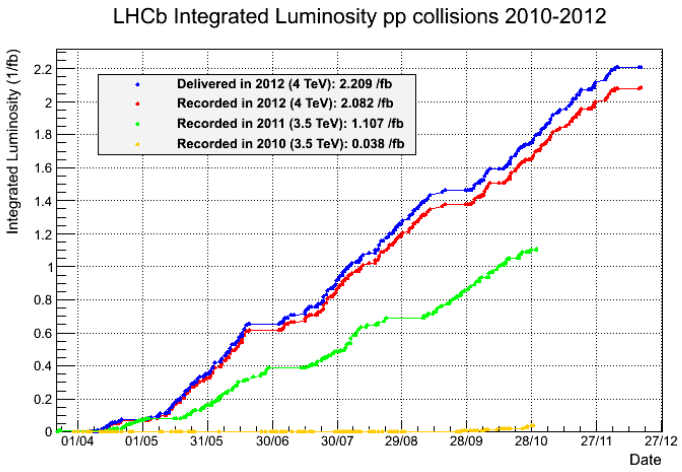

Figure 3.5: Integrated luminosity in *pp* collisions in the first three years of running.

The collision point at LHCb, which is also the origin of the coordinate system, is surrounded by subdetectors arranged along the z axis and perpendicularly on it. In the left side, $z < 0$, see Fig. 3.6, there are only vertex locator (VELO) planes. On the right side, $z > 0$, from left to right these are the VELO planes, the upstream Ring-Imaging Cherenkov detector (RICH1), silicon Tracker Turicensis planes, the magnet, three tracking stations (T1-T3), the downstream RICH2, the preshower (SPD/PS), the electromagnetic calorimeter (ECAL), the hadronic calorimeter (HCAL) and the muon detectors (M1-M5). A beam pipe traverses the whole detector except the VELO which is located inside a vacuum vessel connected to the beam pipe. From a functional point of view these subdetectors perform the following tasks: triggering, track reconstruction and particle identification. Triggering means to select the interesting events from ordinary soft collisions events, i.e. trigger the data registration. Following a collision the stable particles which are passing the subdetectors interact with matter, these traces are then interpreted by tracking algorithms and tracks are formed. LHCb

has also some dedicated subdetectors to provide information on the type of particles which were produced. These information together with track properties are combined in constructing a global particle identification function.

In the rest of this section we present some details on subdetectors and functions that they provide.

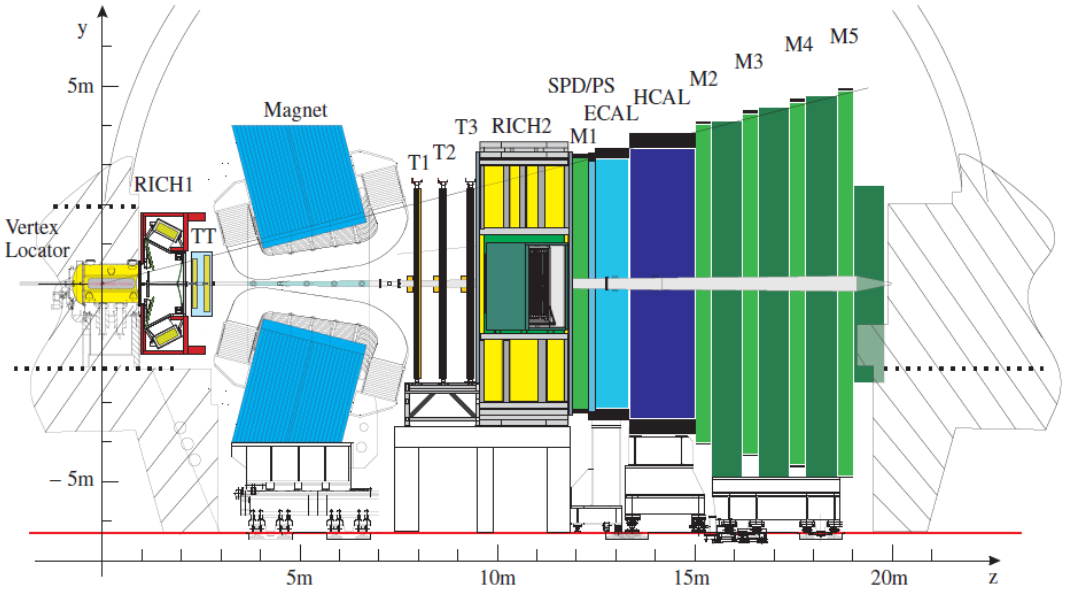

Figure 3.6: LHCb detector

3.2.1 The LHCb trigger

The LHC was designed to run at beam crossing rate of 40 MHz which corresponds to an interval of 25 ns between successive events. Some of the front-end electronics deployed in the LHCb detectors are limited to a maximum rate of 1 MHz. During Run I the optimal interval achieved between beam crossings was 50 ns, this reduces the total rate that subdetectors have to cope to. However, this is not sufficient and a trigger system was designed to select interesting events for the offline analysis rejecting background, the system is able to take a fast decision and reduce the event rate. Another stringent constraint comes from the speed of writing the data in computer disks, considering the average size of an event

in LHCb and the number of computing elements used, the trigger system has to reduce the rate to 1 kHz. To perform such a task the trigger was developed from two parts [79]: the hardware level called Level-0 (L0) and the software level, called the High Level Trigger (HLT). They have been optimized to maximize the signal to noise ratio during data taking.

The Level-0 Trigger

The L0 trigger is an hardware trigger generated by custom made electronics providing the reduction of the events rate. It reduces the LHC beam crossing rate of 40 MHz or less, down to 1 MHz. At this rate all the channels of the whole experiment can be considered and readout. The L0 trigger is performed considering outputs from three components: pile-up, calorimeter and muon system, see Fig. 3.7.

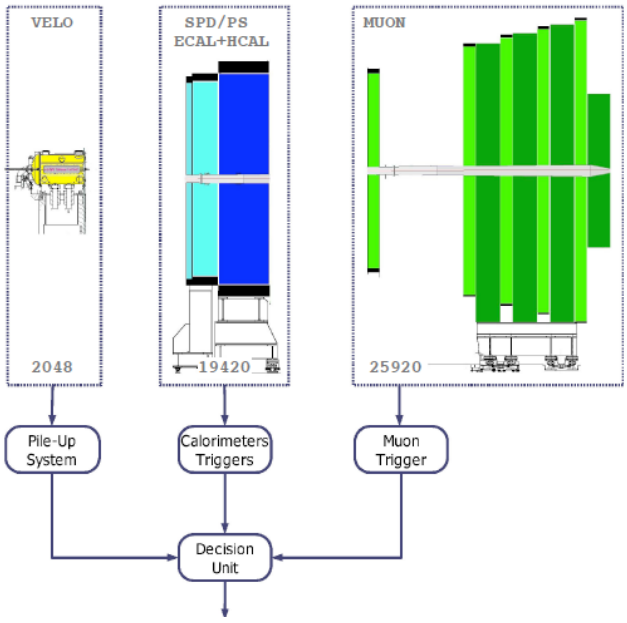

Figure 3.7: Overview of the Level-0 trigger [77]. Every 25 ns the pile-up system receives 2048 channels from the pile-up detector, the Level-0 calorimeters 19420 channels from the scintillating pad detector, preshower, electromagnetic and hadronic calorimeters while the Level-0 muon handles 25920 logical channels from the muon detector.

The pile-up system uses four silicon sensors of the same type as those used in the VELO to measure the radial position of tracks and aims at distinguishing between events with single and multiple visible interactions. The hits from these sensors are used to construct tracks which intersect the z-axis. From the distribution of the intersection points along the beam-line primary vertices candidates are provided.

The calorimeter systems checks the cluster with the highest energy deposited. It rejects the empty events or events with large cells occupancy. The muon L0-trigger selects the muons with the highest p_T as determined by the 5 muon stations. The selection criteria where chosen considering the high mass of the b hadrons and that the decay products tend to have large transverse energy (E_T) or transverse momentum (p_T).

A Level-0 Decision Unit (L0DU) collects all these values and takes the decision for each bunch-crossing. This needs a perfect synchronization with the LHC clock. The latency of the L0 trigger is 4 μs, time needed to get the data and takes the decision.

The High Level Trigger

The second step of the rate reduction is provided by a software layer, HLT, which has to reduce the rate from 1 MHz to 1 kHz or lower. The HLT algorithms are running in a computing farm, the Event Farm Filter (EFF) and use the information from all subdetectors. The HLT structure is divided in two levels, HLT1 and HLT2. HLT1 is divided into alleys, based on the main types of signatures and starts by confirming the candidates selected at L0 level, see Fig. 3.8. It reconstructs particles from vertex and tracking detectors and confirms the presence or not of neutral particles candidates, reducing the rate to 30 kHz. Cuts on p_T and impact parameter are also considered to reduce further the rate. The event is selected only if it passes at least one alley, then it is sent to the HLT2. At this level full reconstruction and pattern recognition are applied to reduce the rate to 1 kHz, applying inclusive and exclusive selection criteria. These criteria are similar to the one used in offline taking advantage of the topological properties of b-decays (secondary vertices, large impact parameters, b momentum pointing

towards the primary vertex, etc), the energetic properties (invariant mass, momentum conservation ...). Groups of selection criteria form HLT2 lines, they are different from offline selections by the fact the cuts are less stringent and some time consuming track algorithms are approximated.

Examples of L0 and HLT trigger lines will be seen in the Λ_b production study from Chapter 5.

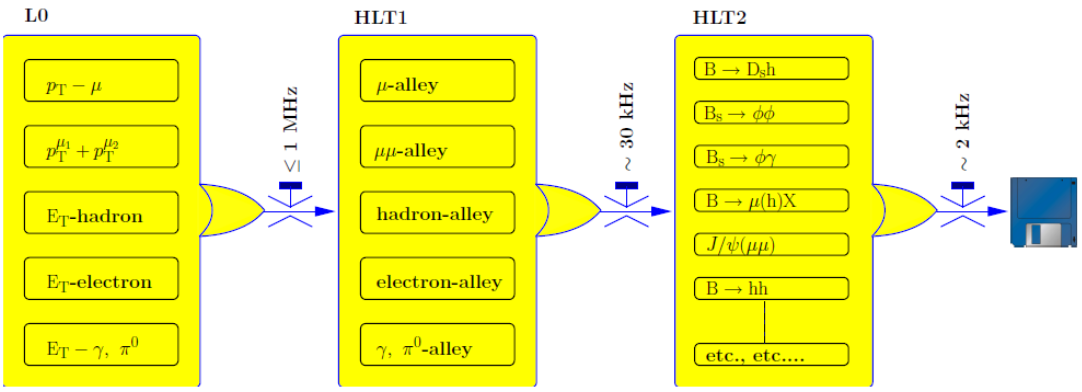

Figure 3.8: Flow-diagram of the different trigger sequences [77].

The final trigger decision is the logical OR of the inclusive and exclusive selections. HLT trigger is an application still in evolution. It follows the progress of the LHC machine in terms of instantaneous luminosity, bunch size, etc. and it is always optimized to meet the computing infrastructure power available. The configuration of the trigger algorithms at a given time is encoded in a Trigger Configuration Key (TCK) to insure reproducibility of the online trigger state at a later time.

3.2.2 Track Reconstruction and the tracking system

The geometrical view of on event is realized by the tracking system, whose task is to recombine the hits from the interactions of the particles with the material into full paths. Charged particles are reconstructed by the tracking system comprised of VErtex LOcator (VELO), the Trigger Tracker (TT), the Inner Tracker (IT) and the Outer Tracker (OT). Particle identification subdetectors can also be used

to acquire information on particles position like the muon stations for muons, or ECAL for photons. Excellent spatial resolution is required for the reconstruction of track direction and production vertices. For this reason, the vertex locator and the inner part of the tracking stations are designed with silicon technology. The outer part is equipped with straw-tubes.

The tracking system and the magnet are used to measure the momentum of the particles. For this purpose the VELO and one of the station are placed upstream and all the other stations are downstream the magnet. This configuration allows to calculate charged particle deflection due to the magnetic field.

A classification of track types according to the detectors involved to reconstructed is the following: Long, Upstream, Downstream, Velo and T tracks. In Fig. 3.9 a schematic illustration of the LHCb track types is shown.

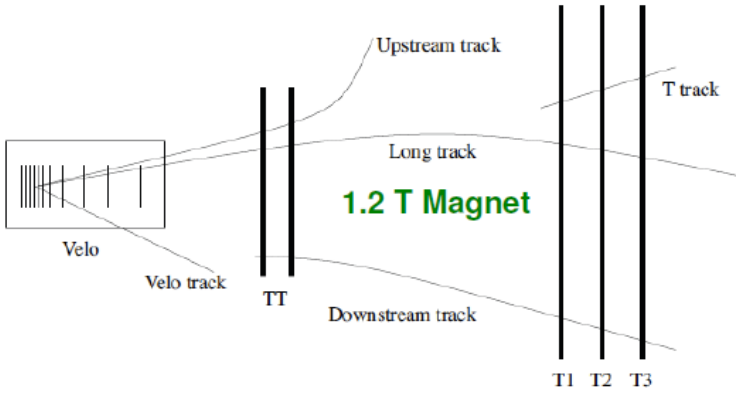

Figure 3.9: Types of tracks reconstructed by LHCb spectrometer. According to their geometrical properties and subdetectors which are used to reconstruct the tracks we distinguish the following types: Long, Upstream, Downstream, Velo and T tracks.

The algorithms for track reconstruction starts with the so called track seeds, short tracks in VELO or T stations, and then these are extrapolated in the rest of the regions, forward or backward respectively. To distinguish between class of tracks will be important in some of the following studies, so we give here some details of each track type.

- **Long tracks:** they traverse all the tracking system from the VELO up

to the tracking stations. They have the most precise momentum reconstruction and most of the LHCb measurements use these type of tracks. The reconstruction starts considering VELO seeds extrapolating trajectories combining the tracking station information. This method reconstructs the 90% of these tracks, another 5% is obtained considering T seeds and requiring a match, in the VELO region, with the VELO seeds. The efficiency is directly proportional to the particle momentum and it decreases for low momentum values, due to the multiple scattering in the material.

- **Downstream tracks:** they traverse the TT and T stations are mainly due to K_S^0 e Λ decays which decay outside the VELO acceptance.
- **Upstream tracks**: they have hits only in VELO and TT stations. They present low momenta and are bent out the detector acceptance by the magnetic field. Upstream tracks are useful for tagging purpose, and since they go through the RICH1 detector.
- **VELO tracks:** they have hits only in the VELO detector. They are used for the Primary Vertex (PV) reconstruction.
- **T tracks:** they are produced in secondary interactions, they have hits only in the T stations and they are mainly used for the RICH2 pattern recognition

The tracking performances are functions of event parameters, in Fig. 3.10 there are two examples of momentum and impact parameter resolution obtained with reconstructed tracks from 2011 data, for more details see also the reference [80].

In the following section tracking subdetectors are presented.

3.2.2.1 The vertex locator

The vertex locator (VELO) [81] covers a region of 1 m around the interaction point and consists of 84 silicon sensors distributed along the z axis as illustrated in the Figure 3.11. The silicon sensors are grouped in 21 stations each made of four half-circular silicon sensors. To obtain the 3D coordinates each station is made of pair of sensors: the r sensor provides the radial distance from the beam

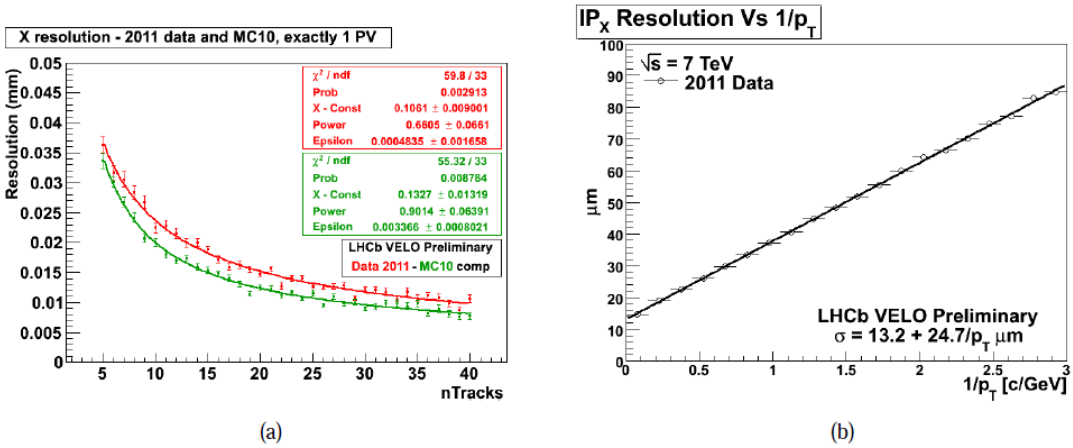

Figure 3.10: Left: Primary vertex resolution in the transverse plane as function of the number of tracks. Right: Impact parameter resolution in the transverse plane as function of $1/p_t$. [80]

axis, the ϕ sensor provides the azimuthal angle coordinate around the beam. The z coordinate is provided by the position of each sensor plane. During injection the two detector halves are retracted 3 cm away to avoid radiation damages due to unstable beams. In the running mode the closest approach to the nominal beam axis is 5 mm.

The VELO stations are located in the LHC vacuum. There are some possible sources of interference as the radio frequency picks up from the LHC beams, gas losses and the field generated by the bunch structure of the beams. To avoid these problems all the modules are separated by RF-foils.

The VELO is designed to give a proper time resolution of better than 50 fs, necessary for resolving the oscillation rate B_s^0. It is also used to take decision at the L0 trigger level to accept or reject the event forcing its efficiency to be at least 99%. The readout chip was designed with a peak time and a sampling frequency respectively equal to the LHC crossing frequency of 40 MHz. The two upstream stations are hardware identically to the others and are used for the pile-up veto. They are used to improve the performance and to identify multi-interaction events. The construction limitations due to the closeness to the beam and the acceptance of downstream detectors allow a coverage with the highest

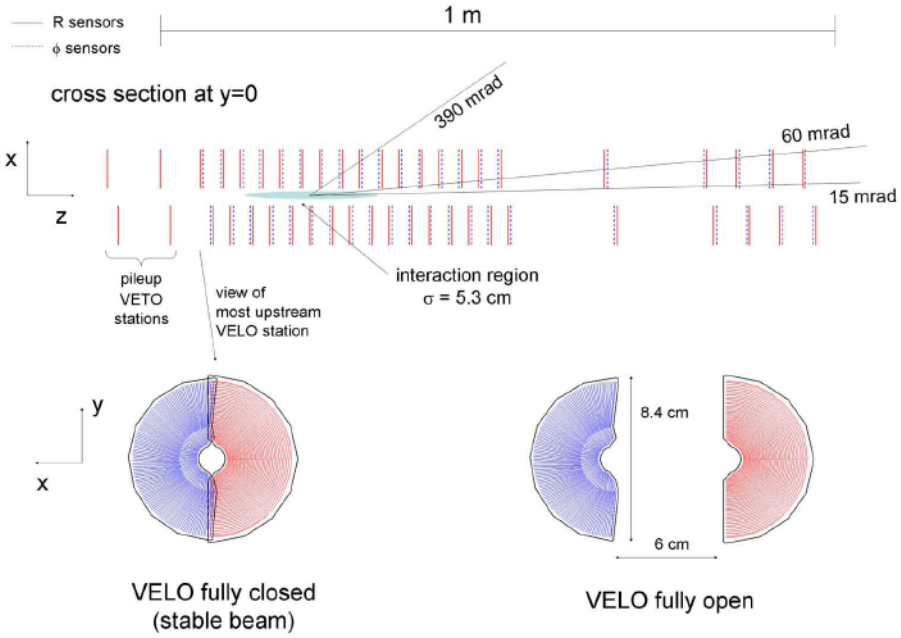

Figure 3.11: Cross section in the (x, z) plane of the VELO silicon sensors, at $y = 0$, with the detector in the fully closed position. The front face of the first modules is also illustrated in both the closed and open positions. The two pile-up veto stations are located upstream of the VELO sensors.

precision in the pseudorapidity region of $1.6 < \eta < 4.9$.

3.2.2.2 The magnet

A dipole magnet [82] is used to measure the momentum of the charged particles from the curvature of their trajectories. To keep its dimension small is placed close to the interaction region immediately downstream of RICH1 and immediately upstream of the first tracking stations. This positioning is designed to give low track curvature in the VELO, such that the fast straight-track fitting algorithms can be used at the trigger level, while providing sufficient field integral before the tracking stations to give good momentum resolution from tracking.

The LHCb magnet is a warm resistive dipole designed with saddle-shaped coils placed mirror-symmetrically to each other in the magnet yoke, as shown in Fig. 3.12. The magnet is designed to generate a field in only one direction

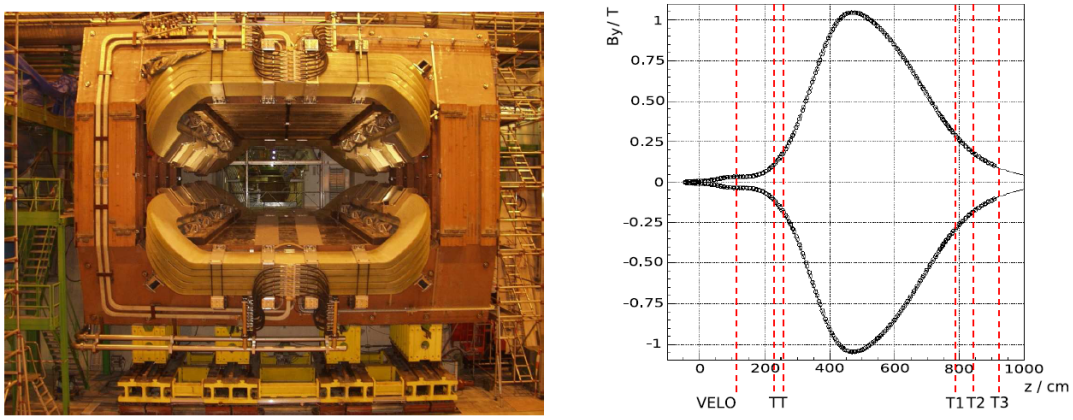

Figure 3.12: Magnetic field.

(vertical direction), but with two polarities, positive and negative. The reversed field is used to study possible asymmetries in the detector, and systematics to be included in all the high-precision measurement. The magnet features a bending power of $\int Bdl = 4\ Tm$ (integrated over 10 m, 1.1 T maximal magnetic field intensity) and dissipates about 4 MW.

3.2.2.3 The trackers

The main components used for track reconstruction are the tracking stations, one placed after RICH1 and upstream the magnet and three other are downstream the magnet. As mention earlier two technologies were used for the trackers considering particle densities. Where the number of charged particles is high, silicon detectors were chosen. This is the case for Tracker Turicensis (TT), first station, which covers all the LHCb acceptance, and Inner Tracker (IT) the inner part of the next three stations. Drift-time tube were used to cover the remaining part of the acceptance, without loosing performance, these parts are called Outer Tracker (OT).

The silicon trackers

The design of the silicon detectors optimizes for the spatial resolution, single-hit efficiency for the specified running conditions. The optimization takes into considerations the following main parameters: hit occupancy, signal shaping time,

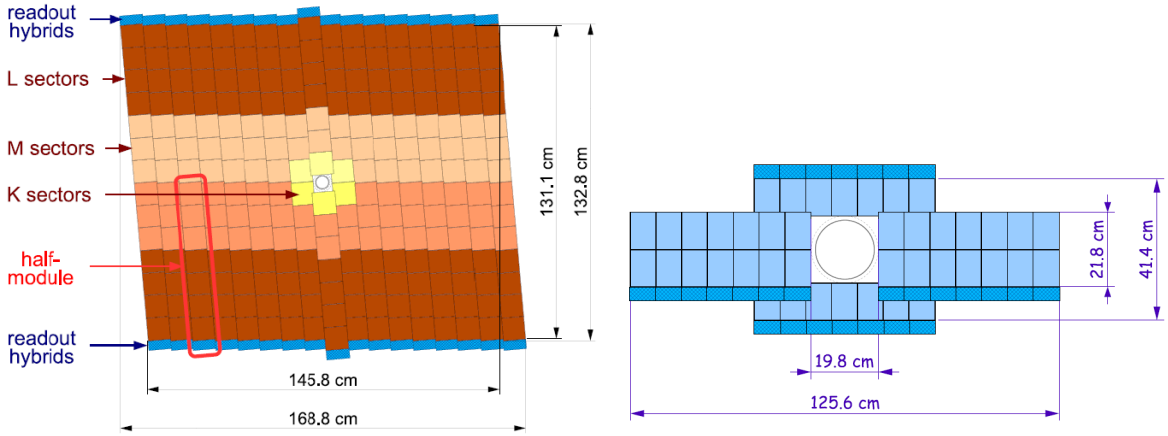

Figure 3.13: Left side: Layout of the v-layer in the silicon tracker station TT. Different readout sectors are indicated by different shadings. Right side: layout of the inner tracker sensors in one x-layer. The sensors are located in four boxes around the beampipe in the middle.

radiation damage, material budget and readout channel number [83; 84]. At LHCb they operate at below $5°C$ to slow the damaging effects of radiation. To enable the reconstruction of three dimensional points the micro-strip sensors are arranged such that each station has four layers $(xuvx)$ with vertical strips in the first and the last layer, and strips rotated by a stereo angle of $-5°$ and $+5°$ in the second and the third layers. These displacement together with a strip pitch of $\approx 200\mu m$ allows a nominal resolution of $50\mu m$.

Tracker Turicensis subdetector is located between the first Cherenkov detector (RICH1) and the magnet. It has an active surface of $8.4m^2$ and it covers the full acceptance. The p^+-on-n silicon sensors are grouped into ladders which are placed around the beampipe as shown in Fig. 3.13, left side. To improve the momentum resolution the (x, u) and (v, x) layers are separated by a distance of 30 cm. The TT gives to the trigger a rough estimation of the particles transverse momentum. It is also fundamental in reconstructing the trajectories of the long lived neutral particles that decay outside of the VELO fiducial volume and in reconstructing the tracks of the low momentum particles.

Inner Tracker subdetectors are the innermost regions of the T stations (T1, T2, T3) which are placed downstream the magnet and before the second

Cherenkov detector (RICH2). Even though it represents the 1.3% of the tracking stations sensitive area, the IT is traversed by the 25% of the particles which reach the tracking stations. Each layer surrounds the beam-pipe with its four sectors arranged in a cross shape configuration, overlapping in x, to avoid acceptance gaps and to facilitate the relative alignment, see 3.13. The sectors have different thickness chosen to maximize the signal to noise ratio and to reduce the material budget. A special characteristics is that the front end read out electronic is in the LHCb acceptance, so an extreme care was put to make it as radiation resistant and transparent as possible.

The outer tracker

The external part of the T1-T3 tracking stations is based on gas detectors. The Outer Tracker (OT) [85] is a drift-time detector equipped with straw-tubes. Similar to the strip detectors each station have four layers ($xuvx$) of double-layered straw-tubes. A double-layer is built up of overlapping staggered straws as is depicted in Fig. 3.14 to avoid insensitive areas in the detector.

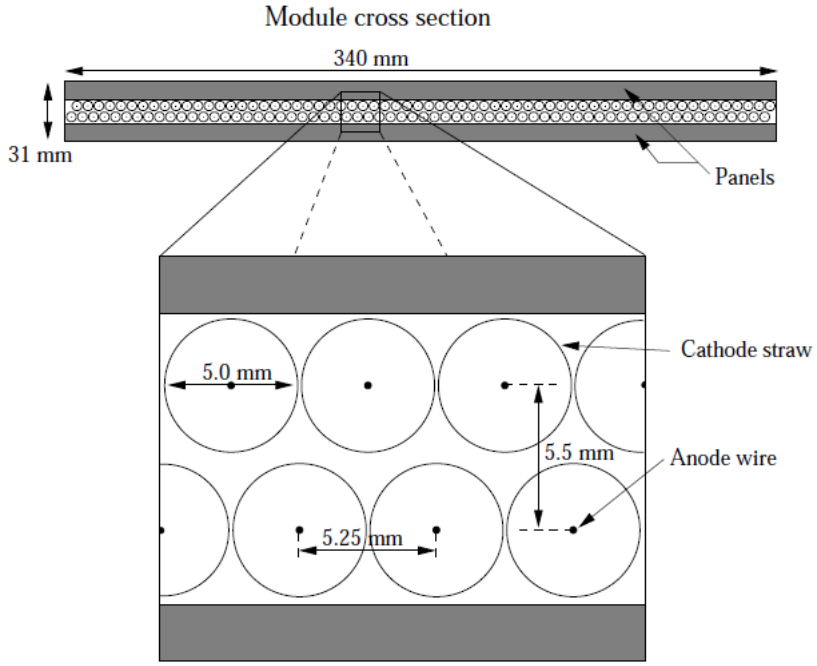

Figure 3.14: Cross section of an OT module (128 straws). A small region containing a few straws is magnified.

A drift tube of the outer tracker is assembled with a high carbon loaded polyimide film (Kapton XC) wrapped with aluminum as the shell of the straw tube. The aluminum acts as a shielding between neighboring channels. The central wire is a gold plated tungsten anode with a diameter of $25\mu m$. The tubes itself have an inner diameter of 5.0 mm and are placed with a pitch of 5.25 mm in the modules. The active volume is filled with a gas mixture of Argon (70%) and CO_2 (28.5%) and O_2 (1.5%) to guarantee fast drift time of 50 ns and good space resolution.

3.2.3 Particle Identification

Particle identification (PID) is one of the most important aspects needed for the study of the rare decays. Different subdetectors participate in the identification of the final states particles: e, μ, π, K and p the charged ones and γ and π^0 the neutral ones. The involved subdetectors are RICH1 and RICH2 for hadron separation mainly, the muon stations M1-M5 for muon identification and the calorimeter system (scintillator pad detector, preshower detector, electromagnetic calorimeter and hadron calorimeter) for hadrons, electrons and neutral particles. In order to determine the particle species, for each track specific information from every subsystem - like Cherenkov angle, energy deposited, number of hits - are translated into a likelihood function, , which is then minimized. The procedure is repeated considering different particle hypotheses and the output is a function which considers the probability for the track to belong to a certain species. For example, in RICH detectors the following delta log-likelihood function is computed as to weigh the distinction of a K from a π

$$\Delta \log \mathcal{L}_{K\pi} = \log \mathcal{L}(K) - \log \mathcal{L}(\pi) = \log \frac{\mathcal{L}(K)}{\mathcal{L}(\pi)}$$

The final likelihoods are combined from the various detectors:

$$\begin{aligned}
\mathcal{L}(e) &= \mathcal{L}^{RICH}(e)\mathcal{L}^{CALO}(e)\mathcal{L}^{MUON}(non-\mu) \\
\mathcal{L}(\mu) &= \mathcal{L}^{RICH}(\mu)\mathcal{L}^{CALO}(non-e)\mathcal{L}^{MUON}(\mu) \\
\mathcal{L}(h) &= \mathcal{L}^{RICH}(h)\mathcal{L}^{CALO}(non-e)\mathcal{L}^{MUON}(non-\mu)
\end{aligned}$$

where h is an hadron.

The subdetectors involved in the particle identification will be described in the following sub-sections.

3.2.3.1 RICH subdetectors System

The identification of hadrons is mainly provided by two stations of Ring Imaging CHerenkov (RICH) counters. Cherenkov radiation is emitted in a cone when a charged particle passes through a radiator material with a velocity that is greater than the speed of light in that medium. The polar angle, at which this light is emitted, is reconstructed by photon detectors and depends on the refractive index of the radiator and the velocity of the particle. Combining the angle measurment with momentum information from the tracking system, one can calculate the mass of the particle.

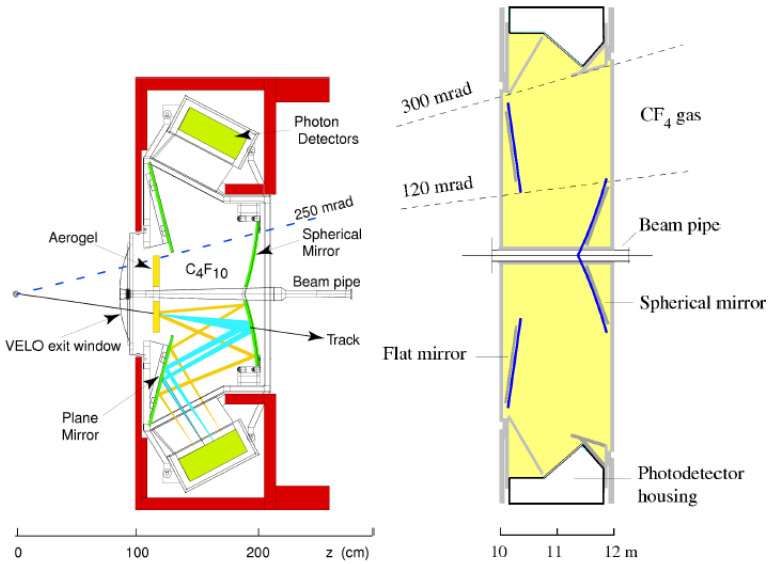

Figure 3.15: Left: side view schematic of the RICH 1 detector. Right: top view schematic layout of the RICH 2 detector.

The need for particle identification to cover a wide momentum range (2-100 GeV/c) imposed a design solution with two stations as shown in Fig.3.15. RICH1 covers the low and intermediate momentum region 2-40 GeV/c over the full spec-

trometer angular acceptance of 25300 mrad. The acceptance is limited at low angle by the size of the beampipe upstream of the magnet. RICH2 covers the high-momentum region 15100 GeV/c, over the angular range 15120 mrad.

As radiators fluorocarbon gases at room temperature and pressure are used, C_4F_{10} in RICH1 and CF_4 in RICH2. The momentum threshold for kaons to produce Cherenkov light in C_4F_{10} at chosen working point is 9.3 GeV/c. Particles below this momentum would only be identified as kaons rather than pions in veto mode, i.e. by the lack of Cherenkov light associated to the particle. To maintain positive identification at low momentum and in order to separate kaons from protons, a second radiator is included in RICH1: a 50 mm thick wall made of silica aerogel at the entrance to RICH1. The acceptance of each RICH station is ilustrated in Fig. 3.16, in the same figure, the right plot, one can see the separation power for every radiator.

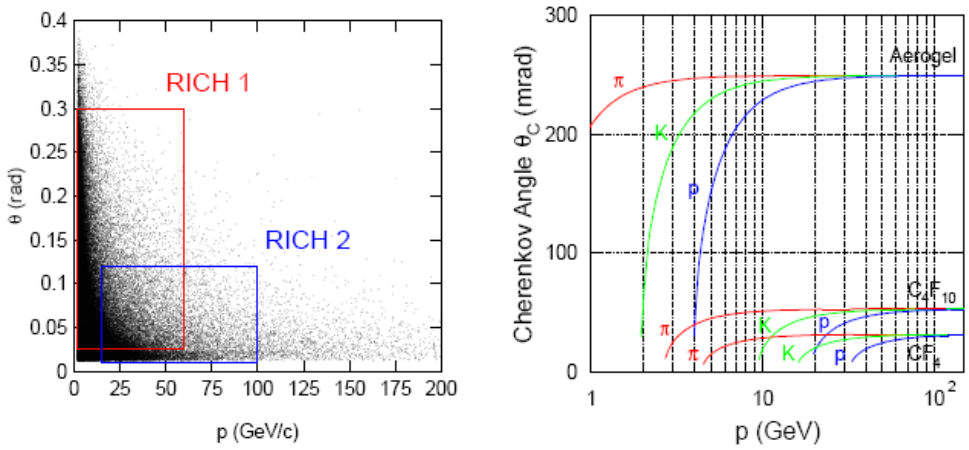

Figure 3.16: Separation power

Both RICH detectors have a similar optical system, with a tilted spherical focusing primary mirror, and a secondary flat mirror to limit the length of the detectors along the beam direction. Each optical system is divided into two halves on either side of the beam pipe, with RICH1 being divided vertically and RICH2 horizontally. The vertical division of RICH1 was necessitated by the requirements of magnetic shielding for the photon detectors, due to their close proximity to the magnet. The spherical mirrors of RICH1 (4 segments) are constructed in four

quadrants, with carbon-fibre structure, while those of RICH2 (56 segments), and all flat mirrors (16 and 40 segments in RICH1 and RICH2 respectively), are tiled from smaller mirror elements, employing a thin glass substrate. A reflectivity of about 90% was achieved for the mirrors, averaged over the wavelength region of interest, 200-600 nm. The total material budget for RICH1 is only about 8% X_0 within the experimental acceptance, whilst that of RICH2 is about 15% X_0.

The Cherenkov photons emitted by charged particles passing through the RICH radiators are focused into ring images on the photon detector planes, situated outside of the spectrometer acceptance. A novel hybrid photon detector (HPD) was developed in collaboration with industry specifically for application in the LHCb RICH system. The HPDs employ vacuum tubes with a 75 mm active diameter, with a quartz window and multialkali photocathode. The photoelectrons are focused onto a silicon pixel array, using an accelerating voltage of -16 kV. The pixel array is arranged in 32 columns and 32 rows, giving a total of 1024 pixels per tube. The pixel size is $2.5 \times 2.5\ mm^2$ at the level of the photocathode. A total of 484 HPDs are closepacked to cover the four photodetector planes. Two planes are employed in each RICH, with 196 tubes used in RICH1 and 288 in RICH2. The photodetector planes are separated from the radiator gas volumes by quartz windows, and the photodetector volumes are maintained in an atmosphere of CO_2.

3.2.3.2 The calorimetry System

The calorimetry system was designed to be able to identify photons, electrons and hadrons, detecting the transverse energy (ET) released, and their spatial coordinate. It is also part of the LHCb trigger where a readout electronics must be very fast and reliable. In the L0 trigger the energy deposited by the electrons are of the variables used to take the d ecision. Sampling calorimeters, of the type used at LHCb, consist of alternating layers of absorber and detector material. The absorber layer is made from a material chosen to develop the electromagnetic or hadronic shower. The detector layer is made from a scintillating material. The energy of a particle is inferred from the sum of scintillating light produced by the shower. An accurate energy measurement therefore requires that the shower is

completely contained within the calorimeter.

The calorimeter system is located downstream of RICH2, between the first and the second Muon stations. Going from up to downstream, the system consists of four components.

The first station of the calorimetry system is the **Scintillator Pad Detector** (SPD) [86] and consists of a single 15 mm-thick plane of scintillator tiles. It is used to distinguish between signals in the calorimeter associated to charged particles and those which are associated to neutral particles.

The **Pre-Shower** (PS) [86] is made up of a 12 mm-thick lead wall located after the SPD, corresponding to 2.5 X_0, followed by a single 15 mm-thick scintillator plane[1]. The PS is designed to separate electrons from the large charged pion background by exploiting the fact that an electron will shower in the lead wall, whereas only a small fraction of charged pions will interact.

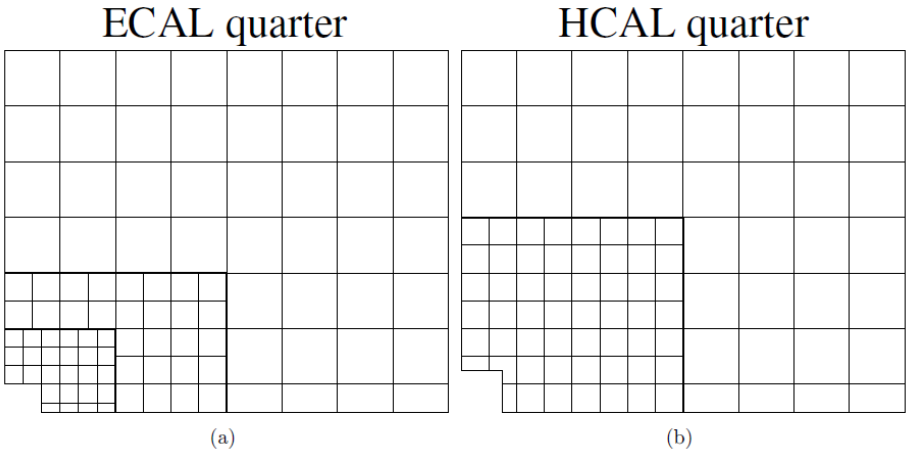

Figure 3.17: Left: lateral segmentation of the SPD, the PS and the ECAL. Right: lateral segmentation of the HCAL. In both figures, one quarter of the detector front face is shown.

The electromagnetic calorimeter ECAL [87] is the subdetector for photons and electrons identification. It is 12.5 m far away from the interaction point and it covers the acceptance of LHCb, but has a limitation at small polar angles.

[1]The radiation length, X_0, of a material is defined as the distance over which the electron energy is reduced by $1/e$ due to Bremsstrahlung radiation only.

It's composed of 66 alternating layers of 2 mm thick lead sheets and 4 mm thick scintillator plates, with a total radiation thickness of 25 X_0. The calorimeter is subdivided into inner, middle and outer sections which differ each other by the density of cells: higher in the inner section, lower in the outer one (see Fig. 3.17). The density of cells was chosen in such a way that the granularity is high enough to separate two individual showers. Each scintillator plate is read out with a plastic WLS fiber, and the fibers corresponding to an individual ECAL module are grouped together in bunches and read by a single PhotoMultiplier Tube (PMT). The ECAL energy resolution is:

$$\frac{\sigma_E}{E}_{ECAL} = \frac{8.5\% < a < 9.5\%}{\sqrt{E}} \oplus 0.8\%$$

where the first term a stands for photoelectron statistics, called stochastic term and the second term represents the electronics noise, E is in GeV.

The **Hadronic CALorimeter** (HCAL) [63] detects hadrons of high energies. It is a sampling calorimeter obtained combining an iron absorber layer, with a thickness of 16 mm, with an active layer equipped with scintillating material of 4 mm thickness. The overall depth of 5.6 λ_I, where λ_I is the nuclear interaction length[1], is a compromise between detector performance, space requirements along the beam axis and financial cost. The resolution from technical design report is [87]:

$$\frac{\sigma_E}{E}_{HCAL} = \frac{(80)\%}{\sqrt{E}} \oplus (10)\%$$

3.2.3.3 The muon system

Some of the most important channels studied by LHCb, like the flavor changing neutral current decay $B_s \to \mu + \mu$ or the golden channels $B_d^0 \to J/\Psi(\mu + \mu)K_s^0$ and $B_s^0 \to J/\Psi(\mu + \mu)\phi$ have muons in their final states. Muon particles interact weakly with the material such that they can be placed at the end of the spectrometer. For these reasons muon system is a fundamental subsystem. It is also part of the LHCb trigger system providing a fast response for the highest p_T muons

[1]The nuclear interaction length is defined as the average distance a hadron has to travel before an inelastic nuclear interaction occurs.

in the event for the L0 trigger and a muon identification for the HLT level.

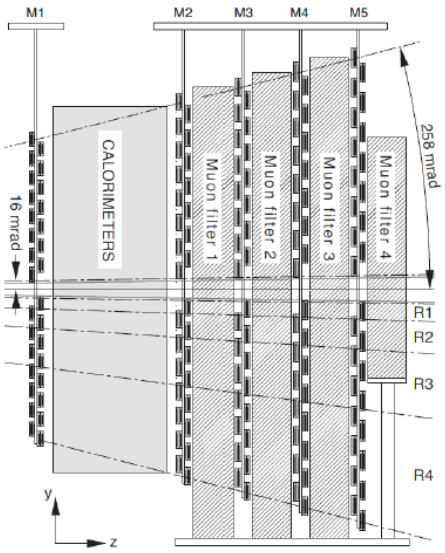

Figure 3.18: Muon stations.

It consists of five rectangular stations (M1-M5), M1 placed upstream and M2-M5 downstream the calorimeters, see Fig. 3.18. The muon system is part of the trigger and the stations M1-M3 have an high granularity in the bending plane (x coordinate), while the last two stations M4 and M5, used for the identification of the most penetrating particles, have a lower spatial resolution. The stations are made up by absorber iron planes and active planes to obtain a total radiation length of about 20 X_0. To identify the particle as a muon candidate, at least two stations must have hits in the direction of the hypothetical track. All the downstream stations and the outer regions of the M1 station are equipped with Multi-Wire Proportional Chambers (MWPC). The M1 inner region uses triple-GEM (Gas Electron Multiplier) to limit aging problem due to the high particle flux. The gas mixtures were chosen to optimize the resolution and the velocity of the signal, for the MWPC the mixture is Ar (40%), CO_2 (55%) and CF_4 (5%). The same mixture, but with different percent age Ar (45%), CO_2 (15%) and CF_4 (40%) is used in the case of the GEM chambers.

Only tracks with momentum greater than 3 GeV/c reach the muon stations,

and only particles with momentum greater than 6 GeV/c pass trough all the five stations. The muon system performances in LHCb 2011 data taking are illustrated in Figure 3.19.

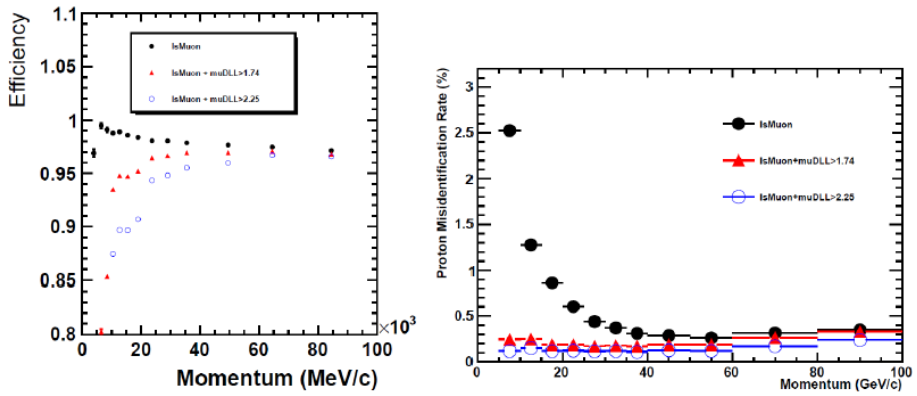

Figure 3.19: Idendtification and misidentification efficiencies for the muon detector.

3.3 The LHCb computing

3.3.1 The online and data acquisition systems

All the data coming from the detector and all the working condition parameters of the machine and of the experimental area must be transferred and synchronized to a permanent storage. All these tasks are made by the online system [7577]. To fulfill these requests the online system is divided into three parts:

- **Data AcQuisition system (DAQ):** it transfers all the events, selected by the trigger, from the frontend electronics to the permanent storage.
- **Timing and Fast Control (TFC):** it checks the clock of whole the system. It is the distributor of the beamsynchronous clock during the data transfer.
- **Experiment Control System (ECS):** it controls the status of LHCb: detectors, working conditions (gas, temperature, voltages), LHC machine

conditions, trigger, DAQ and TFC. All the controls made are registered to be simply checked by the user when employing PVSS II software

The data obtained from the detector are analyzed by the users. Data are reconstructed and written on tape using the distributed computing technologies (GRID) [88].

3.3.2 The LHCb software

Data processing in LHCb is an industrial enterprise which have involved large parts of the collaboration during the last decade and it is undergoing continuous improvement. The main objectives it aims to achieve are: fast routines to cope with large real time fluxes of data, efficient storage and network management, user friendly interfaces for a wide range of tasks. From the computing point of view the resources are distributed around different participating laboratories in a network called GRID. The nodes of this network are grouped hierarchical into Tiers; CERN is the main node, also called Tier 0.

The raw data are produced by the Event Filter Farm using the electric signals recorded by the detector. The data are stored in files labeled by the running periods and passed to the **Brunel** [89] package for reconstruction. The Brunel package reconstructs the tracks from the hits registered by the detectors. It also reconstructs the momentum of the particles, the energy, the primary and secondary vertices. At this level the information from PID detectors are also read and the PID estimators are computed. These data are saved offline.

The next step is the *Stripping* step. To avoid the congestion of the network the data from the previous step are not available to the end user yet. In the stripping step the data are filter by a list of conditions called stripping lines. The stripping lines are conditions similar to the ones used in an offline analysis and act like a common denominator for the interests of different users. The data passing these stripping lines, also called preselection lines, are marked with the type of line they passed and then are saved and made available to the user. The *Stripping* step is performed by the **DaVinci** [90] package. The DaVinci package is one layer of abstraction further, it starts from the objects generated by Brunel and constructs candidates, decays chains, implements vertexing and fitting algorithms etc. Also

this package is employed by the end user to extract the candidates, the event and detector information needed for his analysis. Typically, these information are saved in ntuples (array of events) in *root* files. This type of file is the native type of file for the C++ ROOT [91] software framework, an external framework used by the entire community of particle physics. ROOT also has libraries which bind the C++ objects to Python objects such that one can also perform the offline analysis in Python [92] language.

The same suit of packages are also used for the analysis of the Monte Carlo simulated data. In addition, the following packages, Gauss [93], EvtGen[94], GEANT [95], Boole [96] and Moore [97], are used to bring the simulation data in the format which can be accepted by Brunel.

The Gauss simulation software is used to simulate the *pp* collision, generate particles and describe the behaviors of particles in the detector. Its particle generator is based on Pythia 6.4 generator with parameters configured for LHCb. The EvtGen package is used in Gauss to describe the decays of the particles generated by Pythia. The Geant4 package is introduced to trace the decay products through the detector while Boole is the digitization simulation package, which applies the detector response to hits previously generated in the sensitive detectors by the Geant4 based simulation. The output of Boole consistes in a digitized electronic signal similar to the real data from the detector.

The analyses presented in this thesis are performed with the BPython package which was written by the author during the stage of this thesis. The BPython package is presented in the Annex A.2.

Chapter 4

Particle identification studies with RICH detectors

In this chapter the first section is dedicated to a more detailed description of the physics behind RICH detectors in order to better highlight the author's own contribution to the study of PID performances of RICH, which is presented in next two sections. The first study develops a method for selecting high purity samples of protons and pions from data. In the second study, these calibration samples are used to evaluate the systematic uncertainties due to RICH performance in a physics analysis, Λ_b cross section measurement, described in details in Chapter 5.

4.1 Physics of RICH detectors

4.1.1 Motivation for hadron identification

The primary role of the RICH system is the identification of charged hadrons (π, K, p). It can also help in the identification of charged leptons (e, μ) using information from the other dedicated detectors, the calorimeter and muon systems respectively [98; 99]; the impact of the RICH in this case is to improve the separation of signal from background.

One of the major requirements for charged hadron identification in a flavour-physics experiment is the reduction of combinatorial background. Many of the interesting decay modes of b and $c-$flavoured hadrons involve hadronic multibody

final states. At hadron colliders like the LHC, the most abundant produced charged particle is the pion. The heavy flavour decays of interest typically contain a number of kaons, pions and protons. It is therefore important in reconstructing the invariant mass of the decaying particle to be able to select the charged hadrons of interest in order to reduce the combinatorial background.

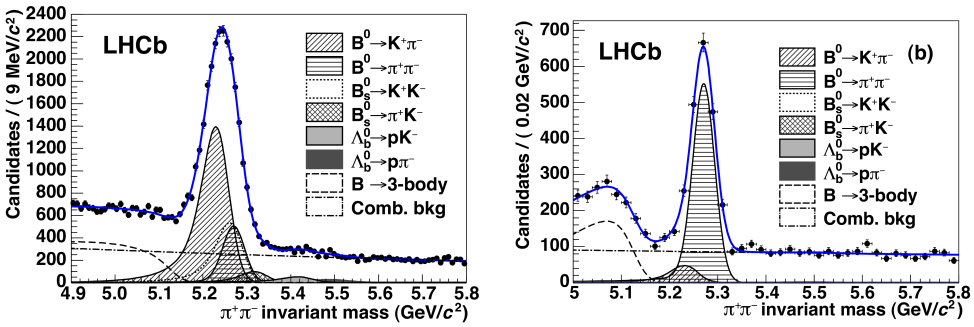

Figure 4.1: Rich separation of topological similar events [100].

The second major use of the particle identification information is to distinguish final states of otherwise identical topology. An example is the two-body hadronic decays, $B \to h^+h^-$, where h indicates a charged hadron. In this case there are many contributions, as illustrated in Fig. 4.1, including $B^0 \to \pi^+\pi$, $B_s^0 \to K^+K$, and other decay modes of the B^0, B_s^0 and Λ_b. A signal extracted using only kinematic and vertex-related cuts is a sum over all of the decay modes of this type (Fig. 4.1 left), each of which will generally have a different CP asymmetry. For a precise study of CP-violating effects, it is crucial to separate the various components. This is achieved by exploiting the high efficiency of the RICH particle identification (Fig. 4.1 right).

Another application of the charged hadron identification is for an efficient flavour tagging [101]. When studying CP asymmetries or particle-antiparticle oscillations, knowledge of the production state of the heavy-flavoured particles is required. This can be achieved by tagging the particle/antiparticle state of the accompanying hadron. Heavy-flavoured particles are predominantly produced in pairs. One of the most powerful means of tagging the production state is by identifying charged kaons produced in the $b \to c \to s$ cascade decay of the

associated particle. Such tagged kaons (as well as kaons from the b fragmentation when a B_s^0 is created) have a soft momentum distribution, with a mean of about 10 GeV/c. Particle identification down to a few GeV/c can therefore significantly increase the tagging power of the experiment.

The typical momentum of the decay products in two-body b decays is about 50 GeV/c. The requirement of maintaining a high efficiency for the reconstruction of these decays leads to the need for particle identification up to at least 100 GeV/c. The lower momentum limit of about 2 GeV/c follows from the need to identify decay products from high multiplicity B decays and also from the fact that particles below this momentum will not pass through the dipole magnetic field (4 Tm) of the LHCb spectrometer.

A further example of the requirements for particle identification in LHCb is its use in the trigger. LHCb has a high performance trigger system [79], that reduces the event rate from the 40 MHz bunch crossing frequency down to about 2 kHz that can be written to storage. The RICH reconstruction is fast enough to contribute to the high level trigger. An example is the online selection of the ϕ particle, which is present in many of the decay modes of interest.

4.1.2 Cherenkov radiation

The electric field of a charged particle traversing a dielectric medium of refractive index n will cause the electrons of the atoms of the medium to be displaced and the atoms to become polarised. Photons are emitted as the electrons of the dielectric return to equilibrium. If the velocity of the particle v is less than the speed of light in the dielectric c/n, the arrangement of the induced dipoles is symmetric and the emitted photons destructively interfere and no radiation is detected. However, if the particle velocity is superluminal, i.e. $v > c/n$, the induced dipoles are not symmetric and consequently the photons constructively interfere and photons are emitted, a phenomenon which is known as Cherenkov radiation [102].

The Huygens construction of the emitted Cherenkov radiation is illustrated in Figure 4.2, from which it follows that the angle θ_c at which light is emitted

relative to the particles trajectory is

$$\cos(\theta_c) = \frac{1}{n\beta} = \frac{1}{n}\sqrt{1 + (\frac{m}{p})^2} \tag{4.1}$$

where β is the particles velocity, expressed as fraction of c, m is the particle mass and p the particle momentum. The angle θ_c is often referred to as the Cherenkov angle. From equation 4.1 it follows that the mass of a particle, and thus its identity, can be derived from a measurement of the Cherenkov angle and the particles momentum.

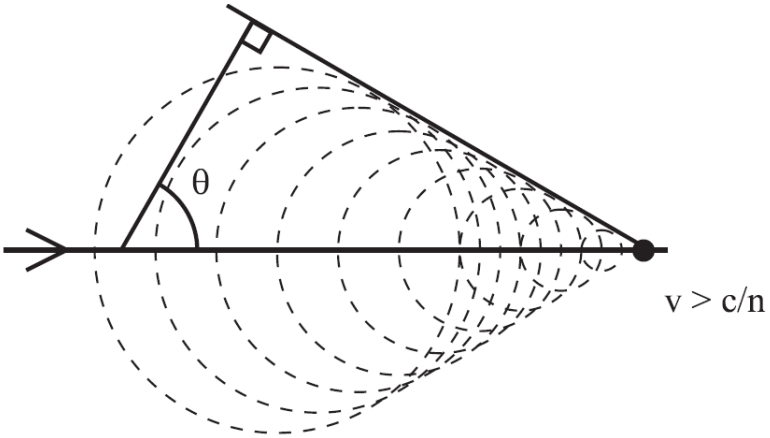

Figure 4.2: Huygens construction for Cherenkov radiation of a superluminal charged particle, which results in a coherent front at an angle θ_c relative to the particles trajectory.

The intensity and spectrum of photons produced by the Cherenkov effect is governed by the Frank-Tamm relation [86],

$$\frac{dN}{dE} = \frac{\alpha}{\hbar c} Z^2 L \sin^2 \theta_c, \tag{4.2}$$

where dN is the number of photons generated with energy between between E and $E + dE$, α is the fine structure constant, Z the particle charge and L the distance traversed through the radiator. For a particle with $Z = 1$ and velocity

$\beta \approx 1$, it follows that

$$\frac{dN}{dE} = (370 cm^{-1} eV^{-1}) L \sin\theta_c, \tag{4.3}$$

For a particle with energy above 1 GeV only a negligible fraction of its energy is radiated as photons [85]. The Cherenkov mechanism is therefore a non-destructive process and as such an ideal tool for particle measurement. The weak light yield does, however, impose stringent requirements on the photon detector sensitivity.

4.1.3 Performance

Determining the performance of the RICH Particle IDentification (PID), both during and after data taking, is particularly important for analyses that exploit RICH PID, for which knowledge of efficiency and misidentification rates are required. Moreover, it enables comparison with expectations and provides a benchmark against which to compare the effectiveness of alignment and calibration procedures. This section provides a description of the PID algorithms and the performance obtained following analysis of data from the first LHC runs.

In order to determine the particle species for each track, the Cherenkov angle information must be combined with the track momentum measured by the tracking system.

The RICH detectors operate in a high occupancy environment, as hinted by Fig. 4.3. To reconstruct such events efficiently, an overall event log-likelihood algorithm is employed, where all tracks in the event and in both RICH detectors are considered simultaneously. This allows for an optimal treatment of tracks where Cherenkov cones overlap.

Since the most abundant particles in pp collisions are pions, the likelihood minimization procedure starts by assuming all particles are pions. The overall event likelihood, computed from the distribution of photon hits, the associated tracks and their errors, is then calculated for this set of hypotheses. Then, for each track in turn, the likelihood is recomputed changing the mass hypothesis to e, μ, π, K and proton, whilst leaving all other hypotheses unchanged. The change in mass hypothesis amongst all tracks that gives the largest increase in the event likelihood is identified, and the mass hypothesis for that track is set to

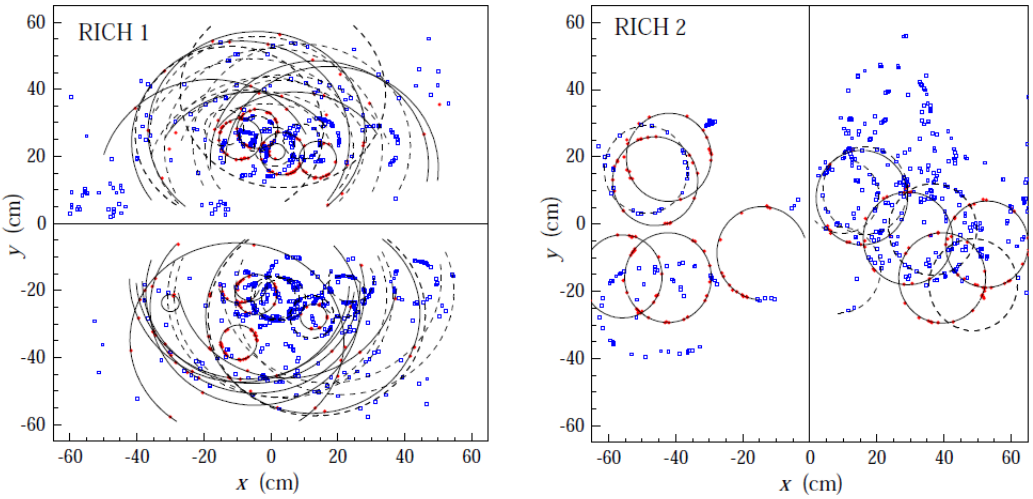

Figure 4.3: Photon detector hits and reconstructed Cherenkov rings (black lines) from a typical event in the detection planes of RICH 1 (left) and RICH 2 (right). The Cherenkov hits associated to a track by the pattern recognition algorithms are indicated by red dots. The blue dots are caused by backgrounds such as secondary particles, electronic and detector noise, or are associated with tracks not reconstructed by the tracking algorithms. The smaller radii rings in RICH1 are due to the C4F10 radiator, whilst the larger rings originate from the aerogel [84].

its preferred value. This procedure is then repeated until all tracks have been set to their optimal hypotheses, and no further improvement in the event likelihood is found.

The overall identification capabilities of RICH are illustrated in Fig. 4.4.

4.2 MC free calibration of LHCb RICH detectors using the $\Lambda \to p\pi$ decay

The LHCb physics program is focused on high precision studies of CP violation and rare phenomena in b hadron decays. The RICH detectors of LHCb will provide hadron identification over the wide momentum range from 1 to 100 GeV/c, and are central to the physics goals of the experiment. An excellent understanding of the hadron identification performance of the RICH detectors is essential.

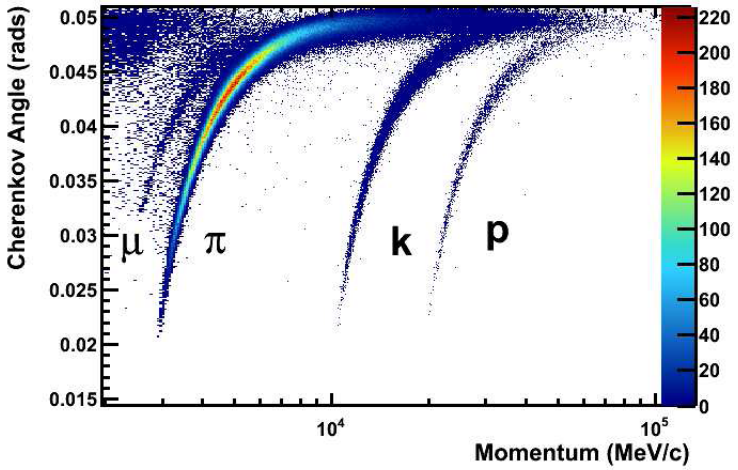

Figure 4.4: RICH pid

To achieve this goal, calibration strategies have been devised that will enable the performance to be measured from the data themselves. The decay chain $\Lambda^0 \rightarrow p\pi^-$ can be cleanly selected, based on its kinematic signature, without the use of RICH information. These events can be used as an unbiased sample for calibrating the RICH particle identification performance of pions and protons. In this way, the calibration method using the high purity samples of Λ's will be described.

4.2.1 RICH calibration with $\Lambda^0 \rightarrow p\pi^-$ decay

For both offline physics analyzes and online data monitoring, the ability to understand the performance of the RICH particle identification (PID) in a Monte Carlo independent manner is of vital importance. In order to achieve that signals which can be reconstructed without the inputs from the RICH have been looked for. If these signals can be very well isolated from the background we will obtain unbiased samples of identified final particles and thus we can evaluate the PID response from the detectors.

The method consists in developing a set of requirements in order that the signal be isolated from background. We proved that the method is efficient for $\Lambda \rightarrow p\pi^-$ decay, being thus useful for the identification of the protons and pions.

The same algorithm can be applied for other neutral resonances which decay into two charged particles. Thus, the method was extended to other resonances like $K^0_S \rightarrow \pi^-\pi^+$ for pions and $J/\psi \rightarrow \mu^+\mu^-$ for the muons. One can mention that the method can also be adapted for kaons with the decay $\phi \rightarrow K^+K^-$. The method also has the advantage that it uses particles abundantly produced in minimum bias events, which makes it useful in the online monitoring.

The selection employed makes use of the properties of the Λ^0 which decays weakly and has a long lifetime, a path of a few centimeters in the detector. Also, the fact that the mass of Λ^0 ($m_{\Lambda^0} = 1115.6\ MeV/c^2$) is very close to the proton mass ($m_{\Lambda^0} = 938.2\ MeV/c^2$) allows one to identify the proton from pion. The reconstruction algorithm selects the combination of two charged tracks which pass a list of conditions. The most energetic track was assumed to be the proton and the second the pion. In Fig. 4.5 we can see the large differences between proton and pion momenta.

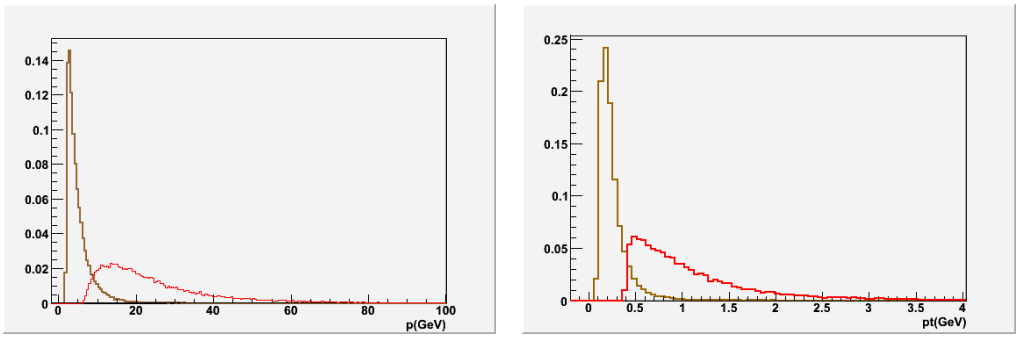

Figure 4.5: The large differences between momenta of proton and pion allows one to identify the two particles between them; a) Proton (red) and pion (brown) momentum b) Proton and pion transverse momentum

Then the condition for selecting secondary particles, i.e. not originating from the primary vertex was imposed, $\chi^2_{IP}(\pi) > 13$ and $\chi^2_{IP}(p) > 6$. The condition on the transverse momenta was left almost untouched since we would like to extend the range of the method to lower momenta, $p_T(\pi) > 0.1GeV/c$ and $p_T(p) > 0.5GeV/c$. The two tracks were required to form a vertex with higher probability, $\chi^2_{vtx}(\Lambda^0) < 10$, and then the distance from the primary vertex to the decay vertex was asked to be significant $\chi^2_{flight}(\Lambda^0) > 10$. The last condition imposed a

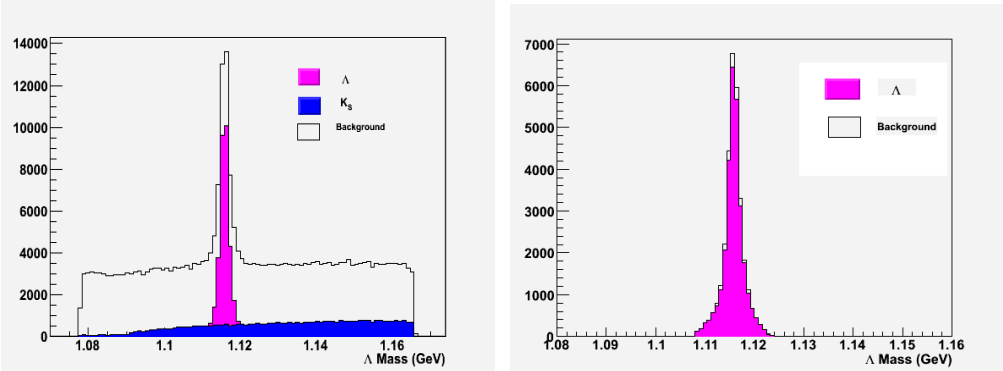

Figure 4.6: $p\pi$-invariant mass before (left) and after (right) the selection

narrow cut on the invariant mass of the reconstructed Λ^0, $|m(p\pi) - m_{PDG}(\Lambda^0)| < 1.5 GeV/c^2$ since we are less interested in optimizing the total efficiency but rather the purity.

In Fig. 4.6, left side, we see the invariant mass of pairs of tracks that were given the mass of proton and pion respectively. Without imposing the above cuts, the peak is already well shaped but it sits on a large combinatorial background. Also, misidentified pions coming from K_s produce a contamination of Λ^0 peak. For improving the above selection and also for rejecting the K_S background from the sample we use the Armenteros-Podolanski variables [103]. This amounts to the following change of the variables

$$(p_p, p_\pi, \cos\theta_{p\pi}) \rightarrow (p_\perp, \alpha, 1/P_\Lambda)$$

where: $\alpha = \frac{p_{p||} - p_{\pi||}}{P_\Lambda}$, $\alpha^* = \frac{m_p^2 - m_\pi^2}{M_\Lambda^2}$, $P_\Lambda = p_{p||} + p_{\pi||}$, p^*- momentum of the decay products in the C.M.S.; $p_\perp$, $p_{p||}$, $p_{\pi||}$ are defined relative to P_Λ direction.

The representation of the candidates in $p_\perp$ and α variables is shown in Fig. 4.7. The plot distinctly shows how the signal and background are separated.

The Λ^0, and K_S^0 shapes can be explained by rewriting the energy-momentum relation.

$$p_\perp^2 + \frac{(\alpha - \alpha^*)^2}{4(1/M_\Lambda^2 + 1/P_\Lambda^2)} = p^{*2} \tag{4.4}$$

Then the elliptic curves suggested by Eq. 4.4 are used to fit the signal region and

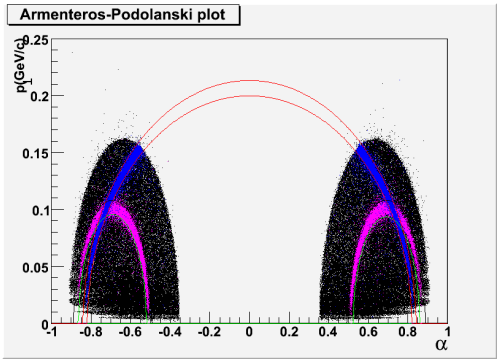

Figure 4.7: magenta - true $\Lambda/\bar{\Lambda}$, blue - true K_S, black - all combinations, red - signal regions $\Lambda\&K_S$ fitted with elliptic curves

identified as / selected	Purity	e	μ	π	K	p	No associated track	total
π	98%	3	10	13713	6	7	219	13958
p	96%	2	0	210	19	13479	248	13958
Λ	95%	-	-	-	-	-	-	13958

Table 4.1: Purities and statistics with particle misidentification. The main impurities for pions(π) and protons(p) come from tracks without association, those coming from electrons(e), muons(μ) and kaons(K) are much smaller.

select the true Λ^0 candidates.

4.2.2 Identification efficiency plots

In Table 4.1 the results on the purity of the sample of protons and pions are presented. The values are excellent and show the validity of the method, see also Fig. 4.6, right side for a plot of the invariant mass. The identification performances of this method are then evaluated as function of the momentum of the proton/pion. Identification/mis-identification efficiency curves for RICH as they are simulated by Monte Carlo are very well described by the efficiency curves obtained using data, see Fig. 4.8.

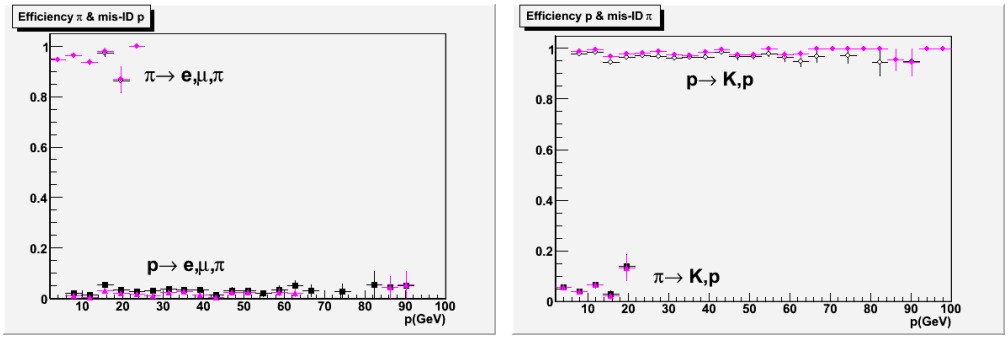

Figure 4.8: Black - pions and protons selected using kinematic cuts; Magenta - truth pions and truth protons selected using the same cuts. Up - identification efficiency curves; down - misidentification efficiency curves. Pions/protons are seen by the RICH as light (e, μ, π) particles or/and heavy (K, p) particles.

The results of this method were presented in a public conference [104] and used for calibrating the RICH detectors at LHCb. Further, use of these studies contributed to the publication of the first LHCb papers [105; 106; 107]. A summary of these first results of LHCb concerning soft physics can be found in [108].

4.3 Performance studies - Λ_b case

In Chapter 5 we present an analysis of the measurement of the production cross-section for Λ_b, reconstructing the following decay $\Lambda_b \rightarrow J/\psi(\mu^+\mu^-)\Lambda^0(p\pi)$. In order to reconstruct the Λ^0 a condition on proton PID of $\Delta \log \mathcal{L}(p-\pi) > -5$ is required, see Tabel 5.5. To express the final result for the cross-section we also need to evaluate the systematic uncertainties coming from different sources. Consequently, in this section we present a generic method for evaluating the systematic uncertainty associated with the PID conditions on the daughters, in our case only for the proton. The method is given in general terms which makes it suitable also for cases where more than one decay daughter has requirements on PID or when the efficiency has a dependency on more variables.

4.3.1 PID efficiency determination

Since the PID variables $\Delta \log \mathcal{L}(p - \pi)$ are poorly described in the Monte Carlo simulation, these data cannot be used to make a reliable determination of the PID cut efficiencies. Instead, it is necessary to invoke a data-driven technique to establish the PID efficiencies for all track types of interest; $K^{\pm}$, $\pi^{\pm}$, p and $\bar{p}$. This is achieved by exploiting the exclusive decays of particles copiously produced at the LHC, and whose final states include the aforementioned track types.

The weakly decaying V^0 hadrons—the K^0_S meson and the Λ baryon —are reconstructed through a selection algorithm completely devoid of PID requirements, as explained in the previous Section 4.2. This ensures that both decays provide samples of unbiased $\pi^{\pm}$, p and $\bar{p}$ tracks with purities in excess of 90%. For kaons the decay $\phi \to K^+K^-$ is used in general. However, in this case comparable purity is only achievable by exploiting PID information, thus a different method of tag-and-probe is used to obtain the calibration sample. To obtain an unbiased sample of $K^{\pm}$ tracks, a selection algorithm comprising of a RICH PID requirement on just one of the two daughter tracks is used. That is, at least one track is necessary to satisfy the requirement $\Delta \log \mathcal{L}(K - \pi) > -15$. The samples resulted after applying the selections are shown in Fig. 4.9 as the invariant mass for the respective signal. It can be seen that despite the use of RICH PID, the $\phi \to K^+K^-$ selection is still very much dominated by combinatoric background. In order to account for the genuine signal decays the ${}_sPlot$ [109; 110] method of discriminating signal from background is used. The same ${}_sPlot$ method is also employed in Λ_b measurement from Chapter 5 The method is able to unfold the contributions of different sources to the distribution of a data sample in a given variable. In our case the signal and the background are separated for $\Delta \log \mathcal{L}$ variables using as the control variable the invariant mass distributions which can be inferred from the fits such as in Fig. 4.9. Although the background contamination in the Λ^0 and K^0_s selections is small in comparison, this strategy has been employed to extract the true $\Delta\log\mathcal{L}$ distributions from all unbiased track samples.

Once the V^0 and ϕ samples have been background subtracted via the ${}_sPlot$ technique, it is possible to determine the identification (ID) and misidentification (misID) rates for a given PID requirement on each track type. The efficiencies

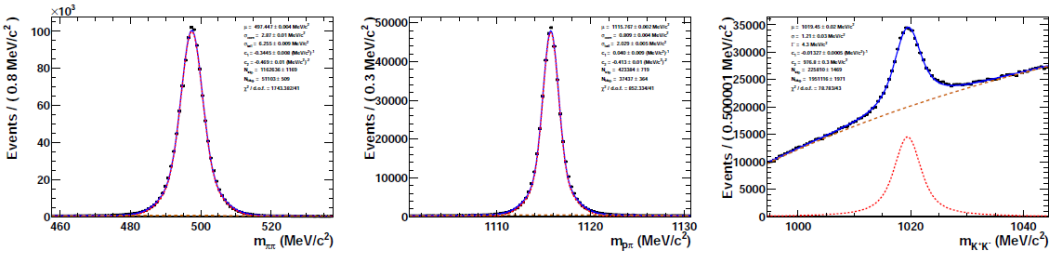

(a) $K^0_S \to \pi^+\pi^-$ (b) $\Lambda \to p\pi^-$ (c) $\Phi \to K^+K^-$

Figure 4.9: Invariant mass distributions reconstructed from the magnet up $\sqrt{s} = 7\,\text{TeV}$ data for (a) $K^0_S \to \pi^+\pi^-$, (b) $\Lambda \to p\pi^-$ and (c) $\phi \to K^+K^-$. The results of unbinned maximum likelihood fits to the data, together with their individual components, are superimposed.

obtained for the calibration samples cannot be used directly for a given signal mode, Λ_b in our case, since these eficiencies depend on the kinematics of each track and also in the case with more daughters tracks correlations exist amongst their kinematic variables.

We shall note with $\varepsilon(\mathbf{x})$ the efficiency for a given PID requirement upon a single track as a function of the kinematic variables, where $\mathbf{x}$ could be a combination of track variables total momentum, trasverse momentum, pseudorapidity or event variables like track multiplicity. And let f describe the distribution of, and the correlations between the kinematic variables of the signal decay daughter tracks. With these notations, the *average* efficiency for a n-body final state with PID requirements imposed on all tracks can be written as:

$$< \varepsilon > = \varepsilon(\mathbf{x}_1) \cdot \cdots \cdot \varepsilon(\mathbf{x}_n) \cdot f(\mathbf{x}_1, \mathbf{x}_2, \ldots, \mathbf{x}_n), \tag{4.5}$$

$$= \prod_{i=1}^{n} \varepsilon(\mathbf{x}_i) \cdot f(\mathbf{x}_1, \ldots, \mathbf{x}_n). \tag{4.6}$$

Knowledge of $\varepsilon(\mathbf{x})$ and $f(\mathbf{x}_1 ..., \mathbf{x}_n)$ can be determined from the collision data calibration samples and from the signal sample, respectively, using again the ${}_sPlot$ method. The same procedure can also be applied on Monte Carlo data where needed. In practice the ε and f functions are not known in every point of the phase space but within bins of the kinematic variables depending on the size

of the statistical samples. The discretized version of Formula 4.6 can be written:

$$< \varepsilon > = \sum_{i,..,\alpha} \varepsilon(\mathbf{x}_1^i) \cdot ... \cdot \varepsilon(\mathbf{x}_n^\alpha) \cdot f^{i,..,\alpha} \tag{4.7}$$

$$= \frac{\sum_{i,..,\alpha} \varepsilon(\mathbf{x}_1^i) \cdot ... \cdot \varepsilon(\mathbf{x}_n^\alpha) \cdot m^{i,..,\alpha}}{N}. \tag{4.8}$$

where the superior indices $i,\ldots,\alpha$ denote the respective bin in kinematic variable. With $m^{i,..,\alpha}$ we denoted the number of signals for that bin and with N the total number of signals in the sample.

An example of PID efficiency for calibration sample and signal data as well as the difference between the efficiencies calculated in a given bin is shown in Fig. 4.10.

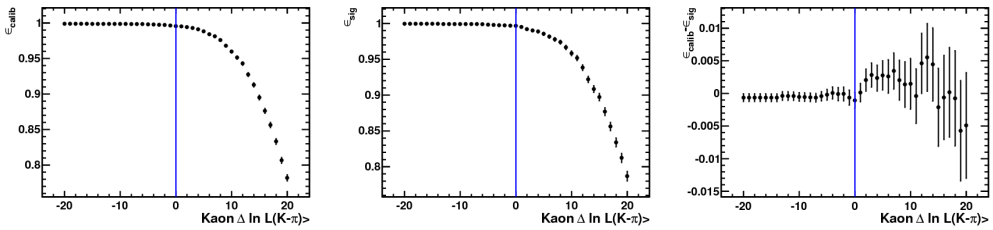

Figure 4.10: Construction of the Monte Carlo efficiency residual for the DzToKmpip pion in analysis bin (p_T, y)=([0.0,1.0[GeV/c, [3.5,4.0[). Efficiencies as a function of $\Delta \log \mathcal{L}$ cut using the Monte Carlo calibration data are shown in fig:PionEffCalMC while the corresponding truth values are shown in fig:PionEffSigMC. The difference between the two is shown in fig:PionResMC. No PID requirement has been imposed on the kaon track.

4.3.2 Assessment of systematic uncertainties

The steps described previously allow us to pass from the PID efficiencies calculated for the calibrating samples to the ones correspondig to the signals from a particular analysis. In the case of Λ_b analysis presented in Chapter 5, we are not directly interested in the identification efficiencies since these were included in the calculation of ε_{rec} term, see Section 5.3. We are only interested in extracting the systematic uncertainty introduced by the condition $\Delta \log \mathcal{L}(p-\pi) > -5$. The

most frequent choice of variables for describing the correlations and efficiencies are $|\vec{p}|$ and η. This assumes that the PID performance is entirely parameterized by the variables and the variations in PID performance across bins are negligible.

We start by evaluating the PID efficiency for proton shown in Fig. 4.10 for each bin in the phase space both for Monte Carlo samples as well as for the samples obtained from data.

This is done to account for any lateral shift in the $\Delta \log \mathcal{L}$ scale between Monte Carlo and collision data. Figure 4.11 demonstrates that, in the range of interest, while the general trend of the residual distribution in Monte Carlo and data are consistent, one is laterally shifted with respect to the other. To account for this, the residuals are considered within a range ± 5 of the nominal cut and the largest residual is taken as the systematic. This is repeated for all PID cuts and the resulting individual systematics summed in quadrature to determine the overall error.

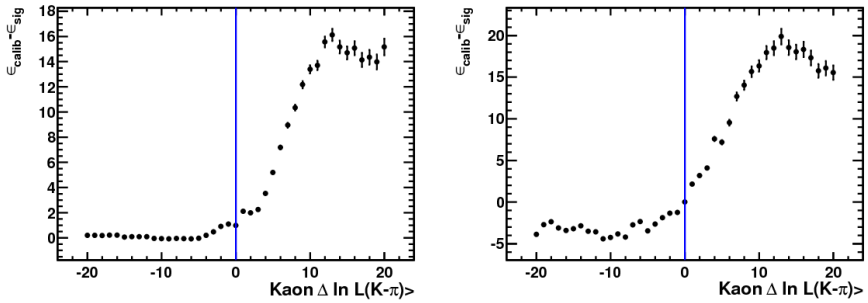

Figure 4.11: Residuals in kaon PID efficiency, for the decay mode $D^0 \to K^-\pi^+$ in analysis bin (p_T, y)=([4.0,5.0[GeV/c, [3.5,4.0[), as determined in calibration and signal for (a) Monte Carlo and (b) collision data as a function of $\Delta \log \mathcal{L}$ cut. No PID requirement has been imposed on the pion track.

The total systematic efficiency for each of the four different Λ_b samples considered are of order of 0.5% and agrees with the values found in the alternative method used in Section 5.5.10.

Chapter 5

Measurement of the $\Lambda_b \to J/\Psi\Lambda^0$ production cross-section

The production of b-baryons is yet an almost unexplored field, as they were out of reach at the b-factories and the amount of data recorded by the Tevatron experiments did not allow cross-section studies. Being a dedicated b-physics experiment covering a unique phase-space region amongst the LHC experiments, LHCb[28] can provide important contributions to the b-baryon production studies.

This Chapter presents a measurement of the Λ_b[1] cross section, $\sigma(pp \to \Lambda_b X)\mathcal{B}(\Lambda_b \to J/\psi\,\Lambda^0)$, for rapidity $2.2 < y < 4.5$ and transverse momentum $0 < p_{\rm T} < 13.0$ GeV/c.

We measure the inclusive Λ_b production cross-sections as follows:

$$\sigma(pp \to \Lambda_b X)\mathcal{B}(\Lambda_b \to J/\psi\,\Lambda^0) = \frac{N_{sig}}{\mathcal{L} \cdot \varepsilon_{total} \cdot \mathcal{B}(\Lambda^0 \to p\pi^-)\mathcal{B}(J/\psi \to \mu^+\mu^-)} \quad (5.1)$$

where N_{sig} is the total number of Λ_b candidates in the nominal sample measured in the $\Lambda_b \to J/\psi\,\Lambda^0$ final state, $\mathcal{L}$ is the luminosity, $\mathcal{B}(\Lambda^0 \to p\pi^-)$ and $\mathcal{B}(J/\psi \to \mu^+\mu^-)$ are the PDG [111] branching fraction of the decays $\Lambda^0 \to p\pi^-$ and $J/\psi \to \mu^+\mu^-$ and ε_{total} is the total efficiency to detect, reconstruct and select Λ_b. The study reported here uses 36.4 ± 1.3 pb^{-1} collected by LHCb in 2010 and presents in detail all the steps of the data analysis from selecting the data samples and detector configurations up to evaluating the systematic uncertainties

[1] We generically indicate both baryon states as Λ_b unless specifically mentioned.

and determining the final result. Some details about the efficiencies are presented in the Annex A.1.

5.1 Data Samples

The LHCb detector is a forward spectrometer described in Chapter 3 an also in more details in Ref. [77]. The LHCb coordinate system is defined having the x-axis in LHC plane pointing inside the circle and the y-axis perpendicular to the LHC plane pointing upwards. The z-axis completes the trihedral and is aligned with the collision direction. Two separate datasets were recorded in 2010: 18.57 pb^{-1} were collected with the magnetic field at positive polarity, $B_y < 0$, Magnet "Up", while 17.82 pb^{-1} were collected with the magnetic field at negative polarity, $B_y > 0$, Magnet "Down".

The data has been reconstructed with Brunel v37r8p4 and stripped with DaVinci v26r3p2 (Reco08-Stripping12) using the DIRAC production management system. For the measurement of the cross-section the events selected by the **Lambdab2JpsiLambda** stripping line were used. Furthermore all J/ψ collected in the **LEPTONICFULL** stream were used to measure the trigger efficiency.

5.1.1 Trigger

The LHCb trigger system consists of three levels (L0, HLT1 and HLT2) and was described in Section 3.2.1. In any of these three trigger levels an event can be selected by one or more set of requirements, so called "trigger-line". Each trigger line can be prescaled or postscaled by a fixed factor between 0 and 1.

The trigger requirements are modified during the data taking according to the changes in beam parameters and the needs of the collaboration, so that the data we analyze here has been collected under several different conditions. Each set of unique trigger conditions used by LHCb is identified by a Trigger Configuration Key, TCK. Any given TCK therefore corresponds to a unique combination of trigger lines for all the three trigger levels. For the purpose of this analysis the TCK and trigger lines were chosen not only to maximize the retention of data but also to have the lines as much as possible common to all TCK and, if possible,

with a prescaling factor 1. A list of all the TCK used for this analysis is shown in Table 5.1, where the HLT1 prescaling factors are also shown. The L0 and HLT2 line prescaling factors were all 1.

TCK	Lumi pb^{-1}	nEvts	Hlt1SingleMuonNoIPL0	Hlt1TrackMuon	Hlt1MuTrack
0x13001F	0.203	3864	1.0	-	1.0
0x19001F	0.860	16978	1.0	-	1.0
0x190024	0.774	12460	1.0	-	1.0
0x1D0030	0.162	1849	1.0	1.0	1.0
0x1E0030	2.150	21421	1.0	1.0	-
0x1F0029	3.060	18511	0.2	1.0	-
0x1F0031	0.123	709	0.2	1.0	-
0x24002A	1.248	11790	1.0	1.0	-
0x24002C	1.103	10172	1.0	1.0	-
0x25002A	0.036	236	0.2	1.0	-
0x25002C	2.023	11525	0.2	1.0	-
0x2A002A	4.253	41626	1.0	1.0	-
0x2A002C	0.483	4705	1.0	1.0	-
0x2B002A	1.919	11840	0.2	1.0	-
0x2E002A	8.709	87310	1.0	1.0	-
0x2E002C	8.887	89043	1.0	1.0	-
-	36.395	344039	-	-	-

Table 5.1: List of TCK used in the measurement of the Λ_b production cross-section. The integrated luminosity, number of events and the HLT1 prescaling factors for each line are also shown. The L0 and HLT2 prescaling factor is 1 for all the lines.

This analysis is based on two L0 lines common to all data collected in 2010: the **single muon** line, which requires one muon candidate with a p_{T} larger than 1.4 GeV/c, and the **di-muon** line, which requires two muons with p_{T} larger than 0.56 GeV/c and 0.48 GeV/c respectively.

Two HLT1 lines are used to collect the majority of the data analyzed here. The first one, present in all the samples, is the **Hlt1SingleMuonNoIPL0** which confirms the muon candidate found by the L0 single muon trigger, and applies a harder cut on the muon p_{T} at 1.8 GeV/c. The second one, **Hlt1TrackMuon,** which is not present in all TCKs, is kept to enhance the number of events in this analysis. It checks for a positive response from L0 single muon and L0 dimuon lines, and selects events with well defined tracks and at least one muon. Besides these two main lines a third one **Hlt1MuTrack** is added for the small part of the data where the optimized line **Hlt1TrackMuon** was not available.

At the HLT2 level only the trigger line **Hlt2DiMuonUnbiasedJPsi,** was used. It selects events having two muon candidates with an invariant mass within 120 MeV/c^2 of the J/Ψ mass and applies cuts on the vertex and track χ^2.

A summary of all the L0, HLT1 and HLT2 lines and their selection criteria is presented in Table 5.2. The only events used in the measurement of the Λ_b cross-section are those in which the muons selected by all three trigger levels originate from the decay of Λ_b into a J/ψ, so called TOS, Trigger On Signal, events. All other types of events have been discarded. In particular this analysis does not use Trigger Independent of Signal, TIS, events, i.e. those in which no signal particle was selected by the trigger.

trigger line	**main requirements**
L0Muon	$p_T > 1.4\,\mathrm{GeV}/c$
L0DiMuon	$p_{T_1} > 0.56\,\mathrm{GeV}/c \quad p_{T_2} > 0.48\,\mathrm{GeV}/c$
Hlt1SingleMuonNoIPL0	L0Muon and $p_T > 1.8\,\mathrm{GeV}/c \quad \chi^2_\mu < 16 \quad \chi^2_\mu/\mathrm{ndf} < 10$
Hlt1TrackMuon	L0DiMuon||L0Muon and $p_T > 800\,\mathrm{MeV}/c$, $p > 8\,\mathrm{GeV}/c$, #TrackHits> 9, |# missed VELO hits| < 3, $\chi^2/\mathrm{ndf} < 10$, $\|IP\| > 110\,\mu\mathrm{m}$
Hlt1MuTrack	L0Muon and $p_T(\mu) > 800\,\mathrm{MeV}/c$, $p_T(\mathrm{tr}) > 600\,\mathrm{MeV}/c$, $\chi^2/\mathrm{ndf} < 16$, $\|IP\| > 50\,\mu\mathrm{m}$, $M_{\mu\mathrm{tr}} > 1000\,\mathrm{MeV}/c$, $\mathrm{DOCA}_{\mathrm{vtx}} > 200\,\mu\mathrm{m}$
Hlt2DiMuonUnbiasedJPsi	$\mid M_{\mu\mu} - M_{J/\psi} \mid < 120\,\mathrm{MeV}/c \quad \chi^2_{V_{\mu\mu}} < 25$

Table 5.2: Summary of the trigger lines used for this analysis and their most important selection criteria.

In order to determine the trigger efficiency with TISTOS method, see section 5.3.3, a data set enriched in J/ψ mesons has been used, stripping line LEPTONICFULL.DST.

A set of Global Event Cuts, GEC, is applied to the events at the beginning of each trigger step in order to discriminate those which would require an excessive amount of time to be reconstructed. They exploit the correlation between reconstruction CPU time and sub-detector hit multiplicity and are summarized in Table 5.3. The only GEC that rejects a significant fraction of the data sample is the requirement on the number of maximum VELO clusters.

	#SPD hits	# VELO clusters	# VELO tracks	# IT clusters	# OT clusters
L0	< 900	-	-	-	-
HLT1	-	< 3000	-	< 3000	< 10000
HLT2	-	-	< 350	-	-

Table 5.3: Summary of global event cuts (GEC).

5.1.2 Luminosity measurement

Additionally to the Van der Meer scan method [105; 112] LHCb uses another method [105] that exploits the high resolution of the VErtex Locator (VELO) subdetector and the small distance between this and the beam to measure beam parameters such as positions, angles and widths in beam-beam and beam-gas interactions. Combining the results of both techniques it is possible to measure the integrated luminosity over the whole data taking period used by this analysis with an error of 3.5 %, obtaining 36.4 ± 1.3 pb^{-1}.

5.1.3 Monte Carlo samples

The Monte Carlo samples used in this analysis were generated with Gauss v39r2 package [113]. The Gauss simulation software uses PYTHIA [21], version 6.421 with the new multiple interaction model, to produce pp collisions with the parameters detailed in [114], and the EvtGen package [94] to generate the subsequent decays. GEANT4, version 9.2 [115], is used for the detector simulation.

The Monte Carlo datasets that are used in this note, correspond to the Summer/Autumn 2010 data taking conditions. We use two distinct samples:

- A fully simulated $\Lambda_b \to \Lambda^0(p\pi^-)J/\Psi(\mu^+\mu^-)$ decay sample, with at least one Λ_b candidate in the LHCb acceptance, event type 15144100, requiring an average number of interactions per beam-crossing $\nu = 2.5$. The trigger conditions used in this simulation correspond to TCK 0x2E002A.

- A Λ_b Monte Carlo "gen-only" sample, generated using the exact same parameters as the previous one, but without requesting the Λ_b candidate to be in the LHCb acceptance. It is used to measure the small correction associated to the edges of the phase space, sec. 5.3.1, and therefore only the generator level quantities are saved.

Events in these samples have been generated both for the Magnet Up and for the Magnet Down polarities, always assuming a flat polarization for the Λ_b.

5.2 Reconstruction and selection

The Λ_b candidates are selected in two separate and consecutive steps: stripping and offline analysis. In the stripping stage, performed centrally as part of the standard LHCb data processing procedure [116; 117], J/ψ and Λ^0 are identified and combined to produce Λ_b candidates. Selection criteria are applied to all three particles to reduce the dataset to a more manageable size. Since this dataset is used by all analyses requiring a sample of Λ_b, the selection criteria are as loose as possible and they are designed to avoid any bias in the sample itself. In the offline analysis the Λ_b candidates are confirmed and tighter criteria are applied on all particles.

Given the Λ^0 long lifetime the final state pion and proton can be reconstructed either as a pair of long-tracks or as a pair of downstream-tracks with comparable probability. In order to maximize the statistics both kinds of events are used to measure the Λ_b production cross-section, however they are analyzed separately as they are subject to different systematics effects. For similar reasons the data set is further split according to the b-quark content of the Λ_b and to the polarity of the magnetic field. This results in eight particle and antiparticle samples named LLPUp, LLPDw, DDPUp, DDPDw, LLNUp, LLNDw, DDNUp and DDNDw, where the first two letters denote the track type, long-long (LL) or downstream-downstream (DD), the third letter keeps track of the b-quark content and is denoted after the sign of the proton from Λ^0, positive (P) or negative (N), and the remaining two letters the field polarity, Up or Down (Dw).

J/ψ selection

The first step of the stripping algorithms is to reconstruct a J/ψ from two muons of opposite charge. Track quality and muon identification are guaranteed by applying cuts on $\chi^2_{\text{tr}}/\text{ndf}$ and on $\Delta\mathcal{L}_{\mu\pi}$, where the first is the track fit reduced χ^2 and the second the muon identification variable, built as the difference in logarithms of the global likelihood of the muon hypothesis with respect to the pion one. The quality of the J/ψ candidate is ensured by applying a cut on the vertex fit χ^2 and requiring the invariant mass of the muon pair to be within $80\,\text{MeV}/c^2$ of the PDG value of the J/ψ mass.

Decay mode	Cut parameter	Stripping	Offline
$J/\psi \to \mu\mu$	$\Delta \ln \mathcal{L}_{\mu\pi}$	> 0	> 0
	$\chi^2_{\rm tr}/{\rm ndf}(\mu)$	< 5	< 4
	$min(p_{\rm T}(\mu^+), p_{\rm T}(\mu^-))$	-	$> 0.5\,{\rm GeV}/c$
	$\chi^2_{\rm vtx}(J/\psi)$	< 16	< 11
	$\lvert M_{\mu^+\mu^-} - M_{J/\psi_{PDG}}\rvert$	$< 80\,{\rm MeV}/c^2$	$< 55\,{\rm MeV}/c^2$

Table 5.4: $J/\psi \to \mu\mu$ selection. The selection cuts applied on the muons and on the J/ψcandidate are shown for both the stripping and the offline selection. When no cut is applied in one of the two selection steps a "-" is used.

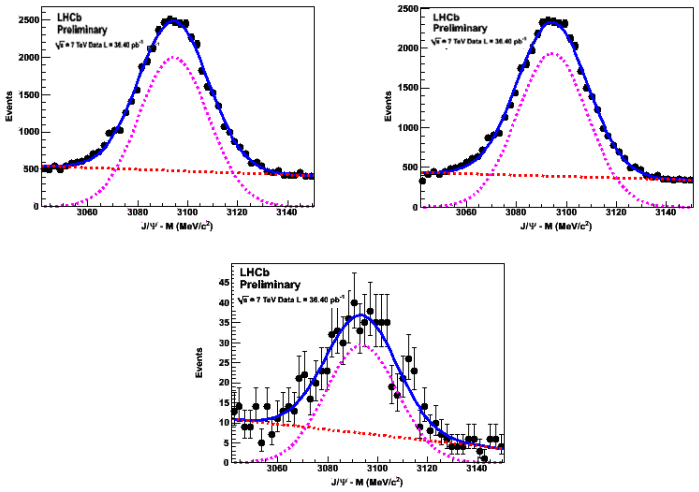

Figure 5.1: The J/ψ invariant mass after the stripping is shown in the left plot. The central plot shows the same quantity after the offline J/ψ selection, while the right plots shows it after the final Λ_b selection when the Λ^0 is reconstructed with DD tracks. The fits for J/ψ are only illustrative and were not used in the analysis.

The J/ψ candidate is confirmed in the offline analysis where tighter cuts are applied on some of the variables just described. Furthermore offline it is required that the minimum p_T of both muons is at least $0.5\,{\rm GeV}/c$.

The cuts applied either in the stripping or in the offline analysis to select J/ψ candidates are summarized in Table 5.4 and the invariant mass distributions after the stripping and offline selections are shown in Fig. 5.1.

Decay mode	Cut parameter	Stripping	Offline
$\Lambda^0 \to p\pi$	$\Delta \ln \mathcal{L}_{p\pi}$	$> -5(LL)$	$> -5(LL)$
	$\chi^2_{\text{IP}}(p,\pi)$	$> 9(LL), 4(DD)$	$> 9(LL), 4(DD)$
	$\chi^2_{\text{tr}}/\text{ndf}(p,\pi)$	< 10	< 4
	$p_{\text{T}}(\pi)$	$> 0.1\,\text{GeV}/c$	$> 0.1\,\text{GeV}/c$
	$p_{\text{T}}(p)$	$> 0.5\,\text{GeV}/c$	$> 0.5\,\text{GeV}/c$
	$p(p,\pi)$	$> 2\,\text{GeV}/c$	$> 2\,\text{GeV}/c$
	$\chi^2_{\text{vtx}}/\text{ndf}(\Lambda^0)$	< 20	< 20
	$\lvert M_{p\pi} - M_{\Lambda^0}\rvert$	$< 15\,\text{MeV}/c^2$	$< 6\,\text{MeV}/c^2$
	$\lvert M_{p\pi} - M_{K^0_S}\rvert$	-	$> 8(LL), 14(DD)\,\text{MeV}/c^2$
	$p_{\text{T}}(\Lambda^0)$	-	$> 1\,\text{GeV}/c$

Table 5.5: $\Lambda^0 \to p\pi$ selection cuts. The selection cuts applied on the protons, pions and on the Λ^0 candidate are shown for both the stripping and the offline selection. The Λ^0 can be reconstructed from a pair of long-tracks (LL) or downstream-tracks (DD), the different values for the cuts are indicated. When no cut is applied in one of the two selection steps a "−" is used.

Λ^0 selection

Events in which at least one J/ψ candidate is identified constitute the input to the Λ^0 selection. As mentioned before Λ^0 candidates can be reconstructed either from a pair of long-tracks (LL) or from a pair of downstream-tracks (DD). In the stripping step the quality of the tracks is ensured by applying cuts to the track $\chi^2_{\text{tr}}/\text{ndf}$, momentum and transverse momentum. In order to reduce the combinatorial background a minimum impact parameter resolution χ^2_{IP} from all primary vertices is required for both the p and the π candidate. The value of all these cuts is in general different for the proton and the pion and also for LL and DD combinations, a summary is shown in Table 5.5. The pion and the proton are combined to form a Λ^0 vertex, candidates are accepted if the vertex fit $\chi^2_{\text{vtx}}/\text{ndf}$ is < 20 and the mass of the pion-proton pair is within $6\,\text{MeV}/c^2$ of the PDG Λ^0 mass.

Analogously to what done for the J/ψ, the Λ^0 is confirmed in the offline analysis applying tighter cuts on the variables just mentioned as shown in Table 5.5. The Λ^0 transverse momentum is required to be above $1\,\text{GeV}/c$ and its proper time to be larger than 5 times its error σ_τ.

A source of background for the Λ^0 is constituted by $K^0_S \to \pi\pi$ decays in which one of the two tracks is mistakenly assigned the proton mass. This contribution is removed requiring that the Λ^0 mass reconstructed when π PID hypothesis is used for its daughters, is not within 8 MeV/c^2 of the K^0_S PDG mass in the case of long-tracks and 14 MeV/c^2 in the case of downstream-tracks. Figure 5.2 shows the mass distribution for both long and downstream-tracks Λ^0 candidates after the stripping and the offline selection.

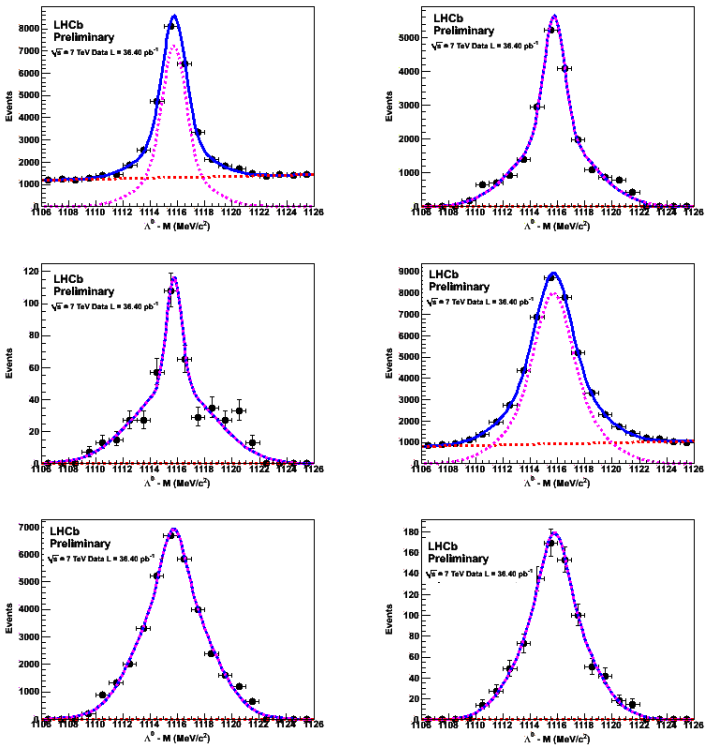

Figure 5.2: Events in which a J/ψ has been identified are the input to the Λ^0 selection. The left plots shows the $\Lambda \to p\pi$ candidates invariant mass after stripping, the central one shows the same quantity after imposing only the selection conditions specific to Λ^0 and the right hand side plot after the final Λ_b selection. The top row is obtained from LL tracks, while the bottom row is obtained from DD tracks. The fits for Λ^0 are only illustrative and were not used in the analysis.

In Figure 5.3 the transversal momentum spectrum is shown for Λ after the stripping cuts in the left side, and after imposing also the specific selection cuts for Λ^0 in the right side. Also distinct curves are shown for candidates which were

reconstructed from long-long tracks of the daughters (black curve) and the ones reconstructed from the downstream-downstream tracks.

A similar plot shows the the transversal momentum spectra for $\bar{\Lambda}^0$ in Figure 5.4.

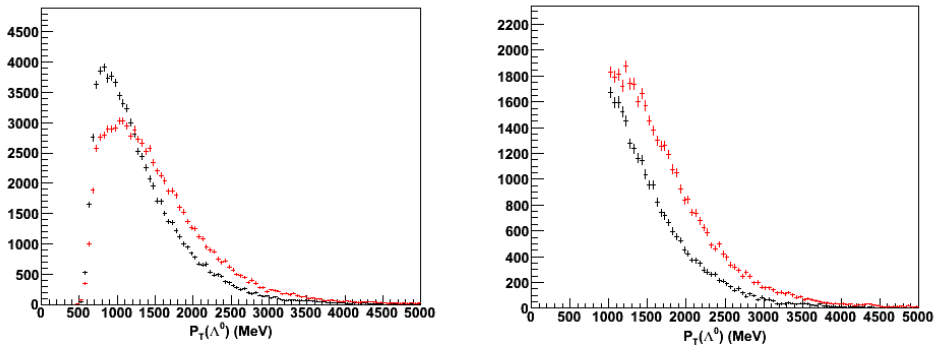

Figure 5.3: The left plots shows the $\Lambda^0 \to p\pi^-$ candidates transversal momentum after stripping. The black curve is candidates with long-long tracks while the red curve is for candidates with downstream-downstream candidates. The same plot is shown in the right side after imposing the selection cuts for Λ^0.

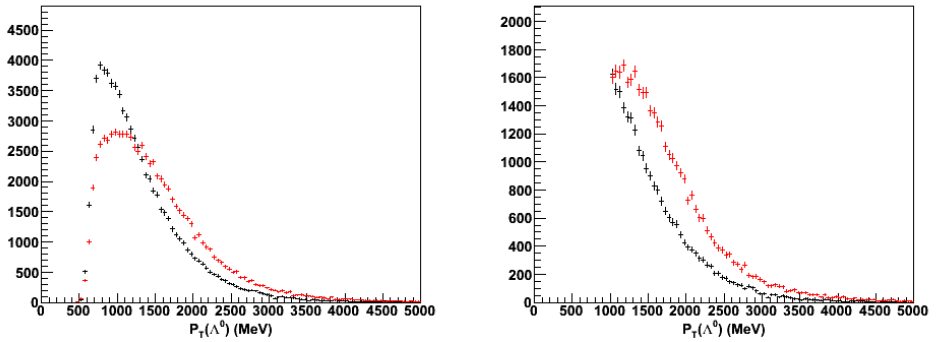

Figure 5.4: The left plots shows the $\bar{\Lambda}^0 \to p^-\pi^+$ candidates transversal momentum after stripping. The black curve is candidates with long-long tracks while the red curve is for candidates with downstream-downstream candidates. The same plot is shown in the right side after imposing the selection cuts for $\bar{\Lambda}^0$.

Decay mode	Cut parameter	Stripping	Offline
$\Lambda_b \to J/\psi\Lambda$	M_{Λ_b}	$\in (5120, 6120)\,\mathrm{MeV}/c^2$	$\in (5370, 5870)\,\mathrm{MeV}/c^2$
	$\chi^2_{\mathrm{vtx}}/\mathrm{ndf}(\Lambda_b)$	< 20	< 10
	χ^2_{IP}	-	< 20
	$\tau(\Lambda_b)$	-	> 0.25ps

Table 5.6: $\Lambda_b \to J/\psi\Lambda$ selection cuts. When no cut is applied in one of the two selection steps a "$-$" is used.

$\Lambda_b \to J/\psi\Lambda^0$ selection

Events in which at least a J/ψ and a Λ^0 candidate are reconstructed are the input to the third and final stage of the selection. All J/ψ and Λ^0 pairs are combined to form a candidate Λ_b, the mass of the combination is required to be in the [5120, 6120] MeV/c^2 range and a cut is applied on the vertex fit χ^2/ndf.

In the offline analysis the candidates selected by the stripping are required to have a vertex fit reduced $\chi^2_{\mathrm{vtx}} < 10$ and the Λ_b χ^2_{IP} from all primary vertices is required to be < 20.

All selection criteria for the Λ_b candidates are summarized in Table 5.6. The invariant mass of the Λ_b candidates after the stripping and the offline selection is shown in Fig. 5.5.

Phase space of the measurement

The events that pass all the above selections are shown in as distribution of p_T and y in Fig. 5.6. The plots are dominated by background and show that for rapidity between 2.0 and 2.2 we have next to no event such that the phase space for the measurement was chosen to be $p_T \in (0, 13)$GeV/c and $y \in (2.2, 4.5)$.

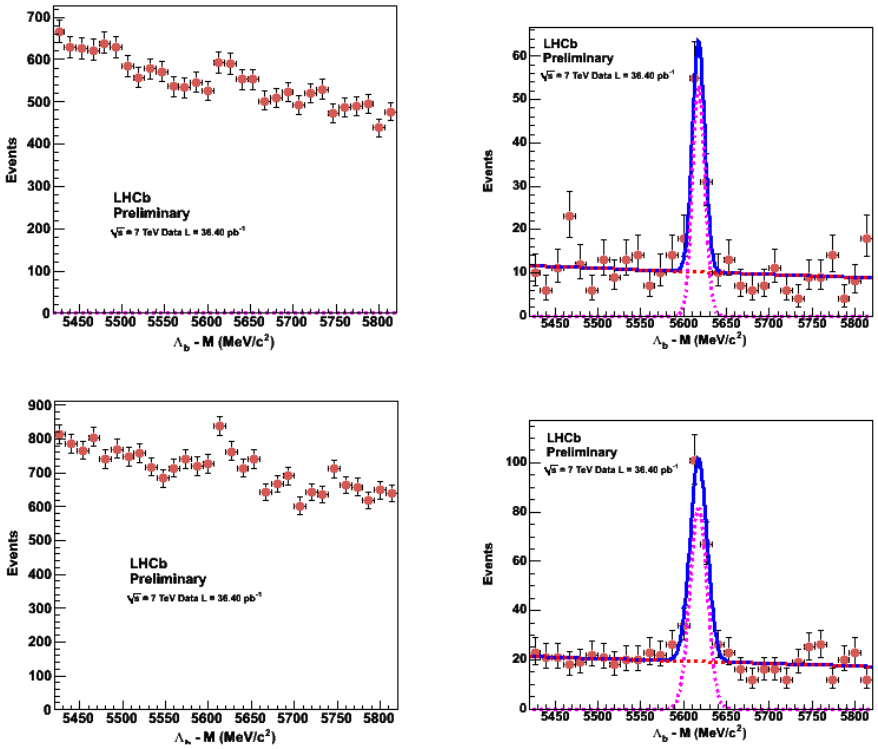

Figure 5.5: The invariant mass distribution for $\Lambda_b \to J/\psi\Lambda^0$ candidates after the stripping (left) and the offline selection (right). The top row is for candidates obtained from LL Λ^0 while the bottom is obtained from DD Λ^0.

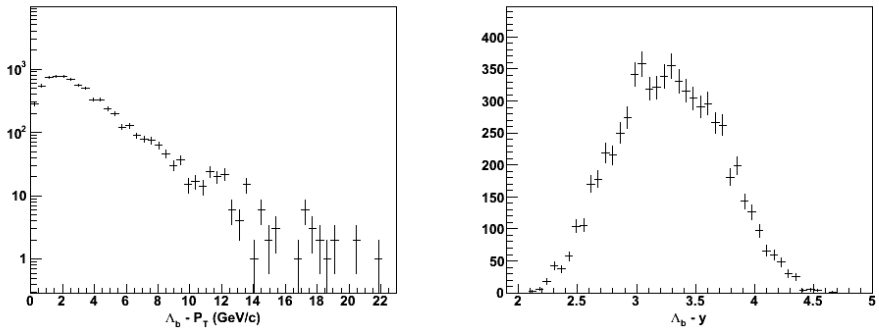

Figure 5.6: The candidates from all types of events (Λ_b or $\bar{\Lambda}_{bb}$, with magnet Up or Down polarity etc.) are shown in p_T and y axis.

5.3 Efficiencies

The total efficiency is factorised in three different components

$$\epsilon^{tot} = f_A \times \epsilon^{rec} \times \epsilon^{trig}. \tag{5.2}$$

where f_A is a factor correcting for the geometric acceptance, ϵ^{rec} combines the detector acceptance, detection, reconstruction and selection efficiencies and ϵ^{trig} is the the trigger efficiency.

The first two terms are estimated from Monte Carlo simulations while the trigger efficiency is computed from data with the TISTOS method. Due to the detector geometrical acceptance this analysis is performed in the phase space limited by the transverse momentum and rapidity intervals $p_T < 13$ GeV/c and $2.2 < y < 4.5$.

The total efficiency, and each of its components, are heavily dependent on the Λ_b transverse momentum and rapidity. In order to improve the measurement and to account more easily for possible differences between the data and the Monte Carlo, the efficiency has been calculated dividing the phase space in bins of p_T and y. As it will be shown later, this allows weighting each event for the efficiency effect corresponding to its position in the phase space. The number of bins is specific to each type of the efficiency and they have in general different dimensions, being optimized to have roughly the same number of candidates in data/MC.

5.3.1 Geometric acceptance correction

The Monte Carlo sample generated centrally by the collaboration for $\Lambda_b \to J/\psi\Lambda^0$ selects only the events with Λ_b in the LHCb acceptance, defined as a having the polar angle $\theta \in [10, 400]$ mrad. A correction is needed to take into account those events in which the Λ_b is not in the acceptance but the final products are and thus the decay chain can be reconstructed. The "gen-only" sample of simulated $\Lambda_b \to J/\psi\Lambda^0$ decays described in section 5.1.3 has been used to estimate the correction factor f_A as:

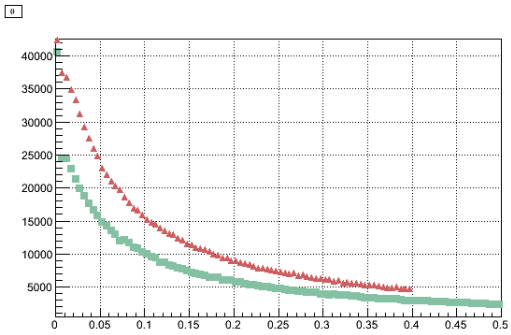

Figure 5.7: Distributions of the simulated Λ_b polar angle θ angle for the fully simulated MC sample (green) and the "gen-only" sample (red) in the case of magnet down polarity.

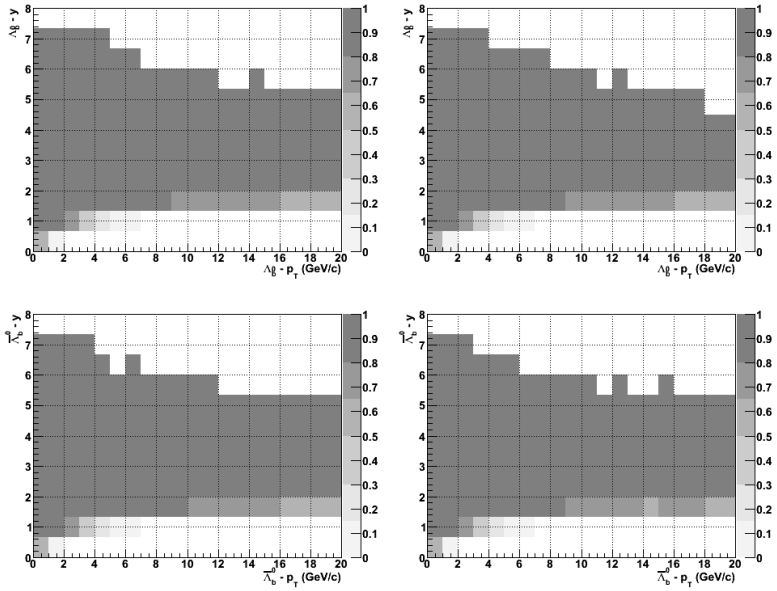

Figure 5.8: The correction factor for geometrical acceptance is measured separately in the four samples Λ_b and Magnet Up polarity (a), Λ_b and Magnet Down polarity (b), $\bar{\Lambda}_b$ and Magnet Up polarity (c) and $\bar{\Lambda}_b$ and Magnet Down polarity (d). For the large part of the phase space concerning this study the corection factor is 1.

$$f_A(p_T, y) \quad = \quad \frac{N^{gen-only}_{10<\theta<400}(p_T, y)}{N^{gen-only}(p_T, y)}, \tag{5.3}$$

- $n^{gen-only}(p_T, y)$ is the number of $\Lambda_b \rightarrow J/\psi\Lambda^0$ events generated in one $[p_T, y]$

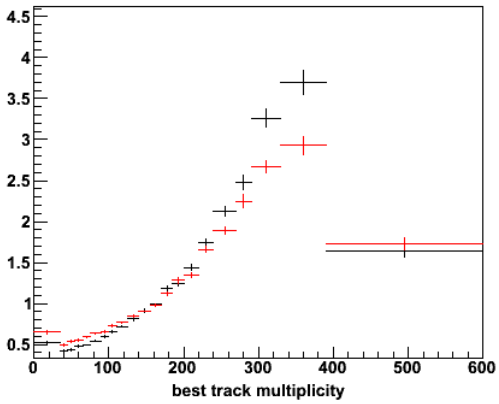

Figure 5.9: In order to account for differences between the simulated data and the sample collected in 2010, the Monte Carlo distributions are reweighted using the ratios of the "best track multiplicity" shown here, in red for Magnet Up sample and in black for Magnet Down sample.

bin in the "gen-only" sample;

- $n^{gen-only}_{10<\theta<400}(p_T, y)$ is the number of $\Lambda_b \to J/\psi\Lambda^0$ events generated in the same $[p_T, y]$ bin in the official LHCb MC sample

The geometric acceptance is measured independently for Λ_b and $\bar{\Lambda}_b$ and for the two magnet polarities. As an example of the size of the acceptance Figure 5.7 shows the θ distributions for Λ_b generated with the Magnet Down both within and outside the LHCb acceptance.

Figure 5.8 shows the shapes of this factor as function of the Λ_b y and p_T for all four samples. For the large part of the phase space concerning this study the correction factor is 1.

From the "gen-only" sample one can infer the fraction from the 4π volume represented by the fiducial volume of this analysis. This was found to be 15.6%.

5.3.2 Reconstruction efficiency

The loss of efficiency due to the requirements that all the tracks of the baryons daughters are in the acceptance, they are reconstructed and selected is calculated as a unique factor ϵ^{rec} as:

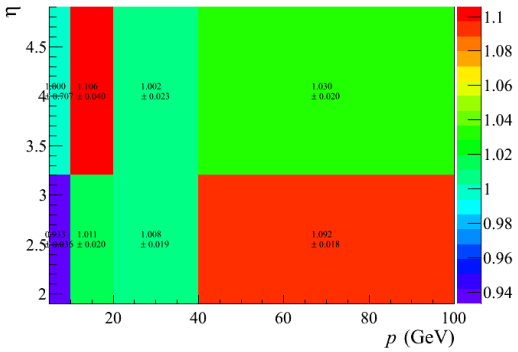

Figure 5.10: The weights used to correct the MC samples for the LL candidates in order to account for the differences in the tracking efficiency as compared to data depend in general on the particle momentum and pseudorapidity. The axis labels need fixing e.g. GeV $\rightarrow$ GeV/c

$$\epsilon^{rec} = \frac{N^{rec}}{N^{gen}_{10<\theta<400}}, \tag{5.4}$$

where

- N^{rec} is the number of $\Lambda_b \rightarrow J/\psi\Lambda^0$ events detected, reconstructed and selected after the offline analysis described in section 5.2 in a $[p_T, y]$ bin.
- $N^{gen}_{10<\theta<400}$ is the number of $\Lambda_b \rightarrow J/\psi\Lambda^0$ events generated in the same $[p_T, y]$ bin having required that the polar angle θ of the Λ^0_b is in the interval [10, 400] mrad before the magnet.

The reconstruction efficiency is evaluated as a function of p_T and y for each of the eight types of events LLPUp, LLPDw, DDPUp, DDPDw, LLNUp, LLNDw, DDNUp and DDNDw using the fully simulated $\Lambda_b \rightarrow J/\psi\Lambda^0$ sample described in section 5.1.3. As already mentioned, in these samples are simulated events with an average number of interactions $\nu = 2.5$, while data was collected in 2010 with a widely varying value of ν. This difference may introduce non negligible errors in the measurement of ϵ^{rec}. In particular it has been found [118] there are significant variations in the tracking efficiency depending on the value of ν. In order to account for these variations the Monte Carlo distributions are reweighted using the ratio of the best track multiplicity between the data collected in 2010

and the Monte Carlo simulation, shown in Fig. 5.9. The tracking efficiency is also dependent on the particle momentum and pseudorapidity [118], unfortunately the distributions of these quantities are significantly different in data and simulation. The Monte Carlo sample therefore undergoes a further event by event reweighting using the set of tables described in reference [118] and shown in Fig. 5.10. The weights are in general different for long and downstream tracks, but they do not depend on the magnet polarity and on the Λ_b flavour.

The small number of bins in the $p-\eta$ maps is driven by the limited statistics available in the simulation. This also affects the measurement of the error on the weights.

The measured ϵ^{rec} is shown in figure 5.11 for all eight types of events as function of the Λ_b transverse momentum and rapidity.

5.3.3 Trigger efficiency

The trigger efficiency is the combined efficiency of L0 × HLT1 × HLT2 trigger as defined in section 5.1.1. As already mentioned, only TOS events have been used to measure the Λ_b cross section, i.e. those in which all three trigger levels have recognized muons originating from the decay of the Λ_b into a J/ψ. With this in mind it is possible to define the trigger efficiency as:

$$\epsilon^{trig} = \frac{1}{1 + \frac{N^{TIS\cancel{TOS}}_{J/\psi}}{N^{TISTOS}_{J/\psi}}} \tag{5.5}$$

where:

- $N^{TIS\cancel{TOS}}_{J/\psi}$ is the number of J/ψ candidates detected, reconstructed and selected by our J/ψ specific selection criteria, which are "TIS" and not "TOS".
- $N^{TISTOS}_{J/\psi}$ is the number of J/ψ candidates detected, reconstructed and selected by our J/ψ specific selection criteria, which are both "TIS" and "TOS".

It is also useful to define a third class of events $\cancel{TIS}TOS$:

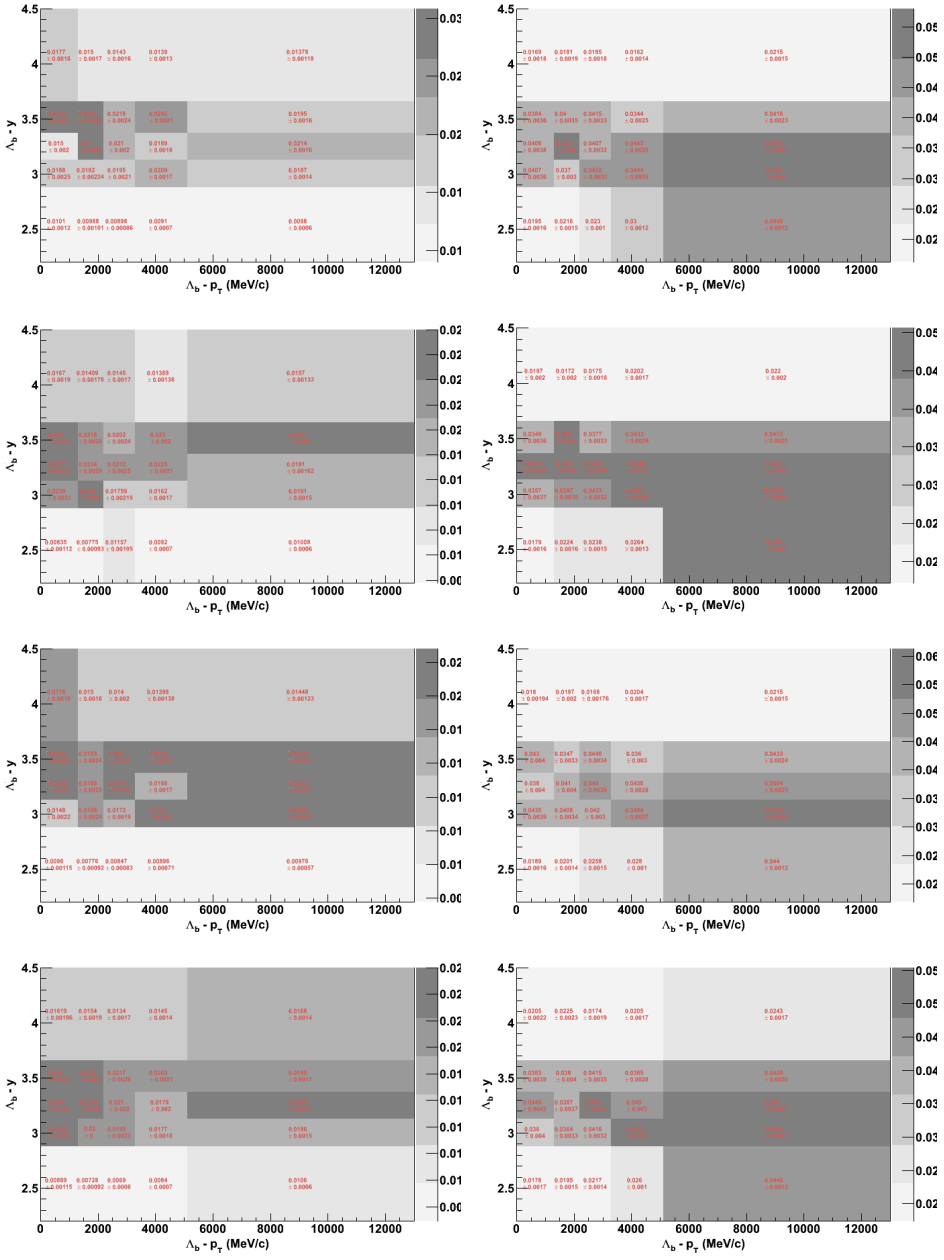

Figure 5.11: The top four plots show the detector acceptance, detection, reconstruction and selection efficiency as a function of p_T and y for Λ_b where the Λ^0 is reconstructed as LL (left) and DD (down) and the magnet polarity is "Up" (top row) and "Down" (second row). The same quantities are shown in the bottom four plots for $\bar{\Lambda_b}$. The explicit values for each bin can be found in tables from appendix A.1.1

- $N_{\mathrm{J}/\psi}^{\cancel{TIS}TOS}$ is the number of J/ψ candidates detected, reconstructed and selected by our J/ψ specific selection criteria, which are "TOS" and not "TIS".

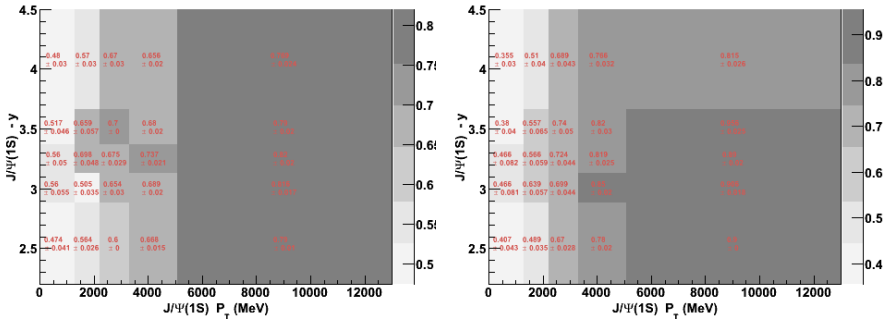

Figure 5.12: Λ_b^0 trigger efficiency obtained from TISTOS method as a function of p_T and y for Magnet Up and Magnet Down samples.

The number of J/ψ candidates passing the selections are estimated by fitting the respective mass distributions separately 5×5 bins of the J/ψ rapidity and transverse momentum. The function used to fit the distribution is a double sided Crystal Ball:

$$\mathrm{f}_{\mathrm{CB}}^{J/\psi}(\mathrm{x}) = \begin{cases} \mathrm{e}^{-\frac{1}{2}\alpha_{\mathrm{L}}^2}\left(\dfrac{\mathrm{n_L}}{\mathrm{n_L} - \alpha_{\mathrm{L}}^2 - \alpha_{\mathrm{L}}\delta_\sigma \mathrm{x}}\right)^{\mathrm{n}_L} & \text{for } \delta_\sigma \mathrm{x} < -\alpha_{\mathrm{L}} \\ \mathrm{e}^{-\frac{1}{2}\delta_\sigma \mathrm{x}} & \text{for } -\alpha_{\mathrm{L}} < \delta_\sigma \mathrm{x} < \alpha_{\mathrm{R}} \\ \mathrm{e}^{-\frac{1}{2}\alpha_{\mathrm{R}}^2}\left(\dfrac{\mathrm{n_R}}{\mathrm{n_R} - \alpha_{\mathrm{R}}^2 + \alpha_{\mathrm{R}}\delta_\sigma \mathrm{x}}\right)^{\mathrm{n}_R} & \text{for } \delta_\sigma \mathrm{x} > \alpha_{\mathrm{R}}, \end{cases} \tag{5.6}$$

where $\delta_\sigma \mathrm{x} = \dfrac{\mathrm{x} - \mathrm{m}_0^{J/\psi}}{\sigma^{J/\psi}}$.

The left correction for $\delta_\sigma \mathrm{x} < -\alpha_{\mathrm{L}}$ accounts for internal and external bremstrahlung emission, while the right correction for $\delta_\sigma \mathrm{x} > \alpha_{\mathrm{R}}$ is an empirical addition describing the non-Gaussian tail observed in the J/ψ invariant mass distribution. The same set of parameters $\mathrm{n_L} = 2.7, \alpha_{\mathrm{L}} = 1.70$ and $\mathrm{n_R} = 3.0, \alpha_{\mathrm{R}} = 1.85$ has been used for all kinematical range of J/ψ mesons, while the J/ψ mass position, $\mathrm{m}_0^{J/\psi}$, and its resolution, $\sigma^{\mathrm{J}/\psi}$, in general will depend on the kinematical range of J/ψ-mesons.

For each of the 25 bins the invariant mass of ~~TIS~~TOS events were fitted with the double Crystal Ball function and the $m_0^{J/\psi}$ and $\sigma^{J/\psi}$ values so obtained were used in the subsequent fits of the TIS~~TOS~~ and TISTOS samples. The number of signal events obtained from these fits are used to estimate the trigger efficiency according to Eq. 5.5, the results are shown in Fig. 5.12.

5.3.4 Efficiency Scale Factors

The efficiencies calculated according to Eq. 5.2 are scaled by an overall factor before they are used to estimate the $\Lambda_b \to J/\psi\Lambda^0$ yield. This factor corrects for effects due to the trigger or the reconstruction that cannot be taken into account in the procedure outlined in the previous sections and it can be split in several components.

The first component compensates for the loss in efficiency due to the trigger global event cuts described in section 5.1.1. It has been shown that the only global event cut affecting the trigger selection of the muon originating from the J/ψ decay is the requirement that the number of Velo clusters has to be smaller than 3000. The effect of this cut has been measured to be a reduction of the trigger efficiency by a factor $(98.2 \pm 0.1)\%$ in simulated data and $(97.3 \pm 0.6)\%$ in the data collected in 2010 [119]. In this study we use this last value determined from data.

In order to cross-check that the muon identification efficiency is the same in data and in Monte Carlo the tag-and-probe method [120] has been applied to samples of 2010 data and of simulated data. The results of this study indicate that the measured muon identification efficiency is higher in data than in simulation and the efficiency ϵ^{tot} has to be scaled by a second factor $\mathrm{SF}^{\mu_{ID}} = (102.4 \pm 1.12)\%$ [29].

The vertex reconstruction efficiency is found to be smaller by 1.6% in Monte Carlo compared to data and the assigned systematic error is 0.8% [29]. In order to account for this a final scale factor $\mathrm{SF}^{VTX} = 98.4\%$ is used.

The total scaling factor used to multiply the total efficiency from Eq. 5.2 is:

$$SF^{tot} = \mathrm{SF}^{GEC} \cdot \mathrm{SF}^{\mu_{ID}} \cdot \mathrm{SF}^{VTX} = 0.9804 \cdot \tag{5.7}$$

5.4 Event yields

The Λ_b candidates selected following the procedure outlined in the previous sections are split according to their b-quark flavour, the proton and pion track types and the magnet polarity. The number of signal candidates in each of these eight sample is estimated by using of an unbinned fit of the invariant mass distribution. In the fit procedure the signal is assumed to be distributed as a Gaussian while the background is described by a straight line. The Λ_b and $\bar{\Lambda}_b$ samples are grouped in 4 pairs according to the track type and magnet polarity, e.g. LLPUp and LLNUp. These pairs are fitted simultaneously with the constraint that the mean value and the sigma of the Gaussian are the same.

The results of the fits are shown in Fig. 5.13, 5.14 and the measured yields, central mass and signal sigma are listed in Table 5.7.

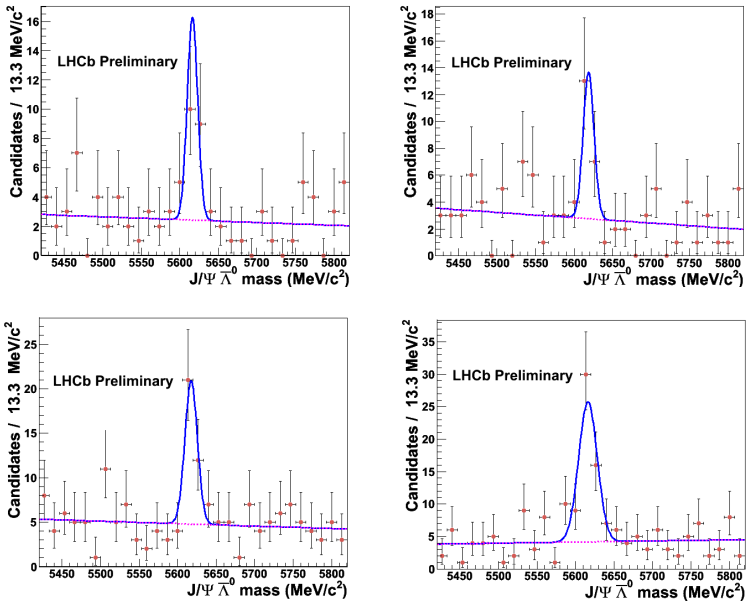

Figure 5.13: $\bar{\Lambda}_b \to J/\psi \bar{\Lambda}^0$ mass fit for the 4 samples. From left to right and top to bottom the samples are: LLNUp, LLNDw, DDNUp, DDNDw. The first two letters denote the $\bar{\Lambda}^0$ daughters track type, long-long (LL) or downstream-downstream (DD), the third letter the b-quark content, positive (P) or negative (N), and the remaining two letters the field polarity, Up or Down (Dw).

The *sPlot* is used in conjunction with this model to extract a statistical weight

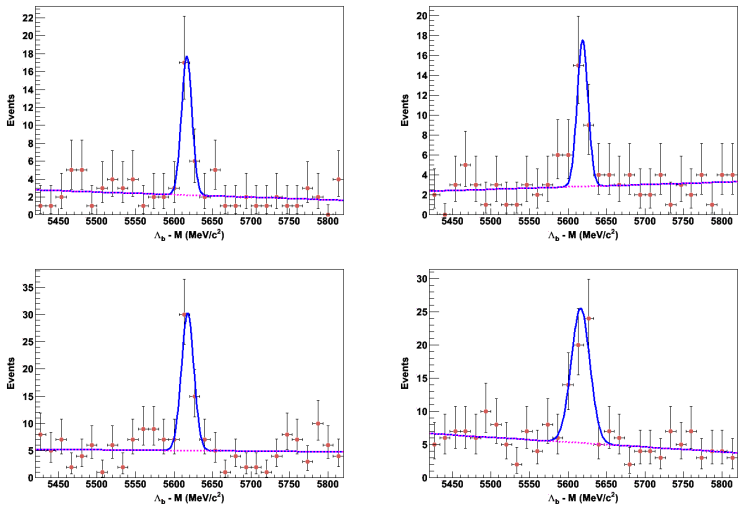

Figure 5.14: $\Lambda_b \to J/\psi\Lambda^0$ mass fit for the 4 samples. From left to right and top to bottom the samples are: LLPUp, LLPDw, DDPUp, DDPDw. The first two letters denote the Λ^0 daughters track type, long-long (LL) or downstream-downstream (DD), the third letter the b-quark content, positive (P) or negative (N), and the remaining two letters the field polarity, Up or Down (Dw).

w_{SP} for each event estimating the probability of it being a true signal event. The efficiency corrected number of $\Lambda_b \to J/\psi\Lambda^0$ decays has been extracted weighting each event by:

$$w_{TOT} = \frac{w_{SP}}{\epsilon^{tot}(p_T, y)} \tag{5.8}$$

The weighted yield so obtained is used to estimate the total number of $\Lambda_b \to J/\psi\Lambda^0$, $N^{corr}_{\Lambda_b}$. The estimated total numbers together with the information on luminosity an branching ratios provide us eight measurements of the cross section.

5.5 Systematic studies

A number of systematic effects have been studied, and their impact on the cross-section measurement quantified.

Type	LLPUp	LLPDw	DDPUp	DDPDw	LLNUp	LLNDw	DDNUp	DDNDw
mass	5616±1	5619±2	5618±1	5616±2	5616±1	5619±2	5618±1	5616±2
sigma fit	6.80±1.24	7±2	8.08±1.40	12±2	6.80±1.24	7±2	8.08±1.40	12±2
raw yield	19.8±5.2	19.4±5.8	38.3±7.6	45.9±8.4	17.7±4.9	14.37±4.75	24.5±6.3	48.8±8.8
corrected yield	2544±859	3183±954	2709±737	2774±724	2440±870	1287±585	1413±479	3321±785
lumi	18.6±0.6	17.8±0.6	18.6±18.6	17.8±0.6	18.6±0.6	17.8±0.6	18.6±18.6	17.8±0.6
xsection	3687±1245	4807±1441	3927±1068	4190±1093	3537±1261	1944±884	2048±695	5015±1185

Table 5.7: The invariant mass distribution of each of the eight samples is fitted with a Gaussian + straight line in order to measure the signal yield. The measured central value for the Λ_b mass and its σ are also shown.

5.5.1 Fit model

The yields have been measured assuming the Λ_b invariant mass is distributed as a Gaussian while the background has been described by a straight line. The eight samples are grouped in four pairs, the two samples in each pair being fitted simultaneously constraining the mean and the sigma of the Gaussian distributions to be the same. Given the small statistics in each sample a complete study of the fit model is not possible. The systematic uncertainty due to the choice made in this analysis has therefore been assessed making small changes to the fit model or by changing the way the sample are grouped before the fits. For example the constraint on the Gaussian mean has been removed in some of the tests, and/or the background has been modeled as an exponential. The weighted average of the difference between each test case and the nominal one according to formula 5.9, provides an estimate of the uncertainty introduced the particular choice of the fitting model.

$$\sigma = \sqrt{\frac{\sum_{i=1}^{n} \frac{(x_i - x_0)^2}{\sigma_i^2}}{\sum_{i=1}^{n} \frac{1}{\sigma_i^2}}} \pm \sqrt{\frac{1}{\sum_{i=1}^{n} \frac{1}{\sigma_i^2}}}, \tag{5.9}$$

where x_0 is the nominal measurement and x_i and σ_i, $i \ldots n$, are the mean and the sigma of each test.

The following grouping and constraints have been tried:

1. The nominal case: a Gaussian for the signal and a linear function for the background. The samples are grouped in pairs by track type and magnet polarity: (LLPUp, LLNUp), (DDPUp, DDNUp), (LLPDw, LLNDw) (DDPDw, DDNDw). Both the Gaussian mean and sigma are constrained

to be the same in the two samples of each pair.

2. A Gaussian for the signal and a linear function for the background. The samples are grouped in pairs by track type and b-quark charge: (LLPUp, LLPDw), (DDPUp, DDPDw), (LLNUp, LLNDw), (DDNUp, DDNDw). Both the Gaussian mean and sigma are constrained to be the same in the two samples of each pair.

3. A Gaussian for the signal and a linear function for the background. The samples are grouped in quartets by track type: (LLPUp, LLNUp, LLPDw, LLNDw), (DDPUp, DDNUp, DDPDw, DDNDw). Only the Gaussian sigma is constrained to be the same in the four samples of each quartet.

4. A Gaussian for the signal and a linear function for the background. The samples are grouped in pairs by track type and b-quark charge: (LLPUp, LLPDw), (DDPUp, DDPDw), (LLNUp, LLNDw), (DDNUp, DDNDw). Only the Gaussian sigma is constrained to be the same in the two samples of each pair.

The next four case repeat the previous four, replacing the background description from a polynomial to an exponential.

5. This model is similar to the nominal with the exception that the background is modeled by an exponential function.

6. A Gaussian for the signal and an exponential function for background. The samples are grouped in pairs by track type and b-quark charge: (LLPUp, LLPDw), (DDPUp, DDPDw), (LLNUp, LLNDw), (DDNUp, DDNDw) Both the Gaussian mean and sigma are constrained to be the same in the two samples of each pair.

7. A Gaussian for the signal and an exponential function for the background. The samples are grouped in quartets by track type: (LLPUp, LLNUp, LLPDw, LLNDw), (DDPUp, DDNUp, DDPDw, DDNDw). Only the Gaussian sigma is constrained to be the same in the four samples of each quartet.

8. A Gaussian for the signal and an exponential function for background. The samples are grouped in pairs by track type and b-quark charge: (LLPUp, LLPDw), (DDPUp, DDPDw), (LLNUp, LLNDw), (DDNUp, DDNDw) Only the Gaussian sigma are constrained to be the same in the two samples of each pair.

The results are shown in Table 5.8.

model	LLPUp	LLPDw	DDPUp	DDPDw	LLNUp	LLNDw	DDNUp	DDNDw
2.	4236±1593	5160±1487	4108±1117	3900±1024	3522±1269	1886±864	2170±747	4852±1166
3.	3479±1122	4677±1427	4122±1123	4093±1069	3540±1267	1921±876	2132±732	4697±1148
4.	3826±1308	4767±1432	4104±1115	3894±1020	3525±1268	1812±824	2167±748	4907±1173
5.	3713±1255	4847±1448	3929±1068	4221±1093	3544±1261	1970±889	2052±695	5021±1186
6.	4262±1602	5404±1555	4116±1119	4089±1067	3529±1269	1909±867	2173±747	4661±1119
7.	3518±1136	4511±1374	4124±1123	4126±1070	3547±1267	1865±843	2137±732	4704±1149
8.	3866±1326	4795±1437	4106±1116	3924±1021	3532±1267	1912±862	2171±748	4910±1173
nominal	3687±1245	4807±1441	3927±1068	4190±1093	3537±1261	1944±884	2048±695	5015±1185
fit sys	284±491	280±548	171±420	200±397	9.38±478.86	67.4±325.1	102±278	234±438
%	7.7±13.3	5.8±11.4	4.36±10.69	4.77±9.48	0.265±13.540	3.47±16.73	4.99±13.56	4.67±8.73

Table 5.8: The Λ_b production cross-section (pb) has been evaluated with different choices for the fit model. The weighted average of the difference between each test case and the nominal result provides an estimate of the systematic uncertainty introduced by the choice of one particular fit model.

5.5.2 Unknown Λ_b polarization

According to some models [121; 122] Λ_b produced in unpolarized pp interactions can present a non-zero polarization. As the total efficiency of detecting a Λ_b can depend on its polarization, one needs to estimate the uncertainty introduced by the assumption in the simulation that the Λ_b is not polarized. In principle a full angular analysis is required, but, since the Monte Carlo requires only that the Λ_b is produced within the LHCb angular acceptance, and the efficiency to reconstruct the daughters is calculated in bins of their kinematic variables, one can simplify and consider only the transverse case.

Under this assumption the Λ_b polarization reveals itself in the asymmetry of the distribution of the angle θ_Λ, Figure 5.15, defined as the angle between the normal of the Λ_b production plane and the momentum vector of the Λ^0 decay daughter, as seen in the Λ_b rest frame. The acceptance correction in this variable

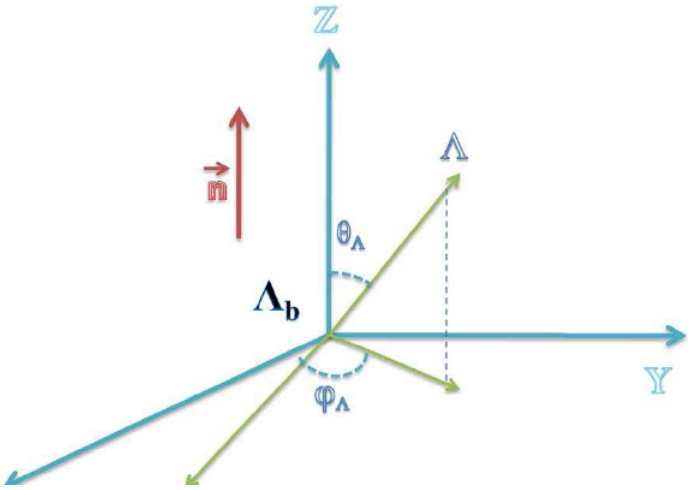

Figure 5.15: Λ_b polarization angles in the Λ_b rest frame.

can then be expressed as:

$$w(\theta_\Lambda, P_{\Lambda_b}) \propto (1 + P_{\Lambda_b}\alpha_{\Lambda_b}\cos(\theta_\Lambda)) \tag{5.10}$$

where $\alpha_{\Lambda_b} = -0.457$ [121; 122] is the decay asymmetry parameter of Λ_b and P_{Λ_b} is the Λ_b polarization.

	LLPUp	LLPDw	DDPUp	DDPDw	LLNUp	LLNDw	DDNUp	DDNDw
$P_{\Lambda_b} = -1$	3658±1233	4941±1494	3955±1083	4167±1094	3511±1262	1871±870	2042±696	5003±1161
$P_{\Lambda_b} = +1$	3722±1260	4684±1395	3901±1056	4217±1095	3568±1262	2017±900	2054±694	5042±1218
nominal	3687±1245	4807±1441	3927±1068	4190±1093	3537±1261	1944±884	2048±695	5015±1185
pol sys	31.9±881.4	128±1020	27±756	25.4±774.0	28.8±892.3	72.8±625.4	6±492	20.2±840.2
%	0.865±23.906	2.66±21.21	0.688±19.246	0.607±18.475	0.81±25.23	3.74±32.18	0.293±24.000	0.403±16.754

Table 5.9: The uncertainty introduced by a the lack of knowledge of the polarization of the Λ_b is estimated calculating the production cross-section (pb) in the two worst case scenarios, $P_{\Lambda_b} = +1$ and $P_{\Lambda_b} = -1$ and comparing the results with the nominal case where no polarization is assumed.

The uncertainty is extracted considering the two extreme cases for the polarization $P_{\Lambda_b} = +1$ and $P_{\Lambda_b} = -1$ and comparing them with the nominal measurement where no polarization is assumed. Each event in the MC dataset is weighted with the Eq. 5.10 and the total efficiency is recomputed in each case. The results are presented in the Table 5.9 and they are used to estimate the systematic uncertainty for the polarization following Eq. 5.9.

variable	nominal	LL-	LL+	DD-	DD+
$\mu - P_T$ (MeV/c)	500	-3	-	-3	-
$\mu - \chi^2_{trk}$	4	-0.25	0.25	-0.25	0.25
$\Delta LL - \mu$	0	-0.001	-	-0.001	-
$J/\Psi - \lvert M - M_{PDG}\rvert$ (MeV/c^2)	55	-2.7	2.7	-2.7	2.7
$J/\Psi - \chi^2_{vtx}$	11	-0.25	0.25	-0.25	0.25
$\pi^- - P_T$ (MeV/c)	100	-1	-	-1	-
$p - P_T$ (MeV/c)	500	5	-	5	-
$p, \pi^- - P$ (MeV/c)	2000	20	-	20	-
$p, \pi^- - \chi^2_{trk}$	4	-0.25	0.25	-0.25	0.25
$\Lambda^0 - P_T$ (MeV/c)	1000	10	-	10	-
$\Lambda^0 - \lvert M - M_{PDG}\rvert$ (MeV/c^2)	6	-1.3	1.3	-1.8	1.8
$\Lambda^0 - \chi^2_{vtx}$	20	-0.25	-	-0.25	-
$\Lambda^0_b - \chi^2_{IP}$	20	-0.3	0.3	-0.3	0.3
$\Lambda^0_b - \chi^2_{vtx}/ndf$	10	-0.25	0.25	-0.25	0.25
$\Lambda^0_b - \lvert M - M_{PDG}\rvert$ (MeV/c^2)	500	-5.8	-	-6.6	-
$\Lambda^0_b - \tau$(ps)	0.25	0.035	0.035	0.045	-0.045

Table 5.10: The systematic uncertainty associated to the selection cuts is estimated varying the cut by $\pm\sigma_{VAR}$. The values for σ_{VAR} in general can depend whether the Λ^0 was reconstructed as LL or DD tracks and the direction of the modification. All 4 σ_{VAR} are shown for each variable.

5.5.3 Selection criteria

In order to estimate the systematic uncertainty associated to the selection cuts applied to extract the signal, the values of the cuts employed in the offline selection have been varied, where possible, by $\pm\sigma_{VAR}$ where σ_{VAR} is the uncertainty on the cut variable.

The values for the different σ_{VAR} have been chosen studying the error distributions of the variable in the case of the Λ_b proper time and mass and of the Λ^0 mass, while for the other variables the measured error established from general studies on detector performance has been used. Different values were used for the LL and DD cases and for the "+" or "-" direction of the variation where appropriate. It has to be noted that in some cases, for example because of the previous cut in the stripping, it is possible to study the variation only in one direction. Table 5.10 contains a full list of the values of σ_{VAR} for each variable in the LL and DD case, or a "-" when the study could not be performed.

The results obtained for each cut modifying its limit by $+\sigma_{VAR}$ and $-\sigma_{VAR}$ have been combined according to Eq. 5.9. The contribution of all cuts have then been combined together, as in Ref. [123; 124] to produce a single value for the uncertainty due to the selection. Where the variables on which the cut is applied can be correlated full correlation has been assumed.

Table 5.11 shows the results for every single variable and the final combination.

model	LLPUp	LLPDw	DDPUp	DDPDw	LLNUp	LLNDw	DDNUp	DDNDw
$\mu - P_T$	3693±1247	4812±1443	3929±1069	4191±1093	3537±1261	1944±884	2054±696	5024±1187
$\mu - \chi^2_{trk}$	3703±1239	4822±1444	3969±1072	4184±1091	3085±1173	1964±888	2091±698	4983±1179
$\Delta LL\mu$	3687±1245	4807±1441	3927±1068	4190±1093	3537±1261	1944±884	2048±695	5015±1185
$J/\Psi - \lvert M - M_{PDG}\rvert$	3617±1281	4586±1406	3954±1070	4190±1093	3584±1267	1953±860	1920±675	5003±1176
$J/\Psi - \chi^2_{vtx}$	3696±1247	4806±1441	3928±1068	4190±1093	3548±1266	1944±884	2049±695	5015±1185
$\pi^- - P_T$	3695±1248	4807±1441	3929±1069	4190±1093	3553±1262	1945±884	2049±695	5015±1185
$p - P_T$	3687±1245	4807±1441	3927±1068	4190±1093	3537±1261	1944±884	2048±695	5015±1185
$p, \pi^- - P$	3613±1211	4861±1460	3940±1071	4169±1099	3470±1247	1951±888	2055±698	5025±1188
$p, \pi^- - \chi^2_{trk}$	3804±1309	4651±1404	3958±1074	4203±1095	3240±1225	1970±865	2068±697	5063±1191
$\Lambda^0 - P_T$	3695±1247	4874±1456	3949±1073	4209±1091	3552±1265	1976±898	2060±700	4715±1146
$\Lambda^0 - \lvert M - M_{PDG}\rvert$	3679±1178	4877±1446	3768±1083	4139±1083	3431±1228	2038±891	1878±694	4762±1191
$\Lambda^0 - \chi^2_{vtx}$	3687±1245	4849±1449	3927±1068	4190±1093	3537±1261	1949±887	2049±695	5016±1185
$\Lambda^0_b - \chi^2_{IP}$	3687±1245	4899±1460	3927±1068	4214±1095	3538±1261	1988±895	2047±695	5089±1187
$\Lambda^0_b - \chi^2_{IP}$	3688±1246	4897±1459	3845±1051	4192±1094	3539±1261	1957±891	2040±689	5017±1186
$\Lambda^0_b - \lvert M - M_{PDG}\rvert$	3687±1245	4807±1441	3927±1068	4190±1093	3537±1261	1944±884	2048±695	5015±1185
$\Lambda^0_b - \tau$	3992±1422	4623±1422	4113±1089	4204±1092	3280±1254	2135±884	1775±630	4864±1176
nominal	3687±1245	4807±1441	3927±1068	4190±1093	3537±1261	1944±884	2048±695	5015±1185
select sys	41.7±52.4	18±60	5.53±44.50	5.3±45.4	14.00±52.98	11.17±36.78	39.8±28.8	28.0±49.3
%	1.13±1.42	0.376±1.246	0.1409±1.1330	0.127±1.084	0.396±1.498	0.575±1.892	1.94±1.40	0.558±0.983

Table 5.11: The cross section (pb) has been measured varying the selection cuts by $\pm\sigma_{VAR}$, the results, shown here, have been compared to the nominal measurement to extract the systematic uncertainty.

5.5.4 Trigger efficiency

The uncertainty due to the error on the measured trigger efficiency has been evaluated modifying the contribution to the weights used to estimate the yields due to the trigger efficiency. Random weights are generated from a Gaussian distribution centered on the measured value of the weight and of width equal to the error on the weight, and they assigned to each event. The cross-section

	LLPUp	LLPDw	DDPUp	DDPDw	LLNUp	LLNDw	DDNUp	DDNDw
nominal	3687±1245	4807±1441	3927±1068	4190±1093	3537±1261	1944±884	2048±695	5015±1185
%	2.93±0.07	3±0	2.4±0.1	3.84±0.09	2.23±0.05	5.03±0.11	2.46±0.06	4.48±0.10

Table 5.12: Systematic uncertainty on the Λ_b cross-section due to error in the measurement of the trigger efficiency.

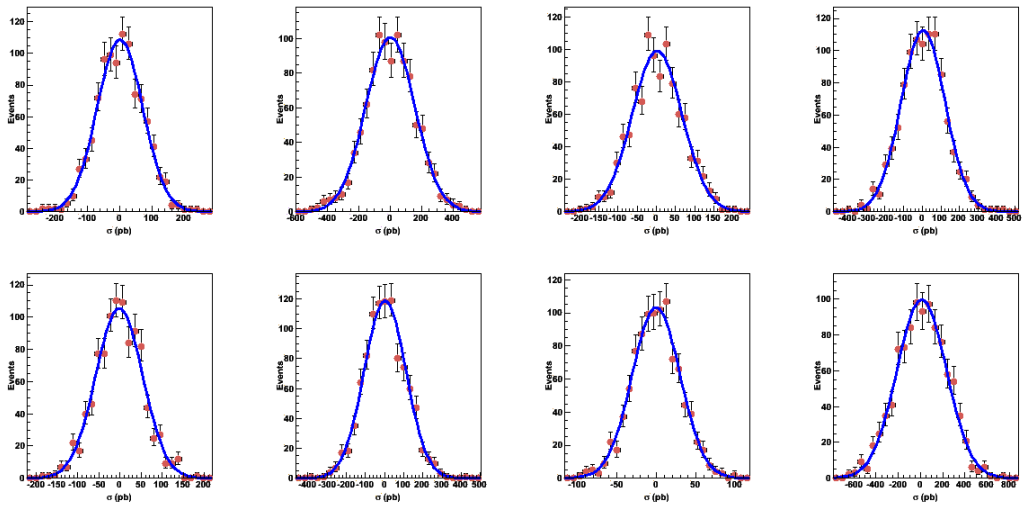

Figure 5.16: The cross-section in each of the eight samples is recalculated 1000 times varying the contribution to the event weights due to the trigger efficiency according to a Gaussian. The distribution of the 1000 measurements is described by a Gaussian, whose width provides an estimate of the systematic uncertainty.

is recomputed using these modified weights and the procedure is repeated 1000 times. The 1000 different values so obtained for the cross-section are plotted, Figure 5.16, and the distribution fitted as a Gaussian. The width of the Gaussian provides an estimate of the uncertainty due to the error on the trigger efficiency measurement. The estimates obtained for all eight Λ_b samples are shown in Table 5.12.

5.5.5 Reconstruction & selection efficiency

The uncertainties introduced by the limited statistics in Monte Carlo samples used to extract the detector acceptance, reconstruction and selection efficiency as defined in Section 5.3.2 are studied varying the event weights contribution due to the selection efficiency in the same way as done for the trigger efficiency. Figure 5.17 shows the cross-section distribution obtained after generating 1000 sets of Gaussian weights. The estimated uncertainty is shown in Table 5.13.

	LLPUp	LLPDw	DDPUp	DDPDw	LLNUp	LLNDw	DDNUp	DDNDw
nominal	3687±1245	4807±1441	3927±1068	4190±1093	3537±1261	1944±884	2048±695	5015±1185
%	4.02±0.09	4.34±0.10	2.59±0.06	3.57±0.08	4.27±0.10	7.6±0.2	3.05±0.07	3.32±0.08

Table 5.13: Systematic uncertainty on the Λ_b cross-section due to error in the measurement of the detector acceptance, reconstruction and selection efficiency.

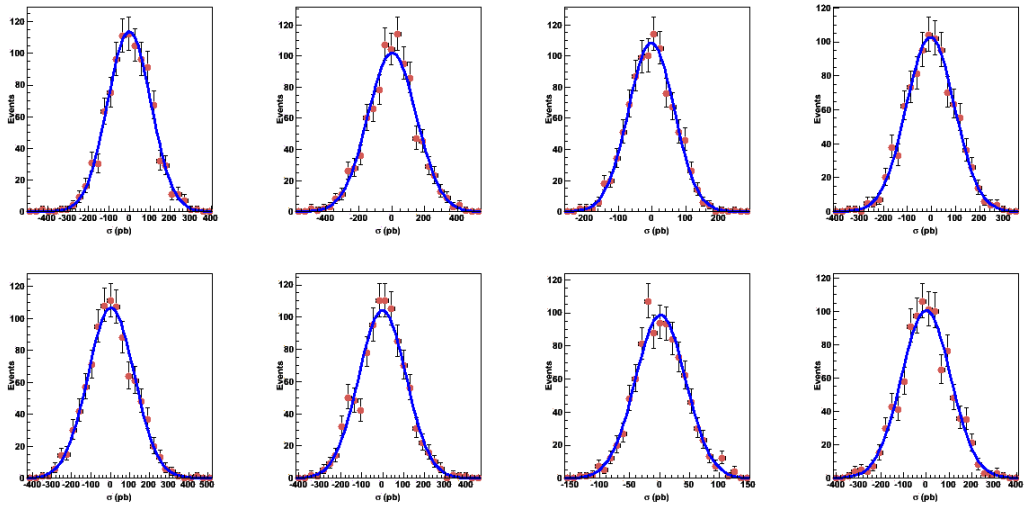

Figure 5.17: The cross-section in each of the eight sample is recalculated 1000 times varying the contribution to the event weights due to the detector acceptance, reconstruction and selection efficiency according to a Gaussian. The distribution of the 1000 measurements is described by a Gaussian, whose width provides an estimate of the systematic uncertainty.

5.5.6 Tracking efficiency

The uncertainty on the maps used to reweight the Monte Carlo events, as described in section 5.3.2, introduces an uncertainty on the cross-section measurement that needs to be evaluated. Again random event weights are generated as done in the last two sections. Figure 5.18 shows the cross-section distribution obtained after generating 1000 sets of Gaussian weights. The estimated uncertainty is shown in Table 5.14.

It has to be noted that the correction maps are not available for downstream tracks and those for T-tracks were used instead.

An systematic uncertainty from the method of building the tracking map of 0.7% is assigned per track, as recommended by the tracking group. As $\Lambda_b \to J/\psi\Lambda^0$

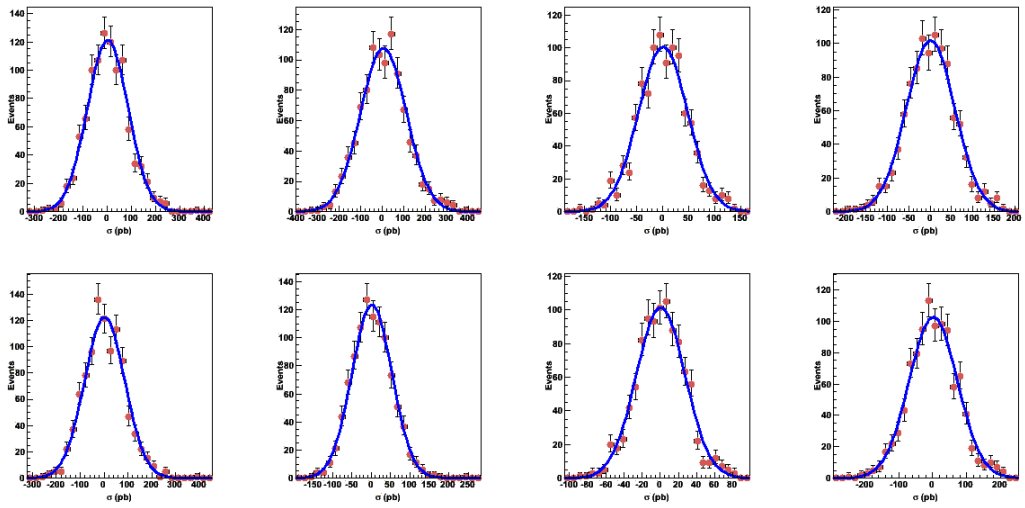

Figure 5.18: The cross-section in each of the eight samples is recalculated 1000 times varying the contribution to the event weights due to the tracking efficiency according to a Gaussian. The distribution of the 1000 measurements is described by a Gaussian, whose width provides an estimate of the systematic uncertainty.

model	LLPUp	LLPDw	DDPUp	DDPDw	LLNUp	LLNDw	DDNUp	DDNDw
nominal	3687±1245	4807±1441	3927±1068	4190±1093	3537±1261	1944±884	2048±695	5015±1185
%	4.3±0.1	4.47±0.10	3.32±0.08	3.52±0.08	4.26±0.10	4.24±0.10	3.26±0.07	3.54±0.08

Table 5.14: Systematic uncertainty on the Λ_b cross-section due to the error in the measurement of the tracking efficiency.

involves four tracks, the total error of 2.8% is added to the list of systematic errors.

5.5.7 Global event cuts

The statistical error on the GEC efficiency extracted from data (0.6%) is taken as systematic uncertainty associated with the GEC, as done in the J/ψ cross-section measurement [119].

5.5.8 Primary vertex reconstruction

The different primary vertex reconstruction efficiency between data and Monte Carlo introduces a systematic uncertainty due to the limited statistics used to measure this effect. This uncertainty is estimated to be 0.8% [29].

5.5.9 Muon identification

An uncertainty of 1.1% is assigned to the "tag and probe" method used to measure the muon ID scale factor described in 5.3.4 [29; 120].

5.5.10 Proton identification

Among the criteria for selecting LL Λ^0 a requirement of (ΔLL $= -5$) for the proton pid is applied. While extremely loose, this is not 100% efficient and, more importantly, the effiency measured on data is slightly different from simulation, as evident in Figures 5.19 where the ratio between the values obtained in data and in Monte Carlo is shown as function of the ΔLL. A factor equal to half the fractional difference between the efficiency in simulation and in data efficiency, Table 5.15, is assigned as systematic uncertainty.

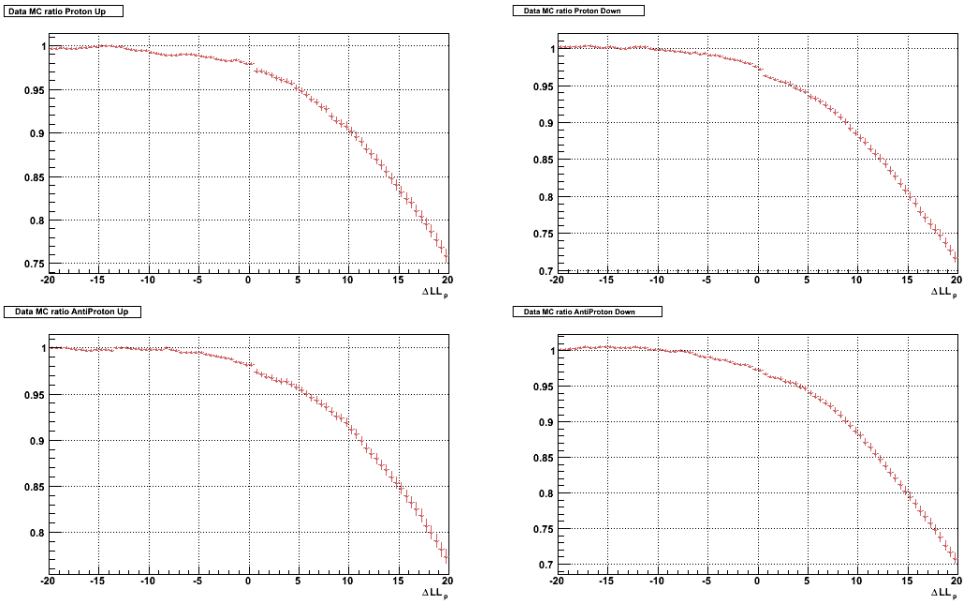

Figure 5.19: The ratio between the proton PID efficiency measured in data and in simulation as function of the ΔLL for the LLPUp, top left, LLPDw, top right, LLNUp, bottom left, and LLNDw, bottom right, case.

	LLPUp	LLPDw	DDPUp	DDPDw	LLNUp	LLNDw	DDNUp	DDNDw
PID eff. Data %	98.47	98.35	-	-	98.34	98.25	-	-
PID eff. MC %	99.6	99.19	-	-	98.79	99.16	-	-
nominal	3687±1245	4807±1441	3927±1068	4190±1093	3537±1261	1944±884	2048±695	5015±1185
proton id %	0.23	0.46	0.0	0.0	0.56	0.43	0.0	0.0

Table 5.15: The efficiencies of the PID cut at the working point $\Delta\text{LL} = -5$ in data and the MC. The relative error between the two cases is taken as a systematic error for the cross section due to this efect.

5.5.11 Crossing angle

The two beams interact in LHCb at an angle different from 0. This implies that the laboratory frame of reference does not coincide with the center of mass frame. Furthermore the crossing angle can depend on the magnet polarity and on the beam structure. For the first part of the 2010 data taking the angle was 270 μrad for both polarities. Starting with fill 1364 the 150 ns filling scheme was introduced, which meant the total crossing angle became 520 μrad for the negative polarity and 20 μrad for the positive polarity. The effects of the different frame of references are taken into account in the analysis applying the appropriate boost to the Λ_b momentum. However in the Monte Carlo the beam is always simulated following the 2^{nd} part of the year configuration. As a consequence a systematic uncertainty is introduced by the different frames between part of the data and the simulation. Fortunately this is a small effect as the Monte Carlo corresponds to more than 90% of the overall luminosity collected in 2010. In order to estimate an upper limit to this effect the analysis has been repeated without applying the boost and half of the difference from the nominal result is assigned as systematic uncertainty, Table 5.16.

model	LLPUp	LLPDw	DDPUp	DDPDw	LLNUp	LLNDw	DDNUp	DDNDw
angle_0	3675±1229	4825±1435	3934±1074	4240±1116	3534±1309	1932±868	2047±686	4994±1202
nominal	3687±1245	4807±1441	3927±1068	4190±1093	3537±1261	1944±884	2048±695	5015±1185
%	0.16	0.19	0.09	0.6	0.04	0.31	0.02	0.21

Table 5.16: In order to estimate an upper limit to the uncertainty introduced by considering a different beam crossing angle between part of the data and the simulation the analysis has been carried out without applying the boost to bring the lab frame to the CM frame, and half of the difference is assigned as error.

5.5.12 Summary of systematic uncertainties

The complete list of systematic uncertainties considered in this analysis is shown in Table 5.17. All uncertainties are combined to provide a final systematic uncertainty, where correlations are possible between the contributions maximum correlation is assumed and the final uncertainty is calculated accordingly, [123; 124].

model	LLPUp	LLPDw	DDPUp	DDPDw	LLNUp	LLNDw	DDNUp	DDNDw
fit sys	7.7±13.3	5.8±11.4	4.36±10.69	4.77±9.48	0.265±13.540	3.47±16.73	4.99±13.56	4.67±8.73
pol sys	0.865±23.906	2.66±21.21	0.688±19.246	0.607±18.475	0.81±25.23	3.74±32.18	0.293±24.000	0.403±16.754
tracking sys	4.3±0.1	4.47±0.10	3.32±0.08	3.52±0.08	4.26±0.10	4.24±0.10	3.26±0.07	3.54±0.08
select sys	1.13±1.42	0.376±1.246	0.1409±1.1330	0.127±1.084	0.396±1.498	0.575±1.892	1.94±1.40	0.558±0.983
recVar sys	4.02±0.09	4.34±0.10	2.59±0.06	3.57±0.08	4.27±0.10	7.6±0.2	3.05±0.07	3.32±0.08
trigVar sys	2.93±0.07	3±0	2.4±0.1	3.84±0.09	2.23±0.05	5.03±0.11	2.46±0.06	4.48±0.10
muon id	1.12±0.00	1.12±0.00	1.12±0.00	1.12±0.00	1.12±0.00	1.12±0.00	1.12±0.00	1.12±0.00
proton id	0.23±0.00	0.46±0.00	0±0	0±0	0.56±0.00	0.43±0.00	0±0	0±0
vertex sys	0.787±0.000	0.787±0.000	0.787±0.000	0.787±0.000	0.787±0.000	0.787±0.000	0.787±0.000	0.787±0.000
cross ang	0.16±0.00	0.19±0.00	0.09±0.00	0.6±0.0	0.04±0.00	0.31±0.00	0.02±0.00	0.21±0.00
gec	0.6±0.0	0.6±0.0	0.6±0.0	0.6±0.0	0.6±0.0	0.6±0.0	0.6±0.0	0.6±0.0
lumi	3.5±0.0	3.5±0.0	3.5±0.0	3.5±0.0	3.5±0.0	3.5±0.0	3.5±0.0	3.5±0.0
bratio	1±0	1±0	1±0	1±0	1±0	1±0	1±0	1±0
nominal	3687±1245	4807±1441	3927±1068	4190±1093	3537±1261	1944±884	2048±695	5015±1185
sys total	16.4+/-0.0	16.6+/-0.0	10.9+/-0.0	13.27+/-0.00	12.6+/-0.0	21.9+/-0.0	13.4+/-0.0	13.9+/-0.0

Table 5.17: Systematics errors for cross-section, 2010 data. The errors on the errors in the table are not used further in the calculations.

5.6 Cross-section determination

Replacing in Eq. (5.1) the measured value for the number of $\Lambda_b \to J/\psi\Lambda^0$ decays in the selected phase space one gets:

$$\sigma(pp \to \Lambda_b X)_{PS}\mathcal{B}(\Lambda_b \to J/\psi\,\Lambda^0) = \frac{\mathrm{N}^{corr}_{\Lambda_b}}{\mathcal{L}\cdot\mathcal{B}(\Lambda^0 \to p\pi^-)\mathcal{B}(J/\psi \to \mu^+\mu^-)} \quad (5.11)$$

The detailed results for the cross-section measurement in the selected phase space for the eight samples are shown in Table 5.18 and displayed in Fig.5.20.

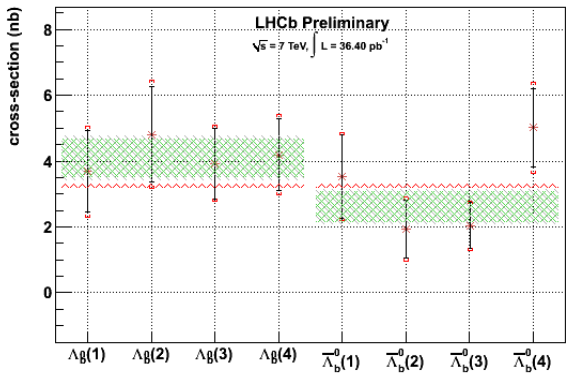

Figure 5.20: The measured cross-section (pb) for the eight samples. The black vertical bars represent the statistical error, the red limits represent the systematic uncertainty. The green horizontal band represents the average for the two species Λ_b and $\bar{\Lambda}_{b0}$ from the corresponding samples. The red horizontal bands represent the predictions of the cross-section from the LHCb MC.

	LLPUp	LLPDw	DDPUp	DDPDw	LLNUp	LLNDw	DDNUp	DDNDw
σ_{PS}	3687±1245	4807±1441	3927±1068	4190±1093	3537±1261	1944±884	2048±695	5015±1185

Table 5.18: The Λ_b production cross-section (pb) in the eight samples, only the statistical error is shown.

The final result is obtained by performing a weighted average on all samples. The systematic uncertainty in all sample has been assumed to be fully correlated.

$$\sigma(pp \to \Lambda_b X)_{PS}\mathcal{B}(\Lambda_b \to J/\Psi\Lambda^0) = 4.08 \pm 0.59(stat) \pm 0.36(sys)\mathrm{nb}$$

$$\sigma(pp \to \bar{\Lambda}_b X)_{PS} \mathcal{B}(\bar{\Lambda}_b \to J/\Psi \bar{\Lambda}^0) = 2.60 \pm 0.46(stat) \pm 0.26(sys)\text{nb}$$

The extended result to the full phase space using the coefficient from section 5.3.1 is:

$$\sigma(pp \to \Lambda_b X)\mathcal{B}(\Lambda_b \to J/\Psi \Lambda^0) = 26.15 \pm 3.78(stat) \pm 2.31(sys)$$
$$\sigma(pp \to \bar{\Lambda}_b X)\mathcal{B}(\bar{\Lambda}_b \to J/\Psi \bar{\Lambda}^0) = 16.67 \pm 2.95(stat) \pm 1.67(sys)$$

The values so obtained can be compared to the prediction of the LHCb Monte Carlo, which can be obtained from the generator input configuration and log files. Defining as $N_{int} = 4338349880$ the total number generated in a sample with no acceptance cuts, and as $N_{evt} = 1971199$ the total number of Λ_b generated in the same sample one obtains that $\sigma_{TOT}^{\Lambda_b}$, the total cross section for the production of Λ_b, is:

$$\sigma_{TOT}^{\Lambda_b}\, \mathcal{B}(\Lambda_b \to \mathrm{J}/\psi \Lambda^0) = 2 \times \sigma_{MB} \frac{N_{evt}}{N_{int}} = 38.89\,\text{nb}$$

where $\sigma_{MB} = 91.05\,\text{mb}$ is the total input cross section used in the simulation. The factor 2 is introduced in Gauss to ensure the correct ratio between the number of events with one $\Lambda_b \to \mathrm{J}/\psi \Lambda^0$ and the number of events with two. Scaling $\sigma_{TOT}^{\Lambda_b}$ by the fraction of Λ_b and $\bar{\Lambda}_b$ in the phase-space selected for this study, one obtains:

$$\sigma_{PS}^{\Lambda_b}\, \mathcal{B}(\Lambda_b \to \mathrm{J}/\psi \Lambda^0) = 3.10\,\text{nb}$$
$$\sigma_{PS}^{\bar{\Lambda}_b}\, \mathcal{B}(\Lambda_b \to \mathrm{J}/\psi \Lambda^0) = 2.95\,\text{nb}$$

CMS collaboration published [125] a differential cross section measurement for the same channel in the phase space $p_T \in (10, 50) GeV$ and $|y| < 2$. In Fig.5.6 we compare the LHCb result expressed as an average between Λ_b^0 and $\bar{\Lambda}_b^0$, with the CMS result, in bins of p_T. The difference in bin dimension between the LHCb and CMS analysis has been taken care of calculating the cross section per unit rapidity in both experiments and then scaling the LHCb results to the width of the CMS rapidity bins. This choice was driven by the fact the cross section has

a much flatter dependance on rapidity than on p_T in the range considered by both experiments. On the same plot the prediction of Pythia (CMS) is shown. The values agree qualitatively with the CMS measurement, however a rigurous quantitative comparison is impossible given the different y and p_T ranges covered by the two experiments.

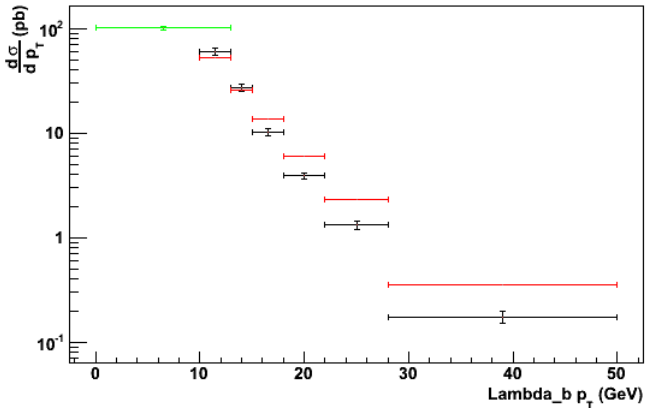

Figure 5.21: Comparison to CMS results, differential cross-section in p_T bins: CMS points in black, Pythia prediction in red (from CMS) and LHCb 2010 point in green. All points represent average values between Λ_b^0 and $\bar{\Lambda}_b^0$.

Chapter 6

Summary

In this thesis we have studied some the aspects of the b quark production at LHCb. In the first two chapters we make a theoretical description of the current formalism that allows calculation at fixed order in perturbation theory NLO and with the resummation of the large logarithms FONLL. These predictions are used from computing codes which, however, are not integrated with the Monte Carlo event generators and cannot be used for studies with simulated events. For our studies we used Pythia 6.4, which is LO generator but has a good description of the hadronization processes.

In the third Chapter, a detailed description of the LHCb detector and its sub-detectors is presented, aiming to provide the reader with more detailed information about the detector's performances and the type of events that can be searched for at the LHCb experiment. Part of my contribution in the collaboration also consisted in participating in the online monitoring of the data acquisition and in offline checking of the data quality.

In the next chapter is described the author contribution to the calibration of the RICH subdetector, responsible for providing identification information for p, π and K particles. Here, we developed a method for calibrating the detector for protons and pions using the data directly from experiment. For LHCb the particle identification ability of RICH is one of the key features, thus these results were used in numerous analysis. An example of the use of these information for the case of Λ_b production is illustrated in the next chapter of the thesis.

A complete data analysis, of the measurement of Λ_b cross-section production

is presented in details in the Chapter 5. The results improve our knowledge on heavy baryon systems, subject which was less accessible and studied in the past. Foreseeable extensions of the analysis, notwithstanding of the better investigation of the Λ_b spectra, are in the direction of studying the fragmentation fractions and their possible dependency of energy, in the investigation of heavier baryons or in the rare decays field.

The software code necessary for this thesis is presented in Annex, which was written in a generically form such that it can be reused in other analysis as well.

All the results from this thesis have been presented publicly in papers and conferences.

Appendix A

A.1 Efficiency details

In this appendix we show some additional information about the efficiencies needed for the Λ_b study from Chapter 5.

The first subsection A.1.1 shows the tables with reconstruction efficiency, which combines the detector acceptance, the detection, reconstruction and selection efficiency as described in Section 5.3.2. The second subsection A.1.2 displays the TISTOS fits used for the estimation of trigger efficiency in 5.3.3, and the tables with the parameters extracted from the fits.

A.1.1 Reconstruction efficiency $p_{\mathrm{T}} - y$

The following Tables A.1, A.2, A.3, A.4, A.5, A.6, A.7, A.8 show the reconstruction efficiency for Λ_b as a function of p_T and y where the Λ^0 is reconstructed as LL (left) and DD (down) and the magnet polarity is "Up" (top row) and ' 'Down" (second row). Also the same information are shown for $\bar{\Lambda}_b$.

Λ_b^0 - $P_T(MeV/c)/y$	2.2 - 2.88	2.88 - 3.13	3.13 - 3.37	3.37 - 3.66	3.66 - 4.5
0 - 1300	0.0071±0.0010	0.0174±0.0026	0.01528±0.00269	0.0243±0.0031	0.0159±0.0021
1300 - 2200	0.0065±0.0008	0.0135±0.0020	0.0276±0.0031	0.0267±0.0033	0.0126±0.0018
2200 - 3300	0.00554±0.00059	0.016±0.002	0.02±0.00	0.0203±0.0025	0.01387±0.00167
3300 - 5100	0.0071±0.0006	0.0194±0.0018	0.0183±0.0021	0.024±0.002	0.013±0.001
5100 - 13000	0.00886±0.00058	0.0184±0.0016	0.0216±0.0020	0.0235±0.0022	0.0208±0.0022

Table A.1: Reconstruction & selection efficiency for LLPUp sample in bins of p_T and y.

Λ_b^0 - $P_T(MeV/c)/y$	2.2 - 2.88	2.88 - 3.13	3.13 - 3.37	3.37 - 3.66	3.66 - 4.5
0 - 1300	0.00638±0.00112	0.0165±0.0028	0.023±0.004	0.0238±0.0038	0.0128±0.0020
1300 - 2200	0.00527±0.00082	0.025±0.003	0.0174±0.0029	0.0205±0.0034	0.00896±0.00138
2200 - 3300	0.00785±0.00090	0.0115±0.0018	0.0236±0.0036	0.0167±0.0024	0.01408±0.00252
3300 - 5100	0.00698±0.00072	0.015±0.002	0.0187±0.0024	0.023±0.003	0.0156±0.0022
5100 - 13000	0.0084±0.0007	0.0188±0.0019	0.021±0.002	0.033±0.003	0.026±0.003

Table A.2: Reconstruction & selection efficiency for LLPDw sample in bins of p_T and y.

Λ_b^0 - $P_T(MeV/c)/y$	2.2 - 2.88	2.88 - 3.13	3.13 - 3.37	3.37 - 3.66	3.66 - 4.5
0 - 1300	0.0125±0.0011	0.0309±0.0032	0.0338±0.0036	0.0339±0.0036	0.01268±0.00156
1300 - 2200	0.0131±0.0010	0.028±0.003	0.0436±0.0037	0.032±0.003	0.0141±0.0023
2200 - 3300	0.0143±0.0010	0.038±0.003	0.0326±0.0029	0.0333±0.0029	0.0141±0.0016
3300 - 5100	0.0233±0.0011	0.0389±0.0025	0.037±0.003	0.0335±0.0027	0.0137±0.0015
5100 - 13000	0.036±0.001	0.0526±0.0024	0.0527±0.0029	0.0468±0.0030	0.0314±0.0027

Table A.3: Reconstruction & selection efficiency for DDPUp sample in bins of p_T and y.

Λ_b^0 - $P_T(MeV/c)/y$	2.2 - 2.88	2.88 - 3.13	3.13 - 3.37	3.37 - 3.66	3.66 - 4.5
0 - 1300	0.0105±0.0013	0.0279±0.0036	0.0375±0.0045	0.0275±0.0037	0.0123±0.0016
1300 - 2200	0.01468±0.00139	0.029±0.003	0.0373±0.0042	0.0327±0.0036	0.01247±0.00191
2200 - 3300	0.0156±0.0013	0.0406±0.0039	0.0397±0.0042	0.0275±0.0032	0.0134±0.0017
3300 - 5100	0.018±0.001	0.039±0.003	0.0369±0.0031	0.0338±0.0031	0.0198±0.0021
5100 - 13000	0.0392±0.0014	0.0488±0.0028	0.052±0.004	0.0456±0.0038	0.0319±0.0031

Table A.4: Reconstruction & selection efficiency for DDPDw sample in bins of p_T and y.

Λ_b^0 - $P_T(MeV/c)/y$	2.2 - 2.88	2.88 - 3.13	3.13 - 3.37	3.37 - 3.66	3.66 - 4.5
0 - 1300	0.00625±0.00087	0.0118±0.0020	0.01860±0.00280	0.02±0.00	0.0141±0.0018
1300 - 2200	0.00615±0.00083	0.0153±0.0021	0.0167±0.0025	0.016±0.002	0.013±0.002
2200 - 3300	0.0063±0.0007	0.0153±0.0020	0.0198±0.0024	0.0188±0.0024	0.0112±0.0014
3300 - 5100	0.0066±0.0006	0.0182±0.0018	0.0166±0.0019	0.01920±0.00210	0.0143±0.0018
5100 - 13000	0.00887±0.00058	0.0181±0.0015	0.021±0.002	0.0264±0.0024	0.0233±0.0025

Table A.5: Reconstruction & selection efficiency for LLNUp sample in bins of p_T and y.

A.1.2 Trigger efficiency $p_{\mathrm{T}} - y$

The trigger efficiency with the TITOS method is extracted following the fits of ~~TIS~~TOS, TISTOS, TIS~~TOS~~ in each $pt - y$ bins for the MagUp and MagDown samples. First the samples with TIS~~TOS~~ events are fitted, Figs A.1, A.2 and $\mathrm{m}_0^{J/\psi}$, $\sigma^{\mathrm{J}/\psi}$ parameters are obtained, Tables A.9, A.10, A.11, A.12. These parameters are subsequently used in the fits of the TISTOS, TIS~~TOS~~ samples.

Λ_b^0 - $P_T(MeV/c)/y$	2.2 - 2.88	2.88 - 3.13	3.13 - 3.37	3.37 - 3.66	3.66 - 4.5
0 - 1300	0.00619±0.00104	0.0228±0.0038	0.0234±0.0041	0.021±0.003	0.0142±0.0024
1300 - 2200	0.0051±0.0009	0.0177±0.0028	0.01920±0.00310	0.0205±0.0035	0.0135±0.0021
2200 - 3300	0.00468±0.00071	0.0165±0.0023	0.0196±0.0029	0.0162±0.0023	0.0099±0.0015
3300 - 5100	0.00625±0.00070	0.0172±0.0022	0.01569±0.00219	0.02±0.00	0.0141±0.0018
5100 - 13000	0.0097±0.0007	0.019±0.002	0.026±0.003	0.022±0.003	0.0347±0.0047

Table A.6: Reconstruction & selection efficiency for LLNDw sample in bins of p_T and y.

Λ_b^0 - $P_T(MeV/c)/y$	2.2 - 2.88	2.88 - 3.13	3.13 - 3.37	3.37 - 3.66	3.66 - 4.5
0 - 1300	0.0118±0.0011	0.0339±0.0034	0.0308±0.0035	0.0342±0.0035	0.0124±0.0016
1300 - 2200	0.0137±0.0011	0.031±0.003	0.0325±0.0034	0.0263±0.0029	0.0127±0.0016
2200 - 3300	0.0156±0.0010	0.0323±0.0027	0.0407±0.0034	0.0403±0.0035	0.0133±0.0016
3300 - 5100	0.0195±0.0010	0.0394±0.0025	0.0368±0.0027	0.0302±0.0023	0.0203±0.0022
5100 - 13000	0.0375±0.0011	0.0559±0.0026	0.0494±0.0029	0.049±0.003	0.0308±0.0025

Table A.7: Reconstruction & selection efficiency for DDNUp sample in bins of p_T and y.

Λ_b^0 - $P_T(MeV/c)/y$	2.2 - 2.88	2.88 - 3.13	3.13 - 3.37	3.37 - 3.66	3.66 - 4.5
0 - 1300	0.0095±0.0011	0.0299±0.0042	0.0337±0.0045	0.0307±0.0040	0.0115±0.0016
1300 - 2200	0.0119±0.0012	0.0289±0.0034	0.0314±0.0037	0.0297±0.0036	0.0139±0.0019
2200 - 3300	0.01299±0.00106	0.0366±0.0035	0.0445±0.0046	0.036±0.004	0.0137±0.0018
3300 - 5100	0.021±0.001	0.0395±0.0031	0.0397±0.0034	0.0346±0.0033	0.0189±0.0020
5100 - 13000	0.0397±0.0014	0.053±0.003	0.055±0.004	0.0527±0.0044	0.0334±0.0031

Table A.8: Reconstruction & selection efficiency for DDNDw sample in bins of p_T and y.

TISTOS fits were also tried starting with a Gaussian function, and similar results were obtained for the efficiency.

J_psi_1S_PT/J_psi_1S_RAP	2.2 - 2.88	2.88 - 3.13	3.13 - 3.37	3.37 - 3.66	3.66 - 4.5
0 - 1300	3096.1+/-0.1	3095.3+/-0.1	3095.3+/-0.1	3095.3+/-0.1	3094.9+/-0.1
1300 - 2200	3095.8+/-0.1	3095.2+/-0.1	3095.0+/-0.1	3094.9+/-0.1	3094.1+/-0.1
2200 - 3300	3095.6+/-0.1	3095.1+/-0.1	3094.7+/-0.1	3094.8+/-0.1	3094.4+/-0.1
3300 - 5100	3095.6+/-0.1	3094.7+/-0.1	3094.6+/-0.1	3094.4+/-0.1	3094.1+/-0.1
5100 - 13000	3095.2+/-0.1	3094.6+/-0.1	3094.3+/-0.1	3094.1+/-0.1	3093.8+/-0.2

Table A.9: Characterisation of the trigger efficiency calculation. The mean value extracted from the fit is shown in different bins; MagUp sample.

J_psi_1S_PT/J_psi_1S_RAP	2.2 - 2.88	2.88 - 3.13	3.13 - 3.37	3.37 - 3.66	3.66 - 4.5
0 - 1300	3095.5+/-0.1	3094.6+/-0.1	3094.3+/-0.1	3093.6+/-0.1	3092.0+/-0.1
1300 - 2200	3095.4+/-0.1	3094.5+/-0.1	3094.0+/-0.1	3093.4+/-0.1	3091.7+/-0.1
2200 - 3300	3095.3+/-0.0	3094.3+/-0.1	3093.7+/-0.1	3093.5+/-0.1	3091.9+/-0.1
3300 - 5100	3094.9+/-0.0	3094.0+/-0.1	3093.7+/-0.1	3093.4+/-0.1	3092.4+/-0.1
5100 - 13000	3094.5+/-0.0	3093.7+/-0.1	3093.5+/-0.1	3093.5+/-0.1	3093.1+/-0.1

Table A.10: Characterisation of the trigger efficiency calculation. The mean value extracted from the fit is shown in different bins; MagDw sample.

J_psi_1S_PT/J_psi_1S_RAP	2.2 - 2.88	2.88 - 3.13	3.13 - 3.37	3.37 - 3.66	3.66 - 4.5
0 - 1300	10.97+/-0.11	11.77+/-0.13	12.3+/-0.1	13.08+/-0.13	15.2+/-0.1
1300 - 2200	10.9+/-0.1	11.98+/-0.09	12.7+/-0.1	13.9+/-0.1	15.59+/-0.09
2200 - 3300	11.37+/-0.06	12.27+/-0.08	13.08+/-0.09	14.19+/-0.10	16.4+/-0.1
3300 - 5100	12.0+/-0.1	12.8+/-0.1	13.8+/-0.1	14.8+/-0.1	17.1+/-0.1
5100 - 13000	13.1+/-0.1	14.20+/-0.10	15.0+/-0.1	16.3+/-0.1	18.6+/-0.2

Table A.11: Characterisation of the trigger efficiency calculation. The sigma value extracted from the fit is shown in different bins; MagUp sample.

J_psi_1S_PT/J_psi_1S_RAP	2.2 - 2.88	2.88 - 3.13	3.13 - 3.37	3.37 - 3.66	3.66 - 4.5
0 - 1300	11.1+/-0.1	12.1+/-0.1	12.8+/-0.1	14.09+/-0.12	16.2+/-0.1
1300 - 2200	11.26+/-0.06	12.3+/-0.1	13.38+/-0.08	14.4+/-0.1	16.9+/-0.1
2200 - 3300	11.5+/-0.0	12.8+/-0.1	13.7+/-0.1	15.1+/-0.1	17.7+/-0.1
3300 - 5100	12.1+/-0.0	13.5+/-0.1	14.50+/-0.07	16.0+/-0.1	18.7+/-0.1
5100 - 13000	13.2+/-0.0	14.79+/-0.08	16.1+/-0.1	17.6+/-0.1	20.5+/-0.2

Table A.12: Characterisation of the trigger efficiency calculation. The sigma value extracted from the fit is shown in different bins; MagDw sample.

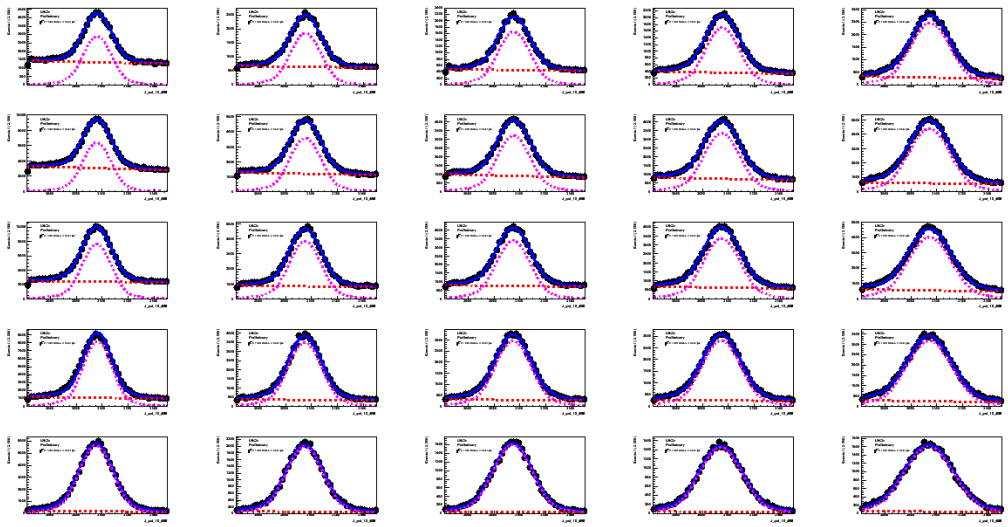

Figure A.1: Fits with the double Crystal Ball function described in section 5.3.3 for J/ψ invariant mass from the ~~TIS~~TOS class type of events; magnet Up sample.

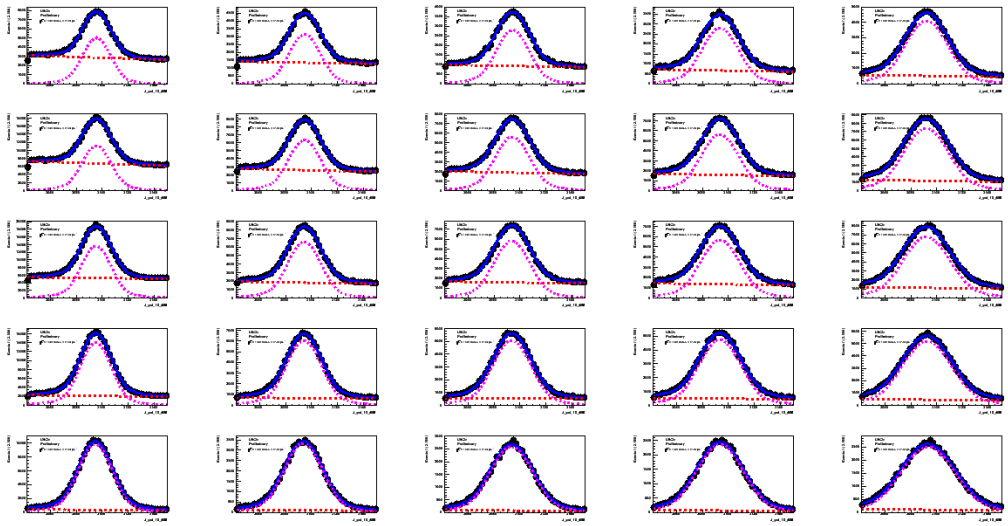

Figure A.2: Fits with the double Crystal Ball function described in section 5.3.3 for J/ψ invariant mass from the ~~TIS~~TOS class type of events; magnet Up sample.

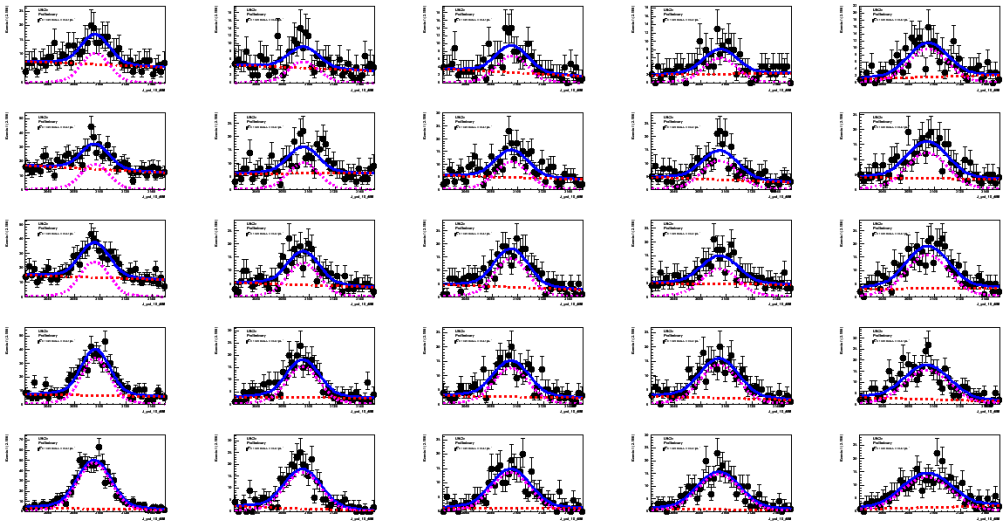

Figure A.3: Fits with the double Crystal Ball function described in section 5.3.3 for J/ψ invariant mass from the TISTOS class type of events; magnet Up sample.

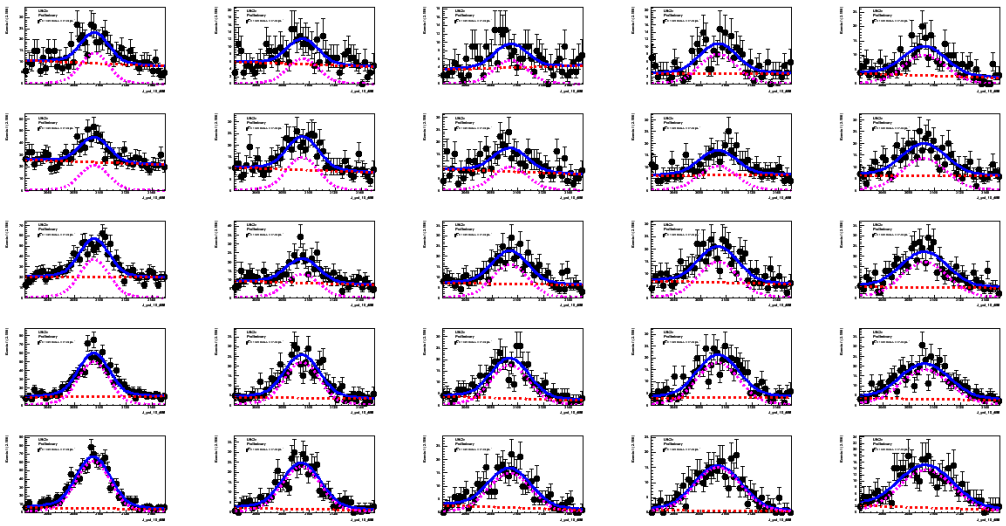

Figure A.4: Fits with the double Crystal Ball function described in section 5.3.3 for J/ψ invariant mass from the TISTOS class type of events; magnet Dw sample.

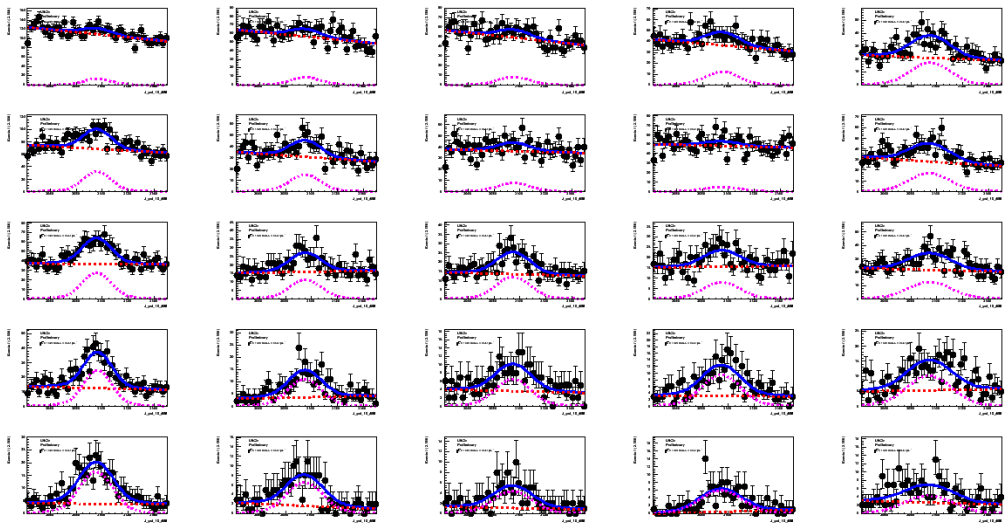

Figure A.5: Fits with the double Crystal Ball function described in section 5.3.3 for J/ψ invariant mass from the TIS~~TOS~~ class type of events; magnet Up sample.

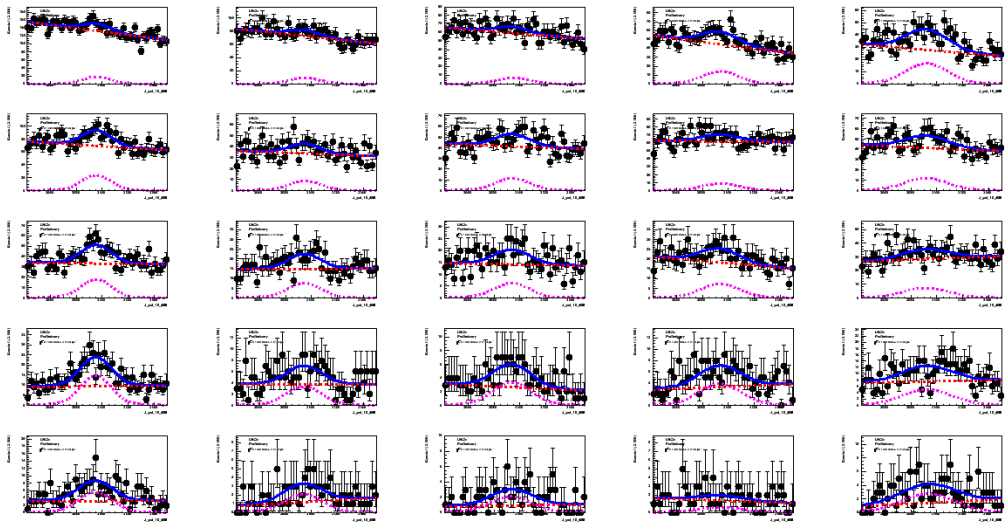

Figure A.6: Fits with the double Crystal Ball function described in section 5.3.3 for J/ψ invariant mass from the TIS~~TOS~~ class type of events; magnet Dw sample.

A.2 BPython: The offline software package

In this appendix we describe the BPython software package developed by the author for the studies of this thesis. It is a Python [92] layer over the more basic ROOT [91] C++ framework. The larger goal for this package is to make the code to be reusable for later analyses, thus, the main feature of the whole package is to provide templates for analyses, such that a new analysis can be easily developed having the basic steps already implemented. In more than 100 files, the package collects a series of useful routines and representations of the data and of the algorithms needed. In this presentation of the package we give some reasons for it and describe its structure having in mind a future extension of the text to a *User manual*.

A.2.1 Introduction

A significant amount of the physicist's time is spent on transposing the specific information and ideas into a state which can be handled by computers. There is a continuous effort to find the best representation of the knowledge, such that its implementation to be as easy and generic as possible. The ultimate goal would be to develop a framework for processing the natural language to software codes, which can control the flow of the algorithms. The package developed here is a step in this direction trying to design tools for some basic and frequent tasks met during an analysis and which can be easily reused in similar contexts.

The inspiration for this work came from noticing the trends in the scientific software. At the end of 90's the CERN program library (CERNLIB) started to be translated from Fortran to C++, an object oriented language. The recoding effort was needed to cope with the challenges of the new internet era, large data input and friendlier interaction with the end user. The ROOT framework, used for large scale data handling applications, inherits previous developed abilities for performing data analysis including linear algebra classes, numerical algorithms such as integration and minimization, and various methods for performing regression analysis (fitting), but most important it offers the flexibility of adding new functionality. The software packages used by LHC experiments are examples of new packages based on ROOT. Other packages not related to a specific collab-

oration are: RooFit [126] package, which allows the user to perform complex data modeling and fitting, the RooStats [127] library, which provides abstractions and implementations for advanced statistical tools. A special package interesting for a large set of users from different scientific fields is the TMVA[128] package, which makes available multivariate classification methods based on machine learning techniques.

In the context of LHCb experiment, ROOT is the default framework for offline data analysis, it provides the basic function for transforming, manipulating and representing the data. Our BPython package makes templates of data analyses, which can be applied in specific cases as in the Λ_b measurement described in Chapter 5. The range of procedures subject to templating is not fixed and can be changed in future version of the code, for the moment it includes transformation of data from ntuples files into a new format, quick visualization of different variables describing similar conditions, computing the efficiencies, simultaneously fits, generation of toy tests. The tools are available as shell commands and require a minimum of user interaction for the default use, while permitting re-use, portability and straightforward modification.

A.2.2 Concepts and features

The code is splitted into two packages. The first one is the directory *BHPlot* and contains generic algorithms and definitions of new data structures, the second package is placed in the *Analysis* directory and contains the analysis templates files and the specific analyses. The main functions of these packages are to abstract the basic steps of a a typical analysis and generates automatic code for it.

Generic classes

The files contained in the first package, also called modules, are listed below:

BCanvas.py	BHPlot.py	BStyles.py
BCreateHist.py	BPath.py	BTreeHelper.py
BCriteria.py	BPickle.py	BWeights.py
BCuttester.py	BPlotUtils.py	__init__.py
BDataSet.py	BRooDataLoader.py	ReadNtuples.py
BFrame.py	BRooData.py	
BHClass.py	BSelection.py	

Some classes from these modules are extensions of ROOT and RooFit classes like *BCanvas, BCut, BFrame, RealVar, BRooData, BTree* etc. The others implement new functionalities needed in the process of creating template analyses. We describe here some of these functionalities only to illustrate the concepts and capabilities, a full reference manual and tutorial being deferred for a later time.

The current version of the software uses input data from *.root* files and Berkley database files. The physical path to the resources is managed by a few classes, *BPath, BTree, BRooData* which unify the addressing method to different type of objects or files.

BSelection class describes a collection of conditions which are typically applied for refining the data available. Since the inspection of physical variables in different conditions is a very frequent operation, a special care has been taken that the class be very flexible and intuitive to operate with. It supports easy extension, merging, extraction operations and can be conveniently used to generate statistics about datasets. *BStyles* class is used to translate these information into LaTeX tables.

The last feature we mention here is the one introduced in *BWeight* and *THWeight* classes. We usually operate with a discreet representation of the reality (the distributions are sampled in finite number of points) thus we design a special class, *BWeight*, to represent a "bin" of information. *THWeight* is then, a collection of these enhanced bins which supports transitions from different formats and representations.

Templated analyses

If the previously described package introduces a new vocabulary, the second package that will be presented here, *Analysis*, is a collection of procedures/tasks performed during an analysis.

A specific analysis is structured as a collection of definitions of the main operands found in *lib/* directory, a collection of scripts for performing specific operations placed in *bin/* directory and some configuration and bootstrapping files.

The *lib/* directory contains definitions of actual data and parameters used in for the study, thus we define classes/objects and Python dictionaries to represent the trigger lines used, the location of data, the main selection objects, binning schemes, fitting models, weights from external sources, constants etc. All these items are assembled in one master definition which represents an analysis, i.e. the full set of parameters. Variations of this master object are allowed for the study of the systematic uncertainties.

The *bin/* directory contains the implementation of different common tasks like plotting multiple variables, fitting mass spectra, computing efficiencies, generating toy Monte Carlo samples, extracting systematic effects, delivering results etc.

Most of these files are automatically generated at the start of a new project. The bootstrap files are first executed and they map the root files, which will be used in the analysis, in static Python files in *lib/* directory. Other files containing templates of common definition are also generated after answering short questions like, the decay chain. After the installation is finished one has the code already written for the basic operations: plotting, statistics for the data, efficiencies plots. Less standard algorithms are available as examples in the repository of the previously developed analyses.

A.2.3 Installation and usage

The latest version of the BPython package contains about 25000 lines of code and 140 files. The package has been used by the author in several analyses and also by colleagues from LHCb-RO group. Next releases are foreseen to introduce

more functionalities and classification of analyses types.

The code is available as Python packages and requires the Python 2.6, a recent version of ROOT with RooFit and pyroot modules included. It can be downloaded from lxplus machines at:

`/afs/cern.ch/user/b/bpopovic/public/BPython/`

and can be installed using the following command

```
>> setup.py bpython.v1r0
```

For generating a new analysis one first creates a *buildout* files with the command

```
>>python bootstrap.py
```

This *buildout* file can be edited to specify the parameters required to generate the analysis files. One runs the buildout:

```
>>bin/buildout
```

The executable scripts are already available in *bin/* with some default parameters. Further information can be inserted in *lib/* directory. The package contains a README file with more instruction and all the Python code generated is interspersed with comments.

References

[1] Georges Aad et al. Observation of a new particle in the search for the Standard Model Higgs boson with the ATLAS detector at the LHC. *Phys.Lett.*, B716:1–29, 2012. 2, 35

[2] Serguei Chatrchyan et al. Observation of a new boson at a mass of 125 GeV with the CMS experiment at the LHC. *Phys.Lett.*, B716:30–61, 2012. 2, 35

[3] T. Aaltonen et al. Invariant Mass Distribution of Jet Pairs Produced in Association with a W boson in $p\bar{p}$ Collisions at $\sqrt{s} = 1.96$ TeV. *Phys.Rev.Lett.*, 106:171801, 2011. 5, 6

[4] P. Nason. Introduction to QCD. *Conf.Proc.*, C9705251:94–149, 1997. 9, 11, 12

[5] Frank Wilczek. What QCD tells us about nature - and why we should listen. *Nucl.Phys.*, A663:3–20, 2000. 9

[6] Andreas S. Kronfeld and Chris Quigg. Resource Letter: Quantum Chromodynamics. *Am.J.Phys.*, 78:1081–1116, 2010. 10

[7] F. Halzen and Alan D. Martin. QUARKS AND LEPTONS: AN INTRODUCTORY COURSE IN MODERN PARTICLE PHYSICS. 1984. 13

[8] Jiri Chyla. Quarks, partons and Quantum Chromodynamics. 2004. 11

[9] Peter Z. Skands. QCD for Collider Physics. 2011. 13, 15

[10] Siegfried Bethke. The 2009 World Average of alpha(s). *Eur.Phys.J.*, C64:689–703, 2009. 16

[11] C. Becchi, A. Rouet, and R. Stora. Renormalization of Gauge Theories. *Annals Phys.*, 98:287–321, 1976. 16

[12] P. Nason, S. Dawson, and R. Keith Ellis. The Total Cross-Section for the Production of Heavy Quarks in Hadronic Collisions. *Nucl.Phys.*, B303:607, 1988. 17, 18

[13] P. Nason, S. Dawson, and R. Keith Ellis. The One Particle Inclusive Differential Cross-Section for Heavy Quark Production in Hadronic Collisions. *Nucl.Phys.*, B327:49–92, 1989. 18

[14] Matteo Cacciari and Mario Greco. Large p_T hadroproduction of heavy quarks. *Nucl.Phys.*, B421:530–544, 1994. 18

[15] Matteo Cacciari, Mario Greco, and Paolo Nason. The P(T) spectrum in heavy flavor hadroproduction. *JHEP*, 9805:007o, 1998. 18, 24

[16] Guido Altarelli and G. Parisi. Asymptotic Freedom in Parton Language. *Nucl.Phys.*, B126:298, 1977. 19

[17] H.L. Lai et al. Global QCD analysis of parton structure of the nucleon: CTEQ5 parton distributions. *Eur.Phys.J.*, C12:375–392, 2000. 19

[18] Alan D. Martin, R.G. Roberts, W. James Stirling, and R.S. Thorne. Parton distributions: A New global analysis. *Eur.Phys.J.*, C4:463–496, 1998. 19

[19] F.D. Aaron et al. Combined Measurement and QCD Analysis of the Inclusive e+- p Scattering Cross Sections at HERA. *JHEP*, 1001:109, 2010. 20

[20] J. Beringer et al. Review of particle physics. *Phys. Rev.*, D86:010001, 2012. 21, 27, 29

[21] Torbjörn Sjöstrand, Stephen Mrenna, and Peter" Skands. PYTHIA 6.4 physics and manual. *JHEP*, 05:026, 2006. 21, 81

[22] Torbjorn Sjostrand, Stephen Mrenna, and Peter Z. Skands. A Brief Introduction to PYTHIA 8.1. *Comput.Phys.Commun.*, 178:852–867, 2008. 21

[23] M. Bahr, S. Gieseke, M.A. Gigg, D. Grellscheid, K. Hamilton, et al. Herwig++ Physics and Manual. *Eur.Phys.J.*, C58:639–707, 2008. 21

[24] T. Gleisberg, Stefan. Hoeche, F. Krauss, M. Schonherr, S. Schumann, et al. Event generation with SHERPA 1.1. *JHEP*, 0902:007, 2009. 21, 22

[25] Paolo Nason. A New method for combining NLO QCD with shower Monte Carlo algorithms. *JHEP*, 0411:040, 2004. 24

[26] Stefano Frixione, Paolo Nason, and Carlo Oleari. Matching NLO QCD computations with Parton Shower simulations: the POWHEG method. *JHEP*, 0711:070, 2007. 24

[27] Simone Alioli, Paolo Nason, Carlo Oleari, and Emanuele Re. A general framework for implementing NLO calculations in shower Monte Carlo programs: the POWHEG BOX. *JHEP*, 1006:043, 2010. 24

[28] R. Aaij et al. Measurement of $\sigma(pp \to b\bar{b}X)$ at $\sqrt{s} = 7$ TeV in the forward region. *Phys.Lett.*, B694:209–216, 2010. 25, 77

[29] R. Aaij et al. Measurement of J/ψ production in pp collisions at $\sqrt{s} = 7$ TeV. *Eur.Phys.J.*, C71:1645, 2011. 25, 96, 107, 108

[30] R. Aaij et al. Measurement of b-hadron production fractions in 7 TeVpp collisions. *Phys.Rev.*, D85:032008, 2012. 25, 29

[31] R. Aaij et al. Measurement of the B+- production cross-section in pp collisions at sqrt(s)=7 TeV. *JHEP*, 1204:093, 2012. 25

[32] Bo LIU, Yuanning GAO, Patrick ROBBE, and Jibo HE. *Measurements of the B meson production cross-sections at LHCb. oai:cds.cern.ch:1484857.* PhD thesis, Tsinghua U., Beijing, Jun 2012. Presented 05 Jun 2012. 25

[33] Nathan Isgur. Why N*'s are important. 2000. 26

[34] Jonathan L. Rosner. Non-factorizable effects in top quark production. *Phys.Rev.*, D86:014011, 2012. 27, 31

[35] V.A. Bednyakov, G.I. Lykasov, and V.V. Lyubushkin. Forward production of beauty baryons in pp collisions at LHC. *Europhys.Lett.*, 92:31001, 2010. 27

[36] G. Bari, M. Basile, G. Bruni, G. Cara Romeo, R. Casaccia, et al. The Lambda/b0 beauty baryon production in proton proton interactions at s**(1/2) = 62-GeV: A Second observation. *Nuovo Cim.*, A104:1787–1800, 1991. 27

[37] G. Bari, M. Basile, G. Bruni, G. Cara Romeo, R. Casaccia, et al. A Measurement of Lambda/c+ baryon production in proton proton interactions at s**(1/2) = 62-GeV. *Nuovo Cim.*, A104:571–599, 1991. 27

[38] Y. Amhis et al. Averages of b-hadron, c-hadron, and tau-lepton properties as of early 2012. 2012. 28, 30

[39] Ikaros I.Y. Bigi. The QCD perspective on lifetimes of heavy flavor hadrons. 1995. 28

[40] Fabrizio Gabbiani, Andrei I. Onishchenko, and Alexey A. Petrov. Lambda(b) lifetime puzzle in heavy quark expansion. *Phys.Rev.*, D68:114006, 2003. 28

[41] Fabrizio Gabbiani, Andrei I. Onishchenko, and Alexey A. Petrov. Spectator effects and lifetimes of heavy hadrons. *Phys.Rev.*, D70:094031, 2004. 28

[42] T. Aaltonen et al. Measurement of b hadron lifetimes in exclusive decays containing a J/ψ in p^- pbar collisions at $\sqrt{s} = 1.96$TeV. *Phys.Rev.Lett.*, 106:121804, 2011. 28

[43] D. Ebert, R.N. Faustov, and V.O. Galkin. Masses of heavy baryons in the relativistic quark model. *Phys.Rev.*, D72:034026, 2005. 28

[44] Eberhard Klempt and Jean-Marc Richard. Baryon spectroscopy. *Rev.Mod.Phys.*, 82:1095–1153, 2010. 28

[45] Measurement of the masses of the ξ_b^- and ω_b^-. Nov 2011. Linked to LHCb-ANA-2011-075. 29

[46] R Aaij et al. Observation of excited Λ_b^0 baryons. *Phys. Rev. Lett. 109,*, 172003, 2012. 29

[47] Serguei Chatrchyan et al. Observation of a new Xi(b) baryon. *Phys.Rev.Lett.*, 108:252002, 2012. 29

[48] Victor Mukhamedovich Abazov et al. Forward-backward asymmetry in top quark-antiquark production. *Phys.Rev.*, D84:112005, 2011. 30

[49] T. Aaltonen et al. Evidence for a Mass Dependent Forward-Backward Asymmetry in Top Quark Pair Production. *Phys.Rev.*, D83:112003, 2011. 30

[50] Moira I. Gresham, Ian-Woo Kim, and Kathryn M. Zurek. Searching for Top Flavor Violating Resonances. *Phys.Rev.*, D84:034025, 2011. 30

[51] Daniel Duffty, Zack Sullivan, and Hao Zhang. Top quark forward-backward asymmetry and W' bosons. *Phys.Rev.*, D85:094027, 2012. 30

[52] R. Mohanta and A.K. Giri. Fourth generation effect on Λ_b decays. *Phys.Rev.*, D82:094022, 2010. 31

[53] Thomas Appelquist, Hsin-Chia Cheng, and Bogdan A. Dobrescu. Bounds on universal extra dimensions. *Phys.Rev.*, D64:035002, 2001. 31

[54] K. Azizi and N. Katirci. Investigation of the $\Lambda_b \to \Lambda \ell^+ \ell^-$ transition in universal extra dimension using form factors from full QCD. *JHEP*, 1101:087, 2011. 32

[55] A. Abashian, K. Gotow, N. Morgan, L. Piilonen, S. Schrenk, et al. The Belle Detector. *Nucl.Instrum.Meth.*, A479:117–232, 2002. 33

[56] SLD DESIGN REPORT. 1984. 33

[57] Bernard Aubert et al. The BaBar detector. *Nucl.Instrum.Meth.*, A479:1–116, 2002. 33

[58] V.M. Abazov et al. The Upgraded D0 detector. *Nucl.Instrum.Meth.*, A565:463–537, 2006. 33

[59] F. Abe et al. The CDF Detector: An Overview. *Nucl.Instrum.Meth.*, A271:387–403, 1988. 33

[60] Y. Kubota et al. The CLEO-II detector. *Nucl.Instrum.Meth.*, A320:66–113, 1992. 33

[61] I. Abt et al. The H1 detector at HERA. *Nucl.Instrum.Meth.*, A386:310–347, 1997. 33

[62] W. Schmidt-Parzefall. HERA-B: An Experiment to study CP violation at the HERA proton ring using an internal target. *Nucl.Instrum.Meth.*, A368:124–132, 1995. 33

[63] The ZEUS detector: Status report 1993. 1993. 33

[64] K. Ackerstaff et al. The HERMES spectrometer. *Nucl.Instrum.Meth.*, A417:230–265, 1998. 33

[65] J.Z. Bai et al. The BES detector. *Nucl.Instrum.Meth.*, A344:319–334, 1994. 33

[66] M. Barranco-Luque et al. The Construction of the Central Detector for an Experiment at the CERN anti-p p Collider. *Nucl.Instrum.Meth.*, 176:175, 1980. 33

[67] K. Ahmet et al. The OPAL detector at LEP. *Nucl.Instrum.Meth.*, A305:275–319, 1991. 33

[68] The Construction of the L3 Experiment. *Nucl.Instrum.Meth.*, A289:35–102, 1990. 33

[69] P.A. Aarnio et al. The DELPHI detector at LEP. *Nucl.Instrum.Meth.*, A303:233–276, 1991. 33

[70] D. Buskulic et al. Performance of the ALEPH detector at LEP. *Nucl.Instrum.Meth.*, A360:481–506, 1995. 33

[71] B Popovici et al. First evidence for the decay $B_s^0 \to \mu^+\mu^-$. 2012. 35

[72] G. Aad et al. The ATLAS Experiment at the CERN Large Hadron Collider. *JINST*, 3:S08003, 2008. 36

[73] S. Chatrchyan et al. The CMS experiment at the CERN LHC. *JINST*, 3:S08004, 2008. 37

[74] K. Aamodt et al. The ALICE experiment at the CERN LHC. *JINST*, 3:S08002, 2008. 37

[75] O. Adriani et al. The LHCf detector at the CERN Large Hadron Collider. *JINST*, 3:S08006, 2008. 37

[76] G. Anelli et al. The TOTEM experiment at the CERN Large Hadron Collider. *JINST*, 3:S08007, 2008. 38

[77] Jr. Alves, A. Augusto et al. The LHCb Detector at the LHC. *JINST*, 3:S08005, 2008. 39, 42, 44, 78

[78] B. Adeva et al. Roadmap for selected key measurements of LHCb. 2009. 39

[79] LHCb trigger system technical design report. 2003. 42, 64

[80] M. van Beuzekom. Performance of the LHCb detector during 2010-2011 data taking. *PoS*, EPS-HEP2011:190, 2011. 46, 47

[81] LHCb VELO TDR: Vertex locator. Technical design report. 2001. 46

[82] LHCb magnet: Technical design report. 2000. 48

[83] LHCb: Inner tracker technical design report. 2002. 50

[84] LHCb technical design report: Reoptimized detector design and performance. 2003. 50, 67

[85] LHCb: Outer tracker technical design report. 2001. 51

[86] S.N. Filippov, Yu K Gavrilov, E. Guschin, V. Klubov, L. Kravchuk, et al. Design and construction of the LHCb scintillator pad/preshower detector. 2000. 56

[87] LHCb calorimeters: Technical design report. 2000. 56, 57

[88] LHCb TDR computing technical design report. 2005. 60

[89] The BRUNEL Project. http://lhcb-release-area.web.cern.ch/LHCb-release-area/DOC/brunel/, 2013. Accessed: 28/09/2012. 60

[90] The DaVinci Project. http://lhcb-release-area.web.cern.ch/LHCb-release-area/DOC/davinci/, 2013. Accessed: 28/09/2012. 60

[91] R. Brun and F. Rademakers. ROOT: An object oriented data analysis framework. *Nucl.Instrum.Meth.*, A389:81–86, 1997. 61, 123

[92] Python Reference Manual. http://www.python.org, 2001. Accessed: 28/09/2012. 61, 123

[93] The GAUSS Project. http://lhcb-release-area.web.cern.ch/LHCb-release-area/DOC/gauss/, 2013. Accessed: 28/09/2012. 61

[94] D. J. Lange. The EvtGen particle decay simulation package. *Nucl. Instrum. Meth.*, A462:152–155, 2001. 61, 81

[95] John Allison, K. Amako, J. Apostolakis, H. Araujo, P.A. Dubois, et al. Geant4 developments and applications. *IEEE Trans.Nucl.Sci.*, 53:270, 2006. 61

[96] The BOOLE Project. http://lhcb-release-area.web.cern.ch/LHCb-release-area/DOC/boole/, 2013. Accessed: 28/09/2012. 61

[97] The MOORE Project. http://lhcb-release-area.web.cern.ch/LHCb-release-area/DOC/moore/, 2013. Accessed: 28/09/2012. 61

[98] LHCb: RICH technical design report. 2000. 62

[99] M Adinolfi, G Aglieri Rinella, E Albrecht, T Bellunato, S Benson, et al. Performance of the LHCb RICH detector at the LHC. 2012. 62

[100] B Popovici et al. Measurement of b-hadron branching fractions for two-body decays into charmless charged hadrons. *JHEP*, 1210:037, 2012. 63

[101] B. Popovici et al. Opposite-side flavour tagging of B mesons at the LHCb experiment. *Eur.Phys.J.*, C72:2022, 2012. 63

[102] D. Green. The physics of particle detectors. *Camb.Monogr.Part.Phys.Nucl.Phys.Cosmol.*, 12:1–361, 2000. 64

[103] J. Podolanski and R. Armenteros. Iii. analysis of v-events. *Philosophical Magazine Series 7*, 45(360):13–30, 1954. 70

[104] Bogdan Popovici and Sabin Stoica. Calibration of LHCb RICH detectors with $\Lambda \to p\pi$ decay using data. Physics at LHC 2008, Split, Sep 2008. Split University. http://marjan.fesb.hr/physicslhc/. 72

[105] B Popovici et al. Prompt K_s^0 production in pp collisions at $\sqrt{s} = 0.9$ TeV. *Phys.Lett.*, B693:69–80, 2010. 72, 81

[106] B. Popovici et al. Measurement of V^0 production ratios in pp collisions at $\sqrt{s} = 0.9$ and 7 TeV. *JHEP*, 1108:034, 2011. 72

[107] B Popovici et al. Measurement of prompt hadron production ratios in pp collisions at $\sqrt{s} = 0.9$ and 7 TeV. *Eur.Phys.J.*, C72:2168, 2012. 72

[108] Bogdan Popovici. Particle production studies at LHCb. *Acta Phys.Polon.*, B42:1547–1556, 2011. LHCb-PROC-2011-021, CERN-LHCb-PROC-2011-021. 72

[109] Muriel Pivk and Francois R. Le Diberder. SPlot: A Statistical tool to unfold data distributions. *Nucl.Instrum.Meth.*, A555:356–369, 2005. 73

[110] Muriel Pivk. sPLOT: A Quick introduction. pages 173–177, 2006. 73

[111] K. Nakamura et al. Review of particle physics. *J.Phys.*, G37:075021, 2010. 77

[112] M. Ferro-Luzzi. Proposal for an absolute luminosity determination in colliding beam experiments using vertex detection of beam-gas interactions. *Nucl.Instrum.Meth.*, A553:388–399, 2005. 81

[113] M. Clemencic et al. The LHCb simulation application, Gauss: Design, evolution and experience. *J.Phys.Conf.Ser.*, 331:032023, 2011. 81

[114] I. Belyaev et al. Handling of the generation of primary events in Gauss, the LHCb simulation framework. *J.Phys.Conf.Ser.*, 331:032047, 2011. 81

[115] S. Agostinelli et al. GEANT4: A simulation toolkit. *Nucl. Instrum. Meth.*, A506:250, 2003. 81

[116] N. Brook. LHCb Computing Model. 2004. 82

[117] LHCb Stripping page. https://twiki.cern.ch/twiki/bin/view/LHCb/LHCbStripping. Accessed: 28/09/2012. 82

[118] A. Jaeger, P. Seyfert, J. van Tilburg, and De Cian M. Tracking efficiency corrections. https://twiki.cern.ch/twiki/bin/view/LHCb/TrackingEffRatio. Accessed: 28/09/2012. 92, 93

[119] Measurements of the $pp \to \Upsilon \to \mu^+\mu^-$ cross-section at $\sqrt{s} = 7$ TeV at LHCb. https://twiki.cern.ch/twiki/pub/LHCbPhysics/UpsilonProduction/upsxsec_draft3.11.pdf. LHCb-ANA-2011-012. 96, 107

[120] A. Sarti, S. Furcas, G. Lanfranchi, and M. Palutan. Calibration Strategy and Efficiency measurement of the Muon Identification procedure at LHCb. 2010. 96, 108

[121] M. Biglietti et al. Plans for the study of the spin properties of the Λ_b baryon using the decay channel $\Lambda_b \to; J/\psi(\mu + \mu-)\Lambda(p\pi^-)$. 2009. https://cdsweb.cern.ch/record/1167951?ln=en. 101, 102

[122] Natalia Panikashvili, M. Biglietti, Eduard De La Cruz Burelo, H. Neal, M. Smizanska, et al. Λ_b polarization study in the ATLAS experiment. *Nucl.Phys.Proc.Suppl.*, 167:169–172, 2007. 101, 102

[123] Louis Lyons, Duncan Gibaut, and Peter Clifford. HOW TO COMBINE CORRELATED ESTIMATES OF A SINGLE PHYSICAL QUANTITY. *Nucl.Instrum.Meth.*, A270:110, 1988. 104, 110

[124] A. Valassi. Combining correlated measurements of several different physical quantities. *Nucl.Instrum.Meth.*, A500:391–405, 2003. 104, 110

[125] Serguei Chatrchyan et al. Measurement of the Lambda(b) cross section and the $\bar{\Lambda}_b$ to Λ_b ratio with $\Lambda_b \to J/\psi\Lambda$ decays in pp collisions at $\sqrt{s} = 7$ TeV. *Phys.Lett.*, B714:136–157, 2012. 112

[126] Wouter Verkerke and David P. Kirkby. The RooFit toolkit for data modeling. *eConf*, C0303241:MOLT007, 2003. 124

[127] Lorenzo Moneta, Kevin Belasco, Kyle S. Cranmer, S. Kreiss, Alfio Lazzaro, et al. The RooStats Project. *PoS*, ACAT2010:057, 2010. 124

[128] Andreas Hocker, J. Stelzer, F. Tegenfeldt, H. Voss, K. Voss, et al. TMVA - Toolkit for Multivariate Data Analysis. *PoS*, ACAT:040, 2007. 124